QUANTUM INFORMATION PROCESSING WITH TRAPPED IONS AND COLD ATOMIC GASES

by

Chao Shen

A dissertation submitted in partial fulfillment
of the requirements for the degree of
Doctor of Philosophy
(Physics)
in the University of Michigan
2014

Doctoral Committee:

Professor Luming Duan, Chair
Assistant Professor Hui Deng
Professor Georg A. Raithel
Professor Duncan G. Steel
Assistant Professor Kai Sun

To my parents and my wife.

ACKNOWLEDGMENTS

I am greatly indebted to my advisor, Professor Luming Duan, for mentoring me over the last five years. I have always been impressed by his sharp insights, broad knowledge, great taste in physics, the ability to communicate complicated ideas clearly and kind and patient personality. He is a good big picture thinker without any lack of attention to details. He offered me a lot help in my research in different ways from steering my project toward meaningful work to correcting factors of 2 in my manuscripts. Through working with him, I feel I have been always improving overall as a researcher.

I would also like to thank my undergraduate research advisor Professor Yi'an Lei at Peking University, China, for bringing me into the world of physics research and offering initial scientific training. I am also grateful to all the other professors who imparted their knowledge and enthusiams through classroom teaching or otherwise during the ten years of undergraduate and graduate study.

I benefitted tremendously from my group mates and visitors. In particular, Wei Zhang, now a professor at Renmin University, China, generously left many books to me; Jason Kestner, now an assistant professor at University of Maryland Baltimore county, taught me cold atom physics in the very beginning of my research; Yong-Jian Han, now a professor at University of Science and Technology of China, introduced me to the tensor network algorithms and guided me through

some explorations of these algorithms; Zhang-Qi Yin brought to the group news in the field from time to time; Jiang-Min Zhang collaborated with me on cold gas dynamics and produced my first publications; Hong-Chen Jiang shared with me his extensive experience in tensor networks and DMRG during one summer; Guin-Dar Lin, who recently became an assistant professor at National Taiwan University, familiarized me with trapped ion quantum simulation and computation; Yang-Hao Chan shared with me a lot of knowledge and experience in numerical simulation; Zhe-Xuan Gong collaborated with me in some projects and discussed many other general questions; Dong-Ling Deng and Sheng-Tao Wang collaborated and discussed with me on many quantum simulation problems; Zhen Zhang, now my wife, had many discussions with me. There were also previous group members and visitors whose stay had brief overlap with mine or I met in other occasions I would like to thank, Shi-Liang Zhu, Wei Yi, Bin Wang, Zhaohui Wei, Yue Wu, Emily Lichko. I am also very grateful to the whole graduate class of 2008 for being so nice and kind. I will always remember Paul and Arina Bierdz's Thanksgiving dinners, Matthew Bales and Amanda Boomer's Halloween parties and many Rock Band nights, Chris Fink and his wife Chrissie's clear and patient explaination of football rules, Alex Burgers and Evangeline Ruth's tailgating parties, and all kinds of help from Ryo Saotome, Michelle Adan, Sarah Anderson and many others. I would also like to thank the fellow asian students, Langechuan Liu for being an interesting roommate, Joon Shin for bringing joy to everyone before his vanishment, Bo Zhang for many airport rides, Cheng Peng, Yifan Zhang and Li Zhang for help in one way or another. Also I am grateful to many PKU alumni who offered much help, Zhichen Zhao, Jingjing Li, Anbo Chen and Hang Chi. There are a lot of other friends I could not mention due to space limitation.

Finally I wish to thank my family. I thank my parents for respecting my choices. I thank my wife for emotional support and encouragement over the years. Without her winters in Michigan would have been a lot more bitter.

TABLE OF CONTENTS

LIST OF FIGURES

LIST OF APPENDICES

ABSTRACT

Quantum technology with atomic, molecular and optical systems has advanced to a stage that single particles can be manipulated precisely so that quantum information processing is no longer elusive. In fact, a great number of quantum information protocols have been demonstrated with small scaled systems. The remaining task is to build large scale practical devices. However it turns out that scaling up is highly nontrivial in the quantum world. A protocol valid in principle could face enormous technical challenges when the system size is increased. Therefore new ideas and smart designs that bypass the technical obstacles are extremely useful in this field.

In this dissertation we tackle several specific problems in quantum information processing with trapped ions and cold atomics gases. For ions, we first present a scalable implementation scheme for the recently proposed concept of Boson sampling, which holds the promise of outperforming classical computers in the near future. The scheme is based on the technically mature linear Paul trap and the transverse motional phonons of the ions are manipulated with laser to perform sampling. A complete recipe is provided and the technical requirements are discussed.

Then we go back to the conventional circuit model for computation and discuss a method to perform individual ion addressing quantum gates with Gaussian beams. We describe the so-called spatial refocusing technique to significantly narrow down the beams with coherent interference.

We also extend the original quantum gate formalism to include the effect of micromotion. We

demonstrate high fidelity gates in the presence of significant micromotion. This paves the way to the development of a two dimensional ion crystal quantum processor with hundreds of ions inside a single trap.

On the other hand, we explore precision measurement with a cold atom interferometer. Combining a spin-spin interaction Hamiltonian and coherent spin rotation pulses, we construct optimized pulse sequences for spin squeezing to approach the Heisenberg limit of noise.

Finally we investigate the general problem of state detection with faulty detectors. We develop a statistical procedure to recover the true correlation from noisy data.

CHAPTER I

Introduction

1.1 Motivation

From abacuses to transistors, various physical systems have been used to construct devices for computing–computers. It is natural to assume that physical laws of the world we are in determine the capabilities of the computing machines, which as part of the physical world are certainly governed by those laws. However, starting in the 1930s, Alan Turing and Alonzo Church's foundational work in the theory of computation established the belief that all kinds of physical devices essentially have the same level of computing power. Thus physics and computation had remained two diverged roads. An interesting turn of the situation started in 1970s, when researchers tried to generalize classical information theory to quantum systems. The ideas of universal quantum computers and quantum simulators were envisioned by pioneers like Feynman and Deutsch in the 1980s [1, 2]. Research along this direction led to a series of discoveries, to name a few, quantum cryptography [3], fast quantum algorithms [4], and the celebrated Shor's algorithm [5]. Inspired by these exciting discoveries, quantum information science has become a burgeoning interdisciplinary

field, uniting the efforts of the physics and computer science communities.

Just as any other interdisciplinary field, researchers with different background and interest approach the subject from different perspectives. In the field of quantum information, there are quantum algorithm designers, quantum communication protocol designers, investigaters of fundamental properties of entanglement, experimentalists constructing quantum-enhanced measurement devices, quantum computer builders, etc. This dissertation focuses on problems in the physical realization of quantum information processing with Atomic, Molecular and Optical (AMO) systems, in particular with trapped ions and cold atom gases. Major topics covered include implementation of a non-traditional paradigm of quantum computing–boson sampling, trapped ion phase gate design and improvement, efficient spin squeezing for precision measurement and quantum state reconstruction.

1.2 Background

Before we dive into detailed discussions of the major topics, we briefly review the physical platforms considered, i.e. trapped ions and cold atom gases. Both systems have been utilized for a wide range of purposes from quantum simulation/computation to testing the foundations of quantum mechanics. We will only touch an extremely small part of the knowledge that is most relevant for this dissertation. For trapped ions, the introduction emphasizes quantum gate design and for cold gases the application in precision measurement is the focus.

1.2.1 Trapped Ion Quantum Gates

Trapped atomic ions have proven to be an ideal platform for quantum information processing. Electric fields are engineered to form a three dimensional trap for charged atomic ions. Suppose the electric potential has the form $\Phi(x,,y,z) = \alpha x^2 + \beta y^2 + \gamma z^2$. One of Maxwell's equations in a region with no charge says $\nabla^2\Phi = 0$, which means $\alpha+\beta+\gamma = 0$. Thus there exists no real three dimensional electric trapping potential. Experimentally radio frequency (r.f.) electric fields are employed to generate an effective trap within the $x-y$ plane and the potential along the other direction z is a pure static trapping potential. The overall potential is $\Phi(x,,y,z) = \alpha\cos(\Omega t)(x^2-y^2) - \frac{\gamma}{2}(x^2+y^2) + \gamma z^2$ where Ω is in the radio frequency regime (around 1GHz) and $\gamma > 0$. If one integrates out the high frequency dynamics and focus on the low frequency effective physics, such an r.f. potential results in a trap along both x and y directions, i.e. $\Phi(x,,y,z) \approx \bar{\Phi}(x,,y,z) = \alpha'(x^2+y^2)+\gamma z^2$ where $\alpha \gg \alpha' > 0$ and $\bar{\Phi}(xy,z)$ is a time independent harmonic potential. Typically α' and γ are on the order of $1-10$MHz level. See [6] for a more experimentally oriented account of ion traps. For ions sitting close to the z-axis, i.e. $x, y \approx 0$, the micromotion with a characteristic frequency Ω in the r.f. regime becomes negligible and the harmonic approximation is very accurate. So typically traps are designed so that $\alpha' > \gamma$ and ions will crystallize along the z-axis when cooled, as shown in Fig. 1.2.1.

Usually atomic species with two valence electrons are used. After loosing one electron the internal level structure of the ion is similar to that of a single valence electron atom. One then identifies two internal levels as the qubit states, resulting in a chain of qubits well separated in space. Using laser beams with appropriate frequency one can manipulate the states of the qubits, for example, initializing all the qubits to the same state through optical pumping, rotating the qubits' states on the Bloch sphere, reading out the qubit state, etc. If the laser beams are focused to single qubits,

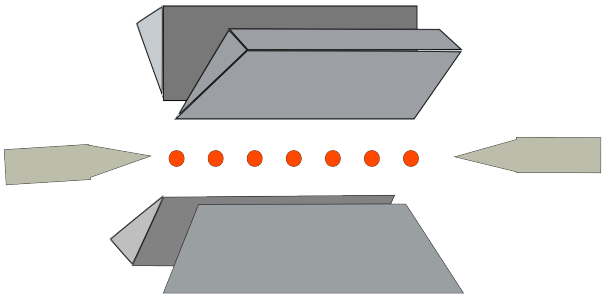

Figure 1.2.1: Illustration of a linear ion trap.

all these operations can be performed on one of the qubits without touching the rest.

For the purpose of universal quantum computing, one still needs a two-qubit entangling operation. This can be done by utilizing the Coulomb interaction between the ions. The earliest proposal is due to Cirac and Zoller [7] and was demonstrated experimentally one decade ago [8]. There exists a more robust type of gate called Molmer Sorensen gate [9] which requires no ground state cooling and thus became more popular than the original Cirac-Zoller gate. In this dissertation we will mainly work with the fast and scalable controlled phase gate mediated by transverse motional modes proposed in [10, 11]. We outline the basic idea below. The key ingredient is a laser induced spin-dependent force described by the Hamiltonian

$$H = \sum_{n=1}^{N} \hbar\Omega_n \cos\left(\Delta k \cdot x_n + \mu t\right) \sigma_n^z \tag{1.2.1}$$

where x_n is the n-th ion's displacement operator along x-direction (perpendicular to the trap axis z) and σ_n^z acts on the qubit space of the n-th ion. The force is induced by a pair of Raman beams with effective wave-vector $\Delta\vec{k} = \vec{k}_1 - \vec{k}_2 = \Delta k\,\hat{x}$ and detuning $\mu = |\omega_1 - \omega_2|$. We can expand the Coulomb interaction upto second order and together with the external trapping the toal potential

energy is $\vec{x}^\dagger A\vec{x}/2$ where $\vec{x}$ denotes the vector of x-coordinates. Using a canonical transformation to diagonalize the potential [12] we obtain normal coordinates $\vec{q}$ defined by $\vec{x}^\dagger A\vec{x}/2 = \vec{q}^\dagger D\vec{q}/2$ with D a diagonal matrix satisfying $AV = VD$, i.e. $A = VDV^\dagger$. The diagonal elements of D gives the normal mode frequencies $D_{kk} = M\omega_k^2$ (M is the mass of one ion). Now we can expand the x-coordinates with the normal mode operators

$$\begin{aligned}
\Delta k \cdot x_n &= \Delta k \cdot \sum_{k=1}^{N} V_{nk} q_k \\
&= \Delta k \cdot \sum_{k=1}^{N} V_{nk} \sqrt{\hbar/(2M\omega_k)} \left(a_k + a_k^\dagger\right) \\
&\equiv \sum_{k=1}^{N} V_{nk} \eta_k \left(a_k + a_k^\dagger\right) \\
&\equiv \sum_{k=1}^{N} g_n^k \left(a_k + a_k^\dagger\right)
\end{aligned}$$

where we defined the Lamb-Dicke parameter for mode k as $\eta_k \equiv |\Delta k| \sqrt{\hbar/2M\omega_k}$ and the coupling constant between the n-th ion and the k-th normal mode $g_n^k \equiv V_{nk}\eta_k$. Assuming the Lamb-Dicke condition $\eta_k = |\Delta k| \sqrt{\hbar/2M\omega_k} \ll 1$, we can use η_k as small parameters to expand the Hamiltonian Eq. (1.2.1) and keep only terms linear in η_k,

$$\begin{aligned}
H &= \sum_{n=1}^{N} \hbar\Omega_n \cos\left(\Delta k \cdot x_n + \mu t\right) \sigma_n^z \\
&= \sum_{n=1}^{N} \sum_{k=1}^{N} \hbar\Omega_n \cos\left(V_{nk}\eta_k \left(a_k + a_k^\dagger\right) + \mu t\right) \sigma_n^z \\
&= -\sum_{n=1}^{N} \sum_{k=1}^{N} \hbar\Omega_n \sin\left(\mu t\right) V_{nk}\eta_k \left(a_k + a_k^\dagger\right) \sigma_n^z + O\left(\eta_k^2\right).
\end{aligned}$$

Switching to the interaction picture with respect to $H_0 = \sum_k \frac{M\omega_k^2}{2} a_k^\dagger a_k$, we replace a_k and $a_k^\dagger$ with

$a_k e^{-i\omega_k t}$ and $a_k^\dagger e^{i\omega_k t}$,

$$H_I \approx -\sum_{n=1}^{N}\sum_{k=1}^{N}\hbar F_n(t) g_n^k \left(a_k^\dagger e^{i\omega_k t} + a_k e^{-i\omega_k t}\right)\sigma_n^z \tag{1.2.2}$$

where we defined $F_n(t) \equiv \Omega_n \sin(\mu t)$ for convenience.

From the Magnus formula we know that the evolution operator corresponding to the Hamiltonian Eq. (1.2.2) contains in its exponent only the following terms, $a_k^\dagger \sigma_n^z$, $a_k \sigma_n^z$, and $\left[a_k \sigma_l^z, a_k^\dagger \sigma_n^z\right] = \sigma_l^z \sigma_n^z$. We can then write down the evolution operator as

$$U(\tau) = \exp[i\sum_n \phi_n(\tau)\sigma_n^z + i\sum_{l<n}\phi_{ln}(\tau)\sigma_l^z\sigma_n^z] \tag{1.2.3}$$

with $\phi_n(\tau)$ and $\phi_{ln}(\tau)$ to be determined from the Schrödinger equation $i\frac{\partial U}{\partial t} = H_I \cdot U$. After some calculation we obtain

$$\phi_n(\tau) = \frac{1}{i}\sum_k [\alpha_n^k a_k^\dagger - \alpha_n^{k*} a_k]$$

with $\alpha_n^k(\tau) = i\int_0^\tau F_n(t) g_n^k e^{i\omega_k t} dt$ and

$$\phi_{ln} = 2\int_0^\tau \int_0^{t_2} \sum_k F_l(t_2) g_l^k g_n^k F_n(t_1) sin[\omega_k(t_2 - t_1)] dt_1 dt_2.$$

The conditional phase flip gate (CPF) is defined to be $U_{\text{CPF}} \equiv \exp\left(i\sigma_i^z \sigma_j^z \pi/4\right)$. Comparing to Eq.(1.2.3) we should engineer the pulse shape $\Omega_n(t)$ and choose an appropriate gate time τ and Raman detuning μ so that $\phi_n(\tau) = 0$ for all n and $\phi_{ln}(\tau) = \pi/4$ if the set $\{l, n\}$ is idential to $\{i, j\}$ and $\phi_{ln}(\tau) = 0$ otherwise. In practice this can be done by choosing a parametric form of $\Omega_n(t)$, e.g. a piecewise constant function, and optimizing the gate fidelity over the parmeter space. With

the evolution operator Eq.(1.2.3) in hand it is straightforward to calculate the gate fidelity. There are different definitions of the fidelity and we will use

$$F = \langle \Psi_0 | \left(U_{\mathrm{CPF}}\right)^{\dagger} \rho_r U_{\mathrm{CPF}} | \Psi_0 \rangle$$

where $|\Psi_0\rangle$ is the initial state before applying the gate (usually taken to be the product state $|+\rangle_i \otimes |+\rangle_j$) and $\rho_r = tr_m\{U(\tau)|\Psi_0\rangle\langle\Psi_0|U(\tau)^{\dagger}\}$ is the actual spin state after the operation of $U(\tau)$, with the motional states traced over. The complication comes from the finite temperature of the motional degrees of freedom. We will offer a simple treatment in Appendix A.

1.2.2 Precision Measurement with Cold Atom Gases

Trapped cold atom interferometers have turned out a suitable platform for precision measurement. In contrast to trapped ions, neutral atoms cannot be confined with electric fields. One instead uses optical or magnetic fields to cool and trap the atoms. Typically around 10^5 atoms form a cloud inside a trap. We also identify two internal atomic levels as the bases for interferometry, analogous to the two ports of an optical interferometer. Note that precision measurement schemes for cold gases also apply to trapped ions but cold gases are more favorable since the particle number is a lot larger, resulting in a larger precision gain as we will see later. Each two level system is often mapped to a spin with $S = 1/2$ which is a more intuitive object. So the trapped gas is equivalent to a collection of about $N \approx 10^5$ spins. Due to the lack of distinguishability the system remains in the permutation invariant subspace with total spin $J = N/2$, i.e. spanned by $|J = N/2, J_z\rangle$ with $J_z = -J, -J+1, \cdots, J$. If the particles are not entangled, for example in a spin coherent state with all the spins pointing to the $x+$ direction, the tip of the total spin vector fluctuates quantum mechanically with magnitude $\Delta J_y = \Delta J_z = \sqrt{J/2}$, see Fig. 1.2.2 left panel for example. This noise

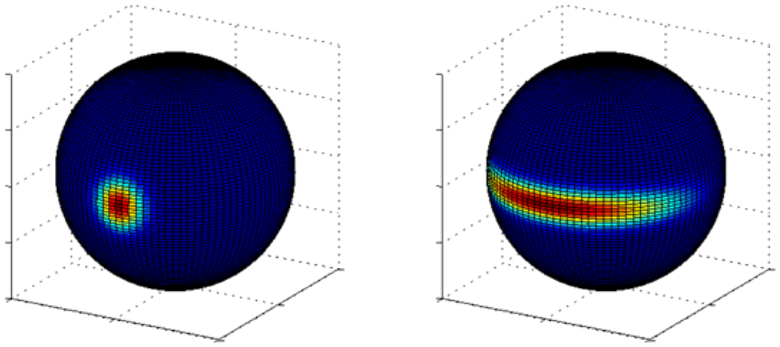

Figure 1.2.2: Quasi-probability distribution of the spin vector for a spin coherent state (left panel) and a spin squeezed state (right panel).

gives rise to the standard quantum limit for the measurement precision of the spin rotation angle around the y or z axis. Although quantum mechanics places the constraint that $\Delta J_y \cdot \Delta J_z \geq J/2$ we can redistribute the noise between y and z directions such that $\Delta J_z < \sqrt{J/2}$ and $\Delta J_y > \sqrt{J/2}$ to achieve a higher rotation sensitivity along the y axis, as shown in Fig.1.2.2 right panel. One figure of merit is the squeezing parameter $\xi^2 = N\frac{\langle J_z^2\rangle}{\langle J_x\rangle^2}$, inversely proportional to the signal-noise ratio squared. For the spin coherent state $\xi^2 = 1$. Interferometry conducted with a squeezed state satisfying $\xi^2 < 1$ can surpass the stand quantum limit. This is the motivation for creating the so-called spin squeezed states.

Since Hamiltonians linear in the spin operators S_x, S_y, S_z only induce rotation of the spin vector, a nonlinear interaction S_i^2 is a necessary ingredient for squeezing. Ideally the two-axis twisting Hamiltonian $H_{\mathrm{TAT}} = \chi\left(S_i^2 - S_j^2\right)$ where i and j are orthgonal directions can create a squeezed state that saturates the Heisenberg limit, i.e. $\xi^2 \propto 1/N$. However such an interaction is usually not naturally present in cold gases. The simpler one-axis twisting Hamiltonian $H_{\mathrm{OAT}} = \chi S_i^2$ that corresponds to two-body spin-spin interaction can produce a slightly inferior state with $\xi^2 \propto 1/N^{2/3}$. We will cover a novel technique to enhance H_{OAT} to approach the performance of H_{TAT} in Chap-

ter V.

1.3 Outline of Dissertation

To orient the readers, we provide a brief outline of the contents of this dissertation. Chapters II, III and IV focus on the trapped ion platform. Chapter II discusses the implementation of a boson sampler which is a novel special-purpose analog quantum computer dedicated to the task of boson sampling. A boson sampler holds the promise of outperforming classical computers in the near future and is currently attracting a lot of interest. Our proposal can hopefully help the trapped ion community scale up the sampler size. In Chapter III we consider the issue of individual ion optical addressing and analyze the spatial refocusing approach which is to construct narrow pulses with a few Gaussian wavepackets. Advantages and limitations of the new approach are discussed. Chapter IV extends the quantum gate formalism to the regime with significant micromotion. Traditionally ion micromotion induced by AC electric fields has to be avoided because it is hard to control. This limits the ions to the saddle points/line of the trap. We will demonstrate how the micromotion can be taken into account in the design of quantum gates so that we no longer need to avoid micromotion. This opens up the possibility of holding a lot more ions inside a single trap and could become a new paradigm for trapped ion quantum computers.

Chapter V discusses spin squeezing for cold atom precision measurement. We will make better use of the Hamiltonian components available to enhance squeezing. Numerical optimization techniques are employed to find a pulse sequence that squeezes much better than the naive approach. The technique does not require complicated experimental setup and can apply readily in experiments. Chapter VI deals with the general issue of correcting measurement errors in state detection. Statistical analysis is performed to figure out the distortion of data brought by faulty detectors and

simple methods to reconstruct the state are presented.

The last chapter will conclude the dissertation and discuss future directions for the topics covered.

CHAPTER II

Boson Sampling with Trapped Ions

2.1 Introduction

What is the ultimate computational power of physical devices? That is a deep question of great importance for both physics and computer science. The famous extended Church-Turing thesis (ECTT) postulates that a (classical) probabilistic Turing machine can efficiently simulate the computational power of any physical devices ("efficiently" here means with a polynomial overhead) [13]. The recent development in quantum computation brings doubt to the ECTT with discovery of superfast quantum algorithms. The most well known example is Shor's algorithm to factorize a large number in polynomial time with a quantum computer [5]. Classically, whether factoring is hard is not settled (a "hard" problem means its solution requires exponential time). No efficient classical algorithm has been found yet to solve factoring, but it wouldn't be very surprising if one finds one as this will not induce dramatic change to the computational complexity theory.

Recently, Ref. [13] introduces another problem, called Boson sampling, which is hard for classi-

cal computers but can be solved efficiently with a quantum machine. Boson sampling is defined as a problem to predict the probabilities of the measurement outcomes in the Fock basis for M Bosonic modes, which start in definite Fock states and undergo a series of mode mixing defined in general by a unitary matrix. By definition, this problem can be efficiently solved with a quantum machine, but classically its solution requires sampling of a probability distribution given by matrix permanents with an exponentially large number of possible outcomes. Computation of the matrix permanent is known to be $\#P$-hard (much harder than the more well-known class of the NP-hard problems) [14]. Ref. [13] rigorously proved that Boson sampling is classically intractable unless the so-called polynomial hierarchy in the computational complexity theory collapses, which is believed to be extremely unlikely. In this sense, compared with the factoring problem, although Boson sampling has no immediate practical applications, it is a problem much harder for classical computers to solve. A demonstration of Boson sampling with a quantum machine thus constitutes an effective disproof of the famous ECTT. Because of this far-reaching theoretical implication, experimental demonstration of the Boson sampling has raised strong interest recently. Several publications this year have reported proof-of-principle demonstrations of the Boson sampling with up to three photons [15–18]. The key challenge for the next-step experiments is to scale up the number of Bosons. The demonstration using photons based on the spontaneous parametric down conversion source has difficulty in terms of scalability [15–18]. The success probability decreases very rapidly with the number of photons due to the probabilistic nature of the single-photon source and the significant photon loss caused by the detector and the coupling inefficiencies. This, in practice, limits the number of Bosons below 10, which is still within the simulation range of classical computers.

In this chapter, we describe a scalable scheme to realize Boson sampling using the transverse phonon modes of trapped ions. Compared with the implementation using photons, this scheme

has the following desirable features: First, the Fock states of the phonons can be prepared in a deterministic fashion and there is no limitation to the number of Bosons that one can realize with this system. We encode the Bosons using the local transverse phonon modes [11], and the state initialization can be done through simple Doppler cooling and one step of the sideband cooling that applies to any number of ions. Second, we find a technique to do projective detection of the phonon numbers for all the ions through sequential spin quantum jump measurements. This gives an implementation of number-resolving phonon detectors with near perfect efficiency, much higher than the efficiency of typical single-photon detectors. Finally, we prove that universal coherent mixing of different phonon modes can be achieved through a combination of the inherent Coulomb interaction and simple laser-induced phase shifts of the ions. Through this scheme, it is feasible to realize Boson sampling for tens of phonons with the state-of-the-art trapped ion technology. This scale has gone beyond the simulation capability of any classical computers and corresponds to the most interesting experimental region for test of the ECTT [19, 20].

2.2 Basic Idea

The problem of Boson sampling is defined as follows: we have M input Bosonic modes a_i ($i = 1, 2, ..., M$), which undergo coherent mode mixing described in general by a unitary matrix Λ, with the output modes given by $b_i = \sum_j^M \Lambda_{ij} a_j$. The input modes are prepared in a Fock (number) state $|\mathbf{T}\rangle = |t_1, t_2, ..., t_M\rangle$, where t_i is an integer denoting the occupation number of the mode a_i. We measure the output modes b_i in the Fock basis and the probability to get the outcome $|\mathbf{S}\rangle =$

$|s_1, s_2, ..., s_M\rangle$ is given by [13, 21]

$$P(\mathbf{S}|\mathbf{T}) = \frac{\left|Per\left(\Lambda^{(\mathbf{S},\mathbf{T})}\right)\right|^2}{\prod_{j=1}^{M} s_j! \prod_i^M t_i!} \tag{2.2.1}$$

where $Per(\cdot)$ denotes the matrix permanent and $\Lambda^{(\mathbf{S},\mathbf{T})}$ is a sub-matrix of Λ formed by taking s_j copies of the j-th column and t_i copies of the i-th row of the matrix Λ. Since the total number of Bosons is conserved $N = \sum_i^M a_i^\dagger a_i = \sum_j^M b_j^\dagger b_j$, the sub-matrix $\Lambda^{(\mathbf{S},\mathbf{T})}$ has dimension $N \times N$. Due to the hardness to calculate the matrix permanent, it becomes impossible to sample the probability distribution $P(\mathbf{S}|\mathbf{T})$ with any classical computer when the number of Bosons N increases beyond $20 \sim 30$. An experimental demonstration of a quantum machine that can successfully perform this job therefore provides strong evidence against the ECTT.

2.3 Trapped Ion Realization

To realize Boson sampling with trapped ions, we consider a chain of ions in a linear Paul trap with the transverse trapping frequency ω_x significantly large than the axial one ω_z. The Bosons are represented by the local transverse phonon modes a_i associated with each ion i ($i = 1, 2, ..., M$), all with the oscillation frequency ω_x. The Coulomb interaction between the ions introduces a small perturbation to the oscillation frequency of the local phonon modes, with the interaction Hamiltonian described by [22, 23]

$$H_c = \sum_{1 \le i < j \le M} \hbar t_{i,j} \left(a_i^\dagger a_j + a_i a_j^\dagger\right), \tag{2.3.1}$$

where the hopping rates $t_{i,j} = t_0/\left|z_{i0} - z_{j0}\right|^3$ and $t_0 = e^2/\left(8\pi\varepsilon_0 m\omega_x\right)$. Here, z_{i0} denotes the axial equilibrium position of the ith ion with mass m and charge e. The Hamiltonian (1) is valid under the condition $t_{i,j} \ll \omega_x$, which is always satisfied for the parameters considered in this chapter. To make the scheme more scalable and eliminate the challenging requirement of resolving phonon sidebands for a large ion chain, we use the local transverse phonon modes to represent the target Bosons instead of the conventional normal modes.

To initialize the local phonon modes a_i to the desired Fock states, first we cool them to the ground state by laser cooling. The routine Doppler cooling achieves a temperature $T_D \sim \hbar\Gamma/\left(2k_B\right)$ (Γ is the natural bandwidth of the excited state and k_B is the Boltzmann constant), with the corresponding thermal phonon number $\bar{n}_x = k_B T_D/\hbar\omega_z \sim \Gamma/\left(2\omega_x\right)$, which is about $1 \sim 2$ under typical values of $\omega_x \approx 2\pi \times (5 \sim 10)$ MHz and $\Gamma \approx 2\pi \times 20$ MHz. The sideband cooling can further push the transverse modes to the ground state with $\bar{n}_x \approx 0$ [24–27]. For the axial modes, we only require their thermal motion to be much less than the ion spacing, which is satisfied already under routine Doppler cooling. As all the local transverse modes have the same frequency (with $t_{i,j} \ll \omega_x$), we only need to apply one step of the sideband cooling independent of the number of ions, with the laser detuning set at $-\omega_x$. The off-resonant process in the sideband cooling limits $\bar{n}_x \sim \gamma/\omega_x$, where γ is the rate of the sideband cooling which needs to be comparable with the phonon hopping rate $t_{i,i+1}$. For a harmonic trap, we take $l_0 = \left[e^2/\left(4\pi\varepsilon_0 m\omega_z^2\right)\right]^{1/3}$ as the length unit so that the ion spacings in this unit take universal dimensionless values (of the order of 1) independent of the ion species and the trap frequency [12]. The hopping rate $t_{i,i+1} \sim t_0/l_0^3 = \omega_z^2/\left(2\omega_x\right)$ and the thermal phonon number after the sideband cooling $\bar{n}_x \sim t_{i,i+1}/\omega_x \sim \omega_z^2/\left(2\omega_x^2\right) < 10^{-2}$ with a typical $\omega_z \approx 2\pi \times (0.3 \sim 1)$ MHz. After cooling of all the transverse modes to the ground state, we can then set them to any desired Fock states through a sequence of laser pulses blue detuned at ω_x [28]. Note that the ion spacing is about or larger than 10 μm under our choice of the parameters,

and under such a spacing it is reasonable to assume individual addressing of different ions with focused laser beams. The focused beam can prepare different local modes a_i to different Fock states $|n_i\rangle$. For implementation of the Boson sampling, without loss of generality we actually can choose $n_i = 1$, which requires only one pulse for preparation. To make the phonon hopping negligible during the preparation step, the sideband Rabi frequency Ω needs to be large compared with the hopping rate $t_{i,i+1} \sim \omega_z^2/(2\omega_x) \sim 2\pi \times (10 \sim 100)$ kHz, which is easy to satisfy under typical laser power.

After the state initialization, we need to coherently mix different phonon modes. The inherent Coulomb interaction described by the Hamiltonian (1) serves this purpose, however, it is constantly on without a tuning knob and we need to introduce additional control parameters to realize different unitary transformations between the M modes. To achieve this goal, we introduce a simple operation which induces a controllable phase shift for any local phonon mode at any desired time. A laser pulse with duration t_p and detuning δ to the sideband induces an additional Hamiltonian $H_i = \hbar\left(\Omega_i^2/\delta\right) a_i^\dagger a_i$ (Ω_i is the sideband Rabi frequency applied to the target ion i), which gives a phase shift $U_{\phi_i} = e^{i\phi_i a_i^\dagger a_i}$ to the mode a_i with $\phi_i = \Omega_i^2 t_p/\delta$. We choose $\Omega_i^2/\delta \gg t_{i,i+1}$ so that the pulse can be considered to be instantaneous over the time scale of phonon tunneling.

The operation U_{ϕ_i} and the Coulomb interaction H_c together are universal in the sense that a combination of them can make any unitary transformation on the M phonon modes represented by the $M \times M$ matrix Λ. Now we prove this statement. It is known that any unitary transformation Λ on M Bosonic modes can be decomposed as a sequence of neighboring beam-splitter-type of operations and individual phase shifts [29]. The beam splitter operation for the modes $(j, j+1)$ is represented by the Hamiltonian $H_{bs}^{(j)} = \hbar t_{j,j+1}\left(a_j a_{j+1}^\dagger + a_{j+1} a_j^\dagger\right)$. To realize $H_{bs}^{(j)}$, we just need to cut off all the other interaction terms in the Coulomb Hamiltonian given by Eq. (2.3.1) except for a specific pair $(j, j+1)$. This can be achieved through the idea of dynamical decoupling using the fast phase

shifts U_{ϕ_i} with $\phi_i = \pi$ [30]. Note that a Hamiltonian term $H_{ij} = \hbar t_{i,j}\left(a_i a_j^\dagger + a_j a_i^\dagger\right)$ can be effectively turned off for an evolution time t if we apply an instantaneous π-phase shift $U_{\phi_i=\pi}$ at time $t/2$ to the mode a_i to flip the sign of H_{ij} to $-H_{ij}$ for the second half period of the evolution. The interaction Hamiltonian H_c has long-range tunneling, but it decays fast with distance d through $1/d^3$ scaling. If we take the first order approximation to keep only the nearest neighbor tunneling, the Hamiltonian has the form $H_{NN} = \sum_{i=1}^{M-1} \hbar t_{i,i+1}\left(a_i^\dagger a_{i+1} + a_i a_{i+1}^\dagger\right)$. The Hamiltonian H_{NN} can be used to realize the required coupling $H_{bs}^{(j)}$ for an arbitrary j if we apply π phase shifts at time $t/2$ to every other modes in the ion chain except for the pair $(j, j+1)$ as illustrated in Fig. 2.3.1(a). This kind of decoupling can be extended and we can simulate the Hamiltonian H_{NN} (and thus $H_{bs}^{(j)}$) with the original long range Hamiltonian H_c to an arbitrary order of approximation. Suppose we cut the interaction range in H_c to the kth order (i.e., we neglect the terms in H_c that scale as $1/d_{ij}^3$ with $|i-j| > k$), we can shrink the interaction range from k to $k-1$ by applying one step of dynamical decoupling with the pattern of π-phase shifts illustrated in Fig. 2.3.1(b). This step can be continued until one reaches H_{NN} through concatenation of the dynamical decoupling [30]. This proves that the Coulomb interaction Hamiltonian H_c, together with the phase shifts U_{ϕ_i} on single ions, can realize any beam splitter operations and thus be universal for construction of arbitrary unitary operations on the M phononic modes.

We should note that the above proof of universality based on the idea of dynamical decoupling is intuitively straight-forward but may be cumbersome to realize in practice. For a real experiment we suggest using optimization methods to design the control sequence for any given unitary. Alternatively, one can randomly generate a sequence of phase shifters and insert them to the evolution to sample unitaries from the group SU(N) randomly (see Appendix B for a demonstration). Due to the universality of the device we are guaranteed to reach almost any corner of the space SU(N). In both approaches, the truncation of Coulomb interaction range is not necessary.

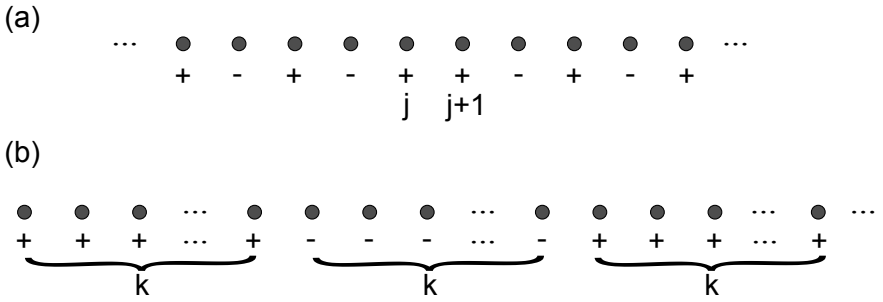

Figure 2.3.1: Control of the tunneling Hamiltonian through the dynamical decoupling. The negative signs in (a,b) denote the set of ions to be applied a π phase shift at half of the evolution time while the positive signs denote the ions left intact. (a) The π-phase pattern to turn off other tunneling terms in H_{NN} except for a neighboring pair $j, j+1$; (b) The π-phase pattern to shrink the tunneling range of the Hamiltonian from k to $k-1$.

The final step of the Boson sampling is detection of all the phononic modes in the Fock basis. The conventional method of measuring the phonon number distribution of a single mode by recording the spin oscillation from red or blue sideband pulses is not applicable here as it cannot measure correlation of different phonon modes in the Fock basis [28]. What we need is a projective measurement of each mode in the Fock basis which gives information of arbitrary high order correlations between different modes. For trapped ions, a projective measurement of its spin (internal) state can be done with a very high efficiency through the quantum jump technique using a cycling transition. However, the spin detection gives only binary measurement outcomes ("dark" or "bright"). We need to figure out a way to perform projective measurements of the Fock states (with multiple possible outcomes) for each phonon mode through the binary spin detection. This is achieved through a consecutive detection scheme with the following steps: (1) First, to illustrate the idea, we consider a single ion with its phonon mode in an arbitrary state $\sum_n c_n |n\rangle$ and its spin prepared in the dark state $|D\rangle$ (see Fig. 2.3.2(a)). (2) Through the well known adiabatic transition technique [31], we make a complete population transfer from $|n+1\rangle|D\rangle$ to $|n\rangle|B\rangle$ for all the Fock components $|n\rangle$ by chirping the frequency of a laser pulse across the red detuning at $-\omega_x$

(see Fig. 2.3.2(b) for the population distribution after this step). (3) We make a carrier transition $|n\rangle|D\rangle \rightleftarrows |n\rangle|B\rangle$ with a $\pi-$pulse to flip the dark and the bright states (see Fig. 2.3.2(c)). (4) After this step, we immediately measure the spin state of the ion through the quantum jump detection. With probability $|c_0|^2$, the outcome is "bright". In this case the measurement is finished and we know the phonon is in the $|n=0\rangle$ state. Otherwise, the spin is in the dark state and the phonon is in the $|n\geq 1\rangle$ components (see Fig. 2.3.2(d) for the population distribution in this case). When the spin is in the dark state, the ion does not scatter any photons during the quantum jump measurement. So its phonon state will not be influenced by this measurement. This feature is important for this consecutive measurement scheme. (5) Now with the phonons in the $|n\geq 1\rangle$ components, we just repeat the steps (2)-(3)-(4) until finally we get the outcome "bright" for the spin detection. We conclude that the phonon is in the Fock state $|n=l\rangle$ if the outcome "bright" occurs (with probability $|c_l|^2$) after l repetitions of the above steps. (6) The above consecutive measurement scheme can be extended straightforwardly to measure M local phonon modes in the Fock basis independently with M ions. The only requirement is that the phonon tunneling between different modes is negligible during the measurement process. The slowest step of the measurement is the quantum jump detection of the ion spin state. Recently, there has been experimental report of high efficiency ($> 99\%$) spin state detection within 10 μs detection time [32]. The typical phonon hopping rate between the neighboring ions in our scheme is in the range of $t_{i,i+1} \sim 2\pi \times (10 \sim 100)$ kHz, and this hopping rate can be significantly reduced during the detection through either an expansion of the ion chain along the z direction right before the direction by lowering the axial trap frequency or application of a few dynamical decoupling pulses to turn off the neighboring tunneling during the detection. As the hopping scales as $1/d^3$, a moderate increase of the effective distance d will significantly reduce the tunneling and push it below the kHz level. We should note that for the Boson sampling algorithm, the output phonon number per mode is typically small (the conventional

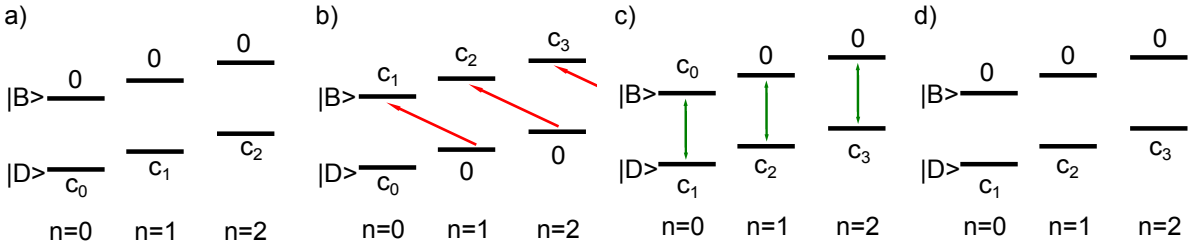

Figure 2.3.2: A consecutive measurement scheme to perform projective detection of the phonon mode in the Fock basis. (a) The initial state configuration right before the measurement. (b-d) The state configuration after the blue sideband transition, the carrier transition, and the quantum jump detection. These three steps are repeated until one finally registers the "bright" state (see the text for details).

photon detectors actually can only distinguish 0 and 1 photons), and the number of repetitions in our consecutive measurement scheme is either zero or very few in most cases.

2.4 Chapter Summary

In summary, we have proposed a scalable scheme to realize the Boson sampling algorithm by use of the local transverse phonon modes of trapped ions. The scheme allows deterministic preparation and high-efficiency readout of the phonon Fock states and universal manipulation of the phonon modes through a combination of inherent Coulomb interaction and individual phase shifts. Several dozens of ions have been successfully trapped experimentally to form a linear chain, and in principle there is no limitation to the number of ions that can be manipulated in a linear Paul trap by use of anharmonic axial potentials [33]. This scheme thus opens the perspective to realize Boson sampling for dozens of phonons with the state-of-the-art trapped ion technology, which would beat the capability of any classical computers and give the first serious experimental test of the extended Church-Turing thesis.

CHAPTER III

Individual Addressing with Spatial Refocusing

3.1 Introduction

Performing useful quantum computation and simulation in the presence of unavoidable noise has been a goal long sought after. Many solid steps have been taken on different physical platforms in the past decade, demonstrating for small systems elementary quantum logic [34–39], simple algorithms [40–42], error correction [43, 44] and quantum simulation [45–48]. While the celebrated error threshold theorem [49] guarantees the fault tolerance of a large scale quantum computer when each single operation error is reduced below a certain limit, this threshold is very hard to satisfy in a typical multi-qubit setting. To fully control the state evolution of the quantum information processor, one needs to pinpoint any individual qubit at will and manipulate it while keeping the others intact. This is a stringent requirement for almost all physical platforms. A lot of efforts have been devoted to the development of individual addressing optical beam delivery and imaging systems [50–53]. Assuming a Gaussian profile of the beam, single qubit addressing typically requires the beam waist to be much smaller than the inter-qubit spacing, which is half the wavelength of the

trapping laser in optical lattices and around one micron in a linear trapped ion chain. So subwavelength focusing beyond the diffraction limit is usually required and this makes it experimentally very challenging.

There have already been many proposals and/or demonstrations in the context of cold atoms in optical lattices [54–61] and linearly trapped ions [62, 63]. To name a few, interference of several Bessel beams were proposed to form a pattern such that all but one atom locate at the nodes of laser profile in [54]; the sharp nonlinear atomic response and position dependent dark states in an electromagnetically induced transparency (EIT) setting was exploited to enable subwavelength selectivity in various proposals [55–59] and experimentally demonstrated very recently [60]; single spin manipulation in an optical lattice with the combination of a well focused level shifting beam and a microwave pulse was demonstrated in [61]. The adaptation of composite pulse refocusing technique widely used in nuclear magnetic resonance [64] and quantum information [30] to trapped ions was considered for single-qubit operation [62] and two-qubit operation with a special form of interaction [63]. Note the two-qubit correction scheme depends on the physical operation being carried out and requires specific form of controllable interaction, and does not reduce error for certain gate realizations.

Our approach is along the line of [54] but in a different setting. We propose and provide detailed analysis for a scheme to reduce crosstalk error and achieve individual addressing with several imperfectly focused laser beams. By applying an array of beams centered at different qubits and controlling their relative amplitudes, we can achieve quantum gates with ideal fidelity even when the beam waist is comparable with or slightly larger than the inter-qubit distance. A reduction of the crosstalk error by several orders of magnitude can be achieved with only moderate increase of the required laser power. The basic idea is reminiscent of the refocusing in NMR, but works in the spatial domain using multiple beams instead of in the time domain. So we call this technique

spatial refocusing. Unlike [63], this technique is universal and works for any quantum gate. We believe it is a valuable addition to the existing toolbox of subwavelength addressing.

3.2 Mathematical formulation

We consider an array of qubits with even spacing a located at the positions x_i $(i = 1, 2, \cdots, N)$. The laser beam used to manipulate the qubits is assumed to have a spatial profile denoted by $g(x - x_i)$ when it is centered at x_i. To have individual addressing, normally we assume the laser is strongly focused so that $g(x_j - x_i) \to 0$ for any $j \neq i$ (i.e., $g(x_j - x_i) = \delta_{ij}$). It remains experimentally challenging to achieve this condition in multi-qubit quantum computing platforms where the spacing a needs to be small to have sufficiently strong interaction. Here, instead of strong focusing, we assume that the laser beams applied to different qubits have relative coherence. To address a single qubit, say qubit i at position x_i, instead of just shining this qubit with $g(x - x_i)$, we apply a number of identical beams centered on its nearby qubits with relative amplitudes denoted by $f(x_j - x_i)$. The total effective laser profile is then the convolution

$$G(x - x_i) = \sum_j g(x - x_j) f(x_j - x_i). \tag{3.2.1}$$

For a given $g(x - x_i)$, we want to find an envelop function $f(x_j - x_i)$ to make $G(x_j - x_i) \to 0$ for any $j \neq i$. It is desirable that $f(x_j - x_i)$ is fast decaying so that in practice we can cut off j in the summation of Eq. (3.2.1) and apply laser beams to only a few of its neighbors. If we take the normalization $g(0) = G(0) = 1$, $f(0)$ then determines the relative increase of the required laser light amplitude, which is desired to be moderate for practical applications.

The solution depends on the laser profile $g(x - x_i)$. To show that the idea works, first we look

at a toy model by assuming $g(x-x_i)$ given by an exponential decay $g(x-x_i)=e^{-\alpha|x-x_i|}$. In this case, two correction beams applied to its nearest neighbors x_{i-1} and x_{i+1} perfectly cancel the residue laser amplitude for all the qubits $j\neq i$. To see this, let us take $f(0)=\beta_0$, $f(x_j-x_i)=\beta_1$ for $j=i\pm1$, and all other $f(x_j-x_i)=0$. If we choose $\beta_0=\left(1+\lambda^2\right)/\left(1-\lambda^2\right)$ and $\beta_1=-\lambda/\left(1-\lambda^2\right)$, where $\lambda\equiv e^{-\alpha a}$, we immediately have $G(x_j-x_i)=\delta_{ij}$. The required increase of the laser power $f(0)=\left(1+\lambda^2\right)/\left(1-\lambda^2\right)$ is moderate even when the original laser profile $g(x-x_i)$ has a significant residue amplitude $\lambda=e^{-\alpha a}$ on the neighboring qubits.

For a general laser profile $g(x-x_i)$, if the number of qubits is large or if the envelop function $f(x_i)$ is fast decaying so that the boundary condition is irrelevant, we can formally solve Eq. (3.2.1) by assuming the periodic boundary condition for the array. In this case, we can take a discrete Fourier transformation of Eq. (3.2.1), which yields $g(k)f(k)=G(k)$. As the target profile $G(x-x_i)$ needs to be a δ-function, $G(k)=1$, and a formal solution of Eq. (3.2.1) is

$$f(x_j-x_i)=\frac{1}{N}\sum_k\frac{1}{g(k)}e^{ik(x_j-x_i)/a}, \tag{3.2.2}$$

where the summation is over $k=\pi n/N$ with $n=-N/2,-N/2+1,\cdots,N/2$. In the limit of large N, $f(x_j-x_i)\approx(1/2\pi)\int_{-\pi}^{\pi}dk\,[1/g(k)]\,e^{ik(x_j-x_i)/a}$.

Now we apply this formalism to practical Gaussian beams, for which $g(x-x_i)=\exp\left[-(x-x_i)^2/w^2\right]$, where w characterizes the width of the beam. The discrete Fourier transformation of $g(x-x_i)$ gives

$$g(k)=\sum_{n\in Z}\exp[-(na)^2/w^2]\exp(-ikn)=\theta_3(k/2,\gamma) \tag{3.2.3}$$

where $\gamma\equiv e^{-a^2/w^2}<1$, and $\theta_3(z,q)\equiv1+2\sum_{n=1}^{\infty}q^{n^2}\cos(2nz)$ is the Jacobi elliptic function. We can do a series expansion with γ, and up to the order of γ^2, $g(k)\approx1+2\gamma\cos(k)+\mathcal{O}(\gamma^4)$ and

$f(x_j - x_i) \approx \left(1+2\gamma^2\right)\delta_{ij} - \gamma\delta_{i\pm1,j} + \gamma^2\delta_{i\pm2,j}$. One can see that the envelop function $f(x_j - x_i)$ decays exponentially by the factor $-\gamma$ as one moves away from the target qubit. This result holds in general. To show this, we write Eq. (3.2.1) into a matrix form $\sum_j M_{nj} f_{ji} = \delta_{n,i}$, denoting x as $x_n = na$ and $g(x_n - x_j)$ as $M_{nj} = e^{-(n-j)^2a^2/w^2} = \gamma^{(n-j)^2}$, where n, j are integers between 1 and N. For large enough positive integers m, $\gamma^m \ll 1$, so we can always cut off at certain m and set terms $\mathscr{O}\left(\gamma^{m+1}\right)$ in M_{nj} to zero. The resulting M_{nj} is then a Toeplitz band matrix with bandwidth $2m+1$ [65]. The solution f_{ji} contains several exponential decay components with different decay constants (see Appendix C for details), but $|-\gamma|$ characterizes the largest decay constant and in the limit of large $|j-i|$ a single term wins out with $f_{ji} \equiv f(x_j - x_i) \sim (-\gamma)^{|j-i|}$. Numerical solution of the matrix equation confirms this (see Fig. 3.2.1(a)). An important implication of this result is that we can set a truncation tolerance error ε and only apply correction beams to those qubits with $\left|f_{ji}\right| > \varepsilon$. That will require about $2\log\varepsilon/\log\gamma = 2(w/a)^2\log(1/\varepsilon)$ beams, independent of the system size. We expect this qualitative behavior to persist for any beam profile that decays quickly with the increase of distance from its center.

The amplitude $f(0)$, characterizing the required laser power, is plotted in Fig. 3.2.1(b) as a function of w/a from exact numerical solution of Eq. (3.2.1). When $w/a \lesssim 1$, γ is small and from a truncation of Eq. (3.2.2) $g(k) \approx 1 + 2\gamma\cos(k)$, we find $f(0) \approx (1/2\pi)\int_{-\pi}^{\pi} dk\,[1/g(k)] \approx 1/\sqrt{1-4\gamma^2}$. In the other region with $w/a \gtrsim 1$, the summation in Eq. (3.2.3) can be approximated with an integration, which yields $g(k) \approx \sqrt{\pi w^2/a^2}e^{-k^2w^2/(4a^2)}$ and therefore $f(0) \approx \frac{2a^3}{\pi^{5/2}w^3}e^{\pi^2w^2/(4a^2)}$. These two analytic expressions, also drawn in Fig. 3.2.1(b) agree well with the exact solution in their respective regions. Note that for $w/a \lesssim 1$, $f(0)$ is close to unity and the cost in the laser power in negligible. For $w/a \gtrsim 1$, $f(0)$ increases exponentially with w^2/a^2, and the scheme becomes impractical when $w^2/a^2 \gg 1$. Our scheme is most effective in the region $w/a \sim 1$, where it allows a reduction of the crosstalk error by several orders of magnitude with just a few correction beams

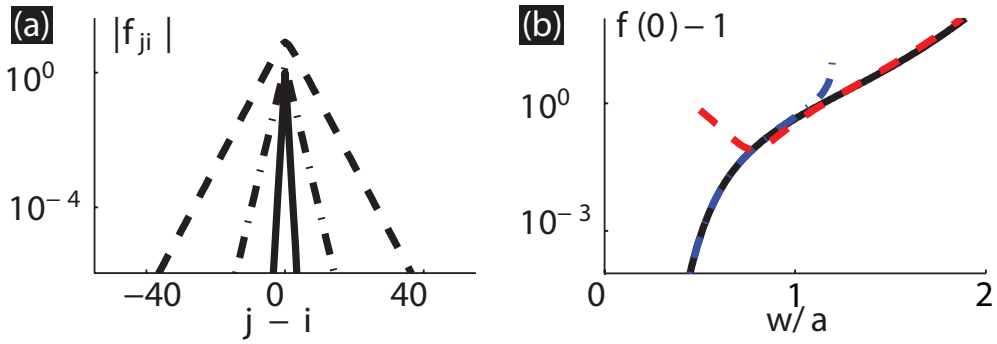

Figure 3.2.1: (a) Envelope function f_{ji} under different Gaussian beam waist ($w/a = 1.5, 1.0, 0.5$ for curves from top to bottom), calculated for a homogeneous chain of 401 qubits. Near the center $j-i=0$, f_{ji} has co-existing components with different decay constants so $\left|f_{ji}\right| = (-1)^{j-i} f_{ji}$ deviates from a straight line on the log plot. Only a few lattice sites away, $\left|f_{ji}\right|$ straightens and the slope matches that of $\gamma^{|j-i|}$ precisely. (b) Amplitude $f(0)$ versus the beam waist w/a. For visibility $f(0)-1$ is plotted. Black solid line is from numerical exact integration of Eq. (3.2.2) and the blue dash-dot (red dashed) line is from the analytic approximation $f(0) = 1/\sqrt{1-4\gamma^2}$ ($f(0) = \frac{2}{\pi^{5/2} w^3} e^{\pi^2 w^2/4}$), valid for the region $w/a \lesssim 1$ ($w/a \gtrsim 1$).

while keeping the cost in the laser power still negligible.

The above analysis extends straightforwardly to higher dimensional systems. Moreover, neither the assumption of homogeneous spacing nor that correction beams center around each qubit is essential. We can always treat the qubits as equidistant if we effectively modify the beam profile $g(x-x_i)$ or M_{nj} according to the actual qubit spacings and the focus positions of the correction lasers. For multi-qubit operations, the relative overhead of spatial refocusing usually becomes lower. For instance, the quantum simulation of arbitrary Ising interaction with N trapped ion qubits requires N^2 well focused laser beams in Ref. [66]. Without perfect focusing, using the scheme here we still only need N^2 beams.

3.3 Spectral refocusing

Instead of using localized beams, an alternative for spatial refocusing is to spectrally decompose the desired amplitude profile and use broad beams of travelling plane waves with varying wave-vectors k to reconstruct a focused beam. Note here we do not use light beams with different frequencies. We simply tilt the traveling wave direction so that the effective spatial periodicity is varied along the system axis. The desired spatial profile $G(x_j - x_i) = \delta_{ij}$, transformed to the momentum space, is a constant function. For N qubits, one can use N plane waves with k evenly spread in the Brillouin zone $[-\pi/a, \pi/a]$ to reconstruct the profile δ_{ij}. We may tilt a travelling wave with a fixed k by different angles with respect to the qubit array to get a varying wave-vector component k_x along the axis. For ion qubits in a harmonic trap, the spacing is inhomogeneous and the exact amplitudes of the components are not even, but can be obtained using the matrix formalism of Eq. (3.2.1). For the plane wave with wave vector k_x^j, the amplitude at position x_n is $M_{nj} = \exp(ik_x^j x_n)$. To get a perfectly focused beam at position x_i, the amplitude f_{ji} for the k_x^j component is given by the solution of the matrix equation $\sum_j M_{nj} f_{ji} = \delta_{ni}$. The maximum $k_x^j = k\sin(\theta_m)$ needs to be comparable with π/a, so we require the laser angle is tunable over a window $[-\theta_m, \theta_m]$, where $\theta_m \approx \sin(\theta_m) \approx \pi/ka$ is typically small. For instance, in an ion trap quantum computer, the ion spacing is about $5\mu m$ and the laser has wavelength about $0.4\mu m$, which gives $\theta_m \sim 0.04 \sim 2.3^\circ$. In Fig. 3.3.1(a), we show the amplitude distribution $f\left(k_x^j\right)$ for 21 ions in a harmonic trap and the associated profile $G(x)$, which is basically a δ-function at ions' positions albeit with small wiggles at other location. This spectral decomposition approach is particularly convenient for quantum simulation where we need to simultaneously apply focused laser beams on each ion [66]. With spectral decomposition, we only need to apply a number of broad plane wave beams that cover all the ions, with their angles tunable in a small window $[-\theta_m, \theta_m]$.

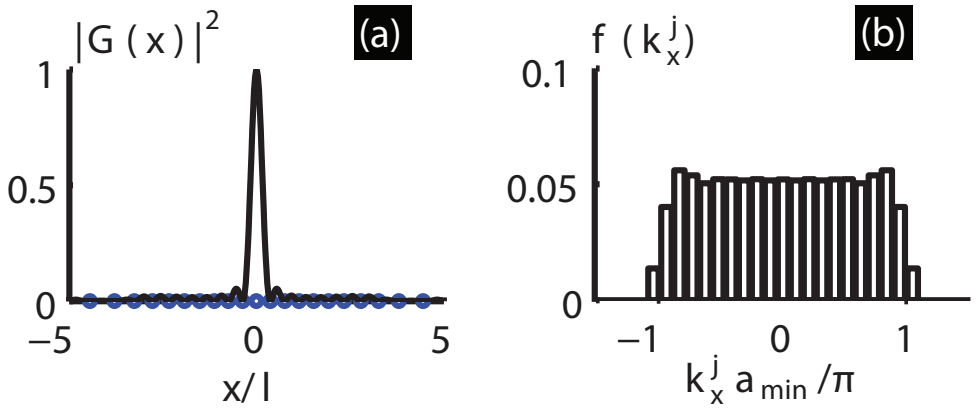

Figure 3.3.1: (a) Intensity (amplitude modulus squared) profile of superposition of 21 plane waves with different wave vector components k_x^j along the chain. Blue circles indicate ions' positions. The unit of position x is $l = \left(\frac{Z^2e^2}{4\pi\varepsilon_0 M\omega_z^2}\right)^{1/3}$, where Ze and M are the charge and mass of each ion, ε_0 the free space permittivity and ω_z the trap frequency along z axis. (b) Amplitudes of spectral components. Here a_{min} is the smallest spacing of ions in the middle of the chain.

3.4 Application example

As an example of application, we consider two-qubit quantum gates in an ion chain. With spatial refocusing, we can perform high fidelity entangling gates even when the Gaussian beam width is comparable with the ion spacing, which significantly simplifies the experimental realization. For two-qubit operations, we need to illuminate only two target ions in the chain. To be concrete, we consider the conditional phase flip (CPF) gate $U_{jn}^{\mathrm{CPF}} = \exp(i\pi\sigma_j^z\sigma_n^z/4)$ mediated by transverse phonon modes as introduced in Chapter I of this dissertation. For the sake of convenience we list the essential formula used again here and for detailed derivation we point the readers to Chapter I. From a practical point of view, one only needs to have Eq. (3.4.1) below in hand to understand this example. We define the trap axis to be the z-direction. The gate is achieved by applying a state-dependent ac-Stark shift on the ions, induced by a pair of Raman beams with frequency detuning μ and wave vector difference $\Delta\mathbf{k}$ along the transverse direction x. The effective Hamiltonian for the

laser-ion interaction is $H=\sum_{j=1}^{N}\hbar\Omega_j\cos\left(\Delta k\cdot q_j+\mu t\right)\sigma_j^z$ where q_j is the j-th ion's displacement operator along x-direction and σ_j^z acts on the qubit space of the j-th ion. Expanding q_j with normal phonon modes [12] $q_j=\sum_k b_j^k\sqrt{\hbar/2M\omega_k}(a_k+a_k^\dagger)$ and assuming Lamb Dicke regime $\eta_k=|\Delta k|\sqrt{\hbar/2M\omega_k}\ll 1$, the interaction picture Hamiltonian under the rotating wave approximation is $H_I=-\sum_{j,k=1}^{N}\hbar\chi_j(t)g_j^k\left(a_k^\dagger e^{i\omega_k t}+a_k e^{-i\omega_k t}\right)\sigma_j^z$, where $g_j^k=\eta_k b_j^k$, $\chi_j(t)=\Omega_j(t)\sin(\mu t)$, b_j^k is the normal mode wavefunction, M is the ion mass, and ω_k is the frequency of the kth motional mode. The associated evolution operator is [10, 11]

$$U(\tau)=\exp\left(i\sum_j\phi_j(\tau)\sigma_j^z+i\sum_{j<n}\phi_{jn}(\tau)\sigma_j^z\sigma_n^z\right), \tag{3.4.1}$$

where

$$\begin{aligned}
\phi_j(\tau) &= \sum_k\left(\alpha_j^k(\tau)a_k^\dagger+h.c.\right)\\
\alpha_j^k(\tau) &= \int_0^\tau\chi_j(t)g_j^k e^{i\omega_k t}dt\\
\phi_{jn}(\tau) &= 2\int_0^\tau dt_2\int_0^{t_2}dt_1\times\\
&\quad\sum_k\chi_j(t_2)g_j^k g_n^k\chi_n(t_1)\sin\left[\omega_k(t_2-t_1)\right]
\end{aligned}$$

This is the key equation of this gate example so let us give more comments to clarify the picture. The evolution operator contains single-spin and two-spin part. The coefficients of the single-spin part $\phi_j(\tau)$ are operators acting on the motional degree of freedom. They give ions an internal state dependent displacement of the motion. This would entangle the spin and motional degrees of freedom. Since we care only about the spin part without measuring the motional states, spin-motion entanglement reduces the purity of the spin states. To get a high fidelity gate we desire a vanishing single-spin part. The coefficients of two-spin part of evolution $\phi_{jn}(\tau)$ are c-numbers

and they only add a phase to the state. Both $\phi_j(\tau)$ and $\phi_{jn}(\tau)$ can be tuned by varying the Raman detuning μ, the gate time τ, and the time-dependent laser Rabi frequency $\Omega_j(t)$. By definition of a controled phase flip gate between ion j and n, one should have $\phi_{jn}(\tau) = \pi/4$ with every other single-spin and two-spin coefficient being zero. To perform such a gate, we shine lasers to ions j and n only, i.e. $\Omega_i = 0$ for $i \neq j,n$, and optimize over μ so that the effective evolution best approximates U_{jn}^{CPF}. For simplicity, here we assume a time independent Ω and pick a relatively long gate time $\tau = 180\tau_0$ ($\tau_0 \equiv 2\pi/\omega_z$ is the trap period). The gate fidelity is quantified by $F = Tr_m \left\langle \Psi_f \right| U(\tau) \left|\Psi_0\right\rangle \left\langle \Psi_0 \right| U^\dagger(\tau) \left|\Psi_f\right\rangle$, where $\left|\Psi_0\right\rangle = \frac{1}{2}\left(\left|0\right\rangle + \left|1\right\rangle\right) \otimes \left(\left|0\right\rangle + \left|1\right\rangle\right)$ is the assumed initial state, $\left|\Psi_f\right\rangle \equiv U_{jn}^{\mathrm{CPF}} \left|\Psi_0\right\rangle$ is the ideal final state and Tr_m indicates tracing over all the motional modes.

Similar to real experiments, we apply Gaussian beams to the target ions j,n. We consider two entangling CPF gates in a 20-ion chain with $\omega_x/\omega_z = 10$, one for two center ions and the other for two ions on one edge, with the beam width about 15% larger than the separation of the two center ions and $2/3$ of separation of the two edge ions. The ion spacings and laser beam width are fixed throughout the calculation. Clearly the condition $w/a \ll 1$ is violated in both cases. All the transverse phonon modes are assumed to be initially in thermal states with the same temperature T such that the center of mass mode has one phonon on average, a typical situation after Doppler cooling. We scan over the Raman detuning μ and for each μ optimize over Ω_j and Ω_n to find the best possible gate fidelity. As expected, without applying correction beams the fidelity of the gate is rather low (see the top curves in Fig. 3.4.1 (a) and (b)). However, keeping all other parameters fixed, the gate error is largely reduced by including only one correction beam and including two correction beams the fidelity gets very close to the ideal case. For the center ions, three correction beams on both sides already reduce the gate error by nearly three orders of magnitude. As shown in Fig 3.4.1(c), the gate infidelity (t1-fidelity) caused by the crosstalk error decreases exponentially

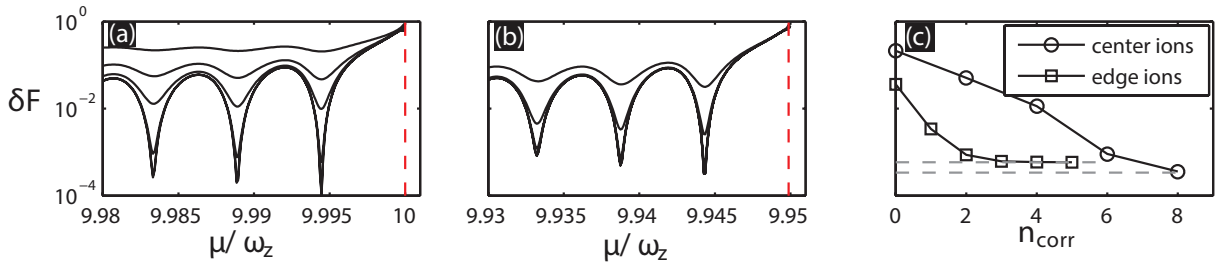

Figure 3.4.1: Panel (a), (b): Infidelity ($\delta F \equiv 1 - F$) of the CPF gate vesus the Raman detuning μ for (a) two ions in the center and (b) two ions on one edge in a 20-ion chain. Vertical dashed lines indicate the position of the transverse phonon modes. The beam waist is set to 15% larger than the minimum spacing (at the center) of ions and about $2/3$ of the maximum spacing (at the edge) of the chain. In (a), curves from top to bottom are for the cases with $0, 2, 4, 6, 8$ correction beams, respectively; in (b), curves from top to bottom are for the cases with $0, 1, 2, 3$ correction beams. Panel. (c): Infidelity under a fixed Raman detuning $\mu = 9.9888\omega_z$ for center ions and $\mu = 9.9387\omega_z$ for edge ions, as a function of the number of correction beams n_{corr}. Dashed lines denote the infidelity under perfect focusing (with zero crosstalk error).

with the number of correction beams, until one approaches the optimal value set by other error sources. Note that with time constant Ω_j and Ω_n, there is an intrinsic gate fidelity due to the lack of control knobs, shown in Fig 3.4.1(c) as dashed lines.

3.5 Experimental implementation and error resistance

The proposed spatial refocusing technique is ready to implement in many quantum computation architectures, such as harmonically trapped ion crystals [33, 45–48] or arrays of micro-traps [67, 68], Rydberg atoms in optical lattices [69], arrays of optical tweezers [70, 71], etc. After measurement of qubit positions, laser focusing positions, and the laser beam profile, one only needs to apply the inverse linear transformation M_{nj}^{-1} to the target beam profile G_j and use the result as input to the beam delivery device. Removing the need of strong focusing, this scheme should significantly simplify the required optics. Another nice feature is that we do not even require each beam to center

at each qubit, as long as the beam positions are known and fixed. The scheme requires coherence between the correction beams. Since Raman beams are used we only need to stabilize the relative phase between the Raman beams. We also note that in small scale systems, the $\log(1/\varepsilon)$ scaling of the number of required correction beams n_{corr} with truncation error is often irrelevant. An array of N coherent pulses should always suffice for the generation of arbitrary laser strength profile for N qubits. So one would never need 10 beams to address 5 qubits.

In practice, spatial refocusing is subject to several types of experimental noise. First of all, the ions are not stationary point particles. Their positions fluctuate thermally and quantum mechanically. Second, the amplitudes and phases of each beam in the array may deviate from the prescription. It is unclear whether the interference is robust to these deviations. We first estimate the position fluctuations of the ions. Take a 21 ion chain as example, the ion spacing vary between 1.02μm and 1.78μm with the smallest spacing in the middle of the chain. Among the axial motional modes the center of mass mode has the lowest frequency, about $2\pi \times 1$MHz and the corresponding oscillator length is $\sqrt{\hbar/2M\omega_z} \approx 5.4$nm. The other axial modes all have higher frequencies and the oscillator lengths are even smaller. Assuming the Doppler cooling limit, i.e. with temperature given by $k_B T = \hbar\Gamma/2$ and the cooling transition linewidth $\Gamma \approx 2\pi \times 20$MHz, the center of mass mode along z contains on average $\frac{k_B T}{\hbar\omega_z} \approx 10$ phonons for a trap with $\omega_z = 2\pi \times 1$MHz. With these realistic data, exact numerical calculation taking all the axial modes into account shows that for each ion the standard deviation of position ranges from 6.5nm to 10nm, at least two orders of magnitude smaller than the inter-ion spacing. So for our purpose here the noise caused by ions' thermal motion is negligible. For the second problem, since the laser beams superpose linearly to give the final refocused pulse, an arbitrary deviation of the j-th pulse's amplitude $\delta f(x_j - x_i)$ only add noise $\delta f(x_j - x_i) g(x - x_j)$ to the final amplitude distribution $G(x - x_i)$. To consider both strength and phase error of the laser, we allow the deviation $\delta f(x_j - x_i)$ to be a complex number. To quantify

the effect of $\delta f(x_j - x_i)$, we parametrize the deviation as follows

$$f(x_j - x_i) + \delta f(x_j - x_i) = f(x_j - x_i)(1 + r_j)\exp(i\phi_j) \tag{3.5.1}$$

where the real numbers r_j and ϕ_j measure respectively the relative amplitude error and phase error of the beam on ion j. Each r_j/ϕ_j is sampled from the normal distribution with zero mean and standard deviation $\Delta r/\Delta\phi$, i.e. $r_j \sim \mathcal{N}(0, \sigma^2 = \Delta r^2)$ and $\phi_j \sim \mathcal{N}(0, \sigma^2 = \Delta\phi^2)$. We define the quantity

$$\varepsilon = \frac{1}{N}\sum_j \left| \left|G(x_j - x_i)\right|^2 - \left|\tilde{G}(x_j - x_i)\right|^2 \right| \tag{3.5.2}$$

to measure the difference of actual and ideal intensity distribution. We now do a numerical simulation to investigte the robustness of the interference. We take a 21-ion chain harmonically trapped and try to address the central ion, $i = 11$. The ideal target is $G(x_j - x_{11}) = \delta_{j,11}$. Assume the addressing beams have a Gaussian profile with width the same as the distance between 11-th and 12-th ion. We randomly sample r_j and ϕ_j 5000 times, calculate ε for each sample and plot the average $\bar{\varepsilon}$ as a function of Δr and $\Delta\phi$, in Fig 3.5.1. We found that the interference pattern is pretty robust. For 5% standard amplitude error and 0.2 radians phase error, the average intensity error $\bar{\varepsilon}$ is still below 1%. In terms of gate infidelity, we did numerical experiments and found that 1% intensity error induces on the order of 10^{-2} (10^{-3}) infidelity for two center ions with $n_{\text{corr}} = 8$ (edge ions with $n_{\text{corr}} = 5$), with every other parameter the same as described in caption of Fig 3.4.1. For 0.5% intensity error, both infidelities are on the 10^{-3} level.

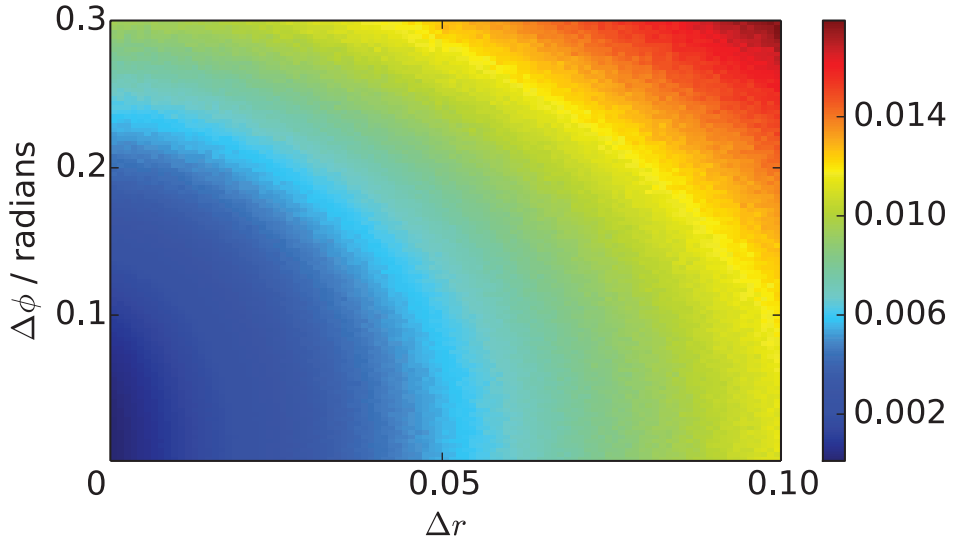

Figure 3.5.1: Average intensity error $\bar{\varepsilon}$ as a function of standard amplitude/phase error $\Delta r/\Delta\phi$. The color encodes value of $\bar{\varepsilon}$. Each point is obtained with 5000 random samples of $r_j \sim \mathcal{N}(0, \sigma^2 = \Delta r^2)$ and $\phi_j \sim \mathcal{N}(0, \sigma^2 = \Delta\phi^2)$.

3.6 Chapter Summary

In summary, we have proposed a spatial refocusing technique to achieve effective individual addressing and reduce crosstalk error in a general multi-qubit platform. The scheme is efficient as the crosstalk error decreases exponentially with the number of correction beams, and the cost in the laser power is modest even when the beam width is comparable with the qubit separation. The scheme works universally for any type of quantum gates and can apply to any quantum computational platform.

CHAPTER IV

Trapped Ion Quantum Gate Design in Presence of Micromotion

4.1 Introduction

Two or three dimensional Paul traps can confine a large number of ions forming a Wigner crystal, which would provide an ideal architecture for scalable quantum computation except for the micromotion, an issue that is widely believed to be the killer for any high fidelity quantum gates. Surprisingly, here we show that the micromotion is not an obstacle at all for design of high fidelity quantum gates, even though the magnitude of the micromotion is significantly beyond the requirement of the Lamb-Dicke condition. Through exact solution of the quantum Mathieu equations, we demonstrate the principle of the gate design under micromotion using two ions in a quadrupole Paul trap as an example. The proposed micromotion quantum gates can be extended to the many ion case and pave a new way for scalable trapped ion quantum computation.

Trapped ions constitute one of the most promising systems for realization of quantum computation. All the quantum information processing experiments so far are actually done in linear Paul traps,

where the ions from a one-dimensional crystal along the trap axis [8, 45, 46, 48, 72–77]. In this configuration, the external radio-frequency (r.f.) Paul trap can be well approximated by a static trapping potential, and the micromotion along the trap axis can be neglected, which is believed to be critical for design of high fidelity quantum gates. However, in terms of scalability, the linear configuration is not the optimal one for realization of large scale quantum computation: first, the number of ions in a linear trap is limited [78, 79]; and second, the linear configuration is not convenient for realization of fault-tolerant quantum computation. The effective qubit coupling in a large ion chain is dominated by the dipole interaction, which is only good for short-range quantum gates because of its fast decay with distance. In a linear chain with short range quantum gates, the error threshold for fault tolerance is very tough and hard to be met experimentally [80, 81].

From a scalability point of view for quantum computation, two or three dimensional Paul traps would be much better than a linear chain, where one can hold a large number of qubits with a high error threshold for fault tolerance, in the range of a percent level, even with just the nearest neighbor quantum gates [81]. Thousands to millions of ions have been successfully trapped to form two or three dimensional Wigner crystals in a Paul trap [82–85] . However, there is a critical problem to use this system for quantum computation, i.e., the micromotion issue. In this high dimensional configuration., the micromotion can not be compensated, and the magnitude of the micromotion for each ion can be significantly beyond the optical wavelength (i.e., outside of the Lamb-Dicke region). As the micromotion is from the driving force of the Paul trap, it cannot be laser cooled. The messy and large-magnitude micromotion well beyond the Lamb-Dicke condition is believed to be a critical hurdle for design of any quantum gate operations in this architecture.

In this chapter, we show that the micromotion surprisingly is not an obstacle at all for design of high-fidelity quantum gates. When the ions form a crystal in a time-dependent Paul trap, they will be described by a set of Mathieu equations. We solve exactly the quantum Mathieu equations in

general with an inhomogeneous driving term and find that the micromotion is dominated by a well-defined classical trajectory with no quantum fluctuation. This large classical motion is significantly outside of the Lamb-Dicke region, however, it does not lead to infidelity of quantum gates if it is appropriately taken into account in the gate design. The quantum part of the Mathieu equation is described by the secular mode with micromotion correction to its mode function. This part of motion still satisfies the Lamb-Dicke condition at the Doppler temperature, which is routine for experiments. We use two ions a quadrupole trap, which have a lot of micromotion, as an example to show the principle of the gate design, and give the explicit gate scheme both in the slow and the fast gate regions using multi-segment laser pulses [10, 11], with the intrinsic gate infidelity approaching zero under large micromotion. We discuss general procedure of the gate design under micromotion, which can work for any number of ions with important implication for large-scale quantum computation.

4.2 Two-Ion Case

To illustrate the general feature of micromotion in Paul traps and the principle of the gate design under micromotion, we consider a three-dimensional (3D) anisotropic quadrupole trap with a time dependent potential $\Phi(x,y,z) = (U_0 + V_0\cos(\Omega_T t))\left(\frac{x^2+y^2-2z^2}{d_0^2}\right) \equiv \alpha(t)(x^2+y^2-2z^2)$ from an electric field oscillating at the r.f. Ω_T, where U_0, V_0 are voltages for the d.c. and a.c. components and d_0 characterizes the size of the trap. We choose a positive U_0 to reduce the effective trap strength along the z direction so that the two ions align along the z-axis. Since the motions in different directions do not couple to each other under quadratic expansion, we focus our attention

on the z direction. The total potential energy of two ions (each with charge e and mass m) is

$$V(z_1, z_2) = -2e\alpha(t)\left(z_1^2 + z_2^2\right) + \frac{e^2}{4\pi\varepsilon_0 |z_1 - z_2|}. \tag{4.2.1}$$

Define center-of-mass (CM) coordinate $u_{\mathrm{cm}} = (z_1 + z_2)/2$ and relative coordinate $u_{\mathrm{r}} = z_1 - z_2$. Without loss of generality, we assume $u_{\mathrm{r}} > 0$ and its average $\bar{u}_{\mathrm{r}} = u_0$. We assume the magnitude of the ion motion is significantly less than the ion separation, which is always true for the ions in a crystal phase. The Coulomb interaction can then be expanded around the average distance $\bar{u}_{\mathrm{r}}$ up to the second order of $|u_{\mathrm{r}} - u_0|$. Under this expansion, the total Hamiltonian $H = p_{\mathrm{cm}}^2/4m + p_{\mathrm{r}}^2/m + V(z_1, z_2)$ is quadratic (although time-dependent) in terms of the coordinate operators $u_{\mathrm{cm}}, u_{\mathrm{r}}$ and the corresponding momentum operators $p_{\mathrm{cm}} = p_1 + p_2$, $p_{\mathrm{r}} = (p_1 - p_2)/2$. The Heisenberg equations under this Hamiltonian H yield the following quantum Mathieu equations respectively for the coordinate operators u_{cm} and u_{r}

$$\frac{d^2 u_{\mathrm{cm}}}{d\xi^2} + (a_{\mathrm{cm}} - 2q_{\mathrm{cm}}\cos(2\xi))\, u_{\mathrm{cm}} = 0 \tag{4.2.2}$$

$$\frac{d^2 u_{\mathrm{r}}}{d\xi^2} + (a_{\mathrm{r}} - 2q_{\mathrm{r}}\cos(2\xi))\, u_{\mathrm{r}} = f_0 \tag{4.2.3}$$

where the dimensionless parameters $a_{\mathrm{cm}} = -16eU_0/\left(md_0^2\Omega_T^2\right)$, $a_{\mathrm{r}} = a_{\mathrm{cm}} + 4e^2/\left(\pi\varepsilon_0 m u_0^3 \Omega_T^2\right)$, $q_{\mathrm{cm}} = q_{\mathrm{r}} = 8eV_0/\left(md_0^2\Omega_T^2\right)$ and the dimensionless time $\xi = \Omega_T t/2$. The driving term $f_0 = 6e^2/\left(\pi\varepsilon_0 m u_0^2 \Omega_T^2\right)$. The quantum operators u_{cm} and u_{r} satisfy the same form of the Mathieu equations (except for the driving term f_0) as for the classical variables. As these equations are linear, we can use the solutions known for the classical Mathieu equation to construct a quantum solution that takes into account of the quantum fluctuation.

It is well known that the solution to the classical Mathieu equation $\frac{d^2}{d\xi^2}v + (a - 2q\cos(2\xi))\, v = 0$ is

a combination of Mathieu sine $S(a, q, \xi)$ and Mathieu cosine $C(a, q, \xi)$ functions, which reduce to the conventional sine and cosine functions when micromotion is neglected [86]. The solution to a homogeneous quantum Mathieu equation $\frac{d^2}{d\xi^2}\hat{u} + (a - 2q\cos(2\xi))\,\hat{u} = 0$ can be described using the reference oscillator technique [6, 87–89]. From the classical solution v and the quantum operator $\hat{u}$, one can introduce the following annihilation operator of a reference oscillator (remember that $\xi = \Omega_T t/2$ is the dimensionless time)

$$\hat{a}(t) = \sqrt{\frac{m}{2\hbar\omega}}\, i\left(v(t)\dot{\hat{u}}(t) - \dot{v}(t)\hat{u}(t)\right), \tag{4.2.4}$$

where ω is a normalization constant typically taken as the secular motion frequency of the corresponding Mathieu equation. In addition, we impose the initial condition for $v(t)$ with $v(t)|_{t=0} = 1$ and $\dot{v}(t)|_{t=0} = i\omega$. The position operator $\hat{u}(t)$ and its conjugate momentum $\hat{p}(t) \equiv m\dot{\hat{u}}(t)$ satisfy the commutator $[\hat{u}(t), \hat{p}(t)] = i\hbar$. From the above definition, one can easily check that $\frac{d}{dt}\hat{a}(t) \propto v\frac{d^2}{d\xi^2}\hat{u} - \hat{u}\frac{d^2}{d\xi^2}v = 0$, so $\hat{a}(t) \equiv \hat{a}$ is a constant of motion. Furthermore, $\hat{a}$ and $\hat{a}^\dagger$ satisfy the standard commutator

$$\left[\hat{a}, \hat{a}^\dagger\right] = (m/2\hbar\omega)\,(i\hbar/m)\,\left(v(t)\dot{v}^*(t) - v^*(t)\dot{v}(t)\right)|_{t=0} = 1.$$

When micromotion is neglected, $v(t) = e^{i\omega t}$ and $\hat{a}$ reduces to the annihilation operator of a harmonic oscillator. In presence of micromotion, $v(t) = C(a, q, \xi) + iS(a, q, \xi)$. The solution to the position operator $\hat{u}$ takes the form

$$\hat{u}(t) = u_0\left(v^*(t)\hat{a} + v(t)\hat{a}^\dagger\right) \tag{4.2.5}$$

where $u_0 \equiv \sqrt{\hbar/2m\omega}$ is the oscillator length.

The above solution gives a complete description of the center-of-mass motion with the operator

$$u_{\rm cm}(t) = u_{0\rm cm}\left(v^*_{\rm cm}(t)\hat{a}_{\rm cm} + v_{\rm cm}(t)\hat{a}^\dagger_{\rm cm}\right), \tag{4.2.6}$$

where $u_{0\rm cm} \equiv \sqrt{\hbar/2m\omega_{\rm cm}}$. The relative motion $u_{\rm r}$ satisfies the inhomogeneous quantum Mathieu equation (4.2.3). To solve it, we let $u_{\rm r} = u'_{\rm r} + \bar{u}_{\rm r}$, where $u'_{\rm r}$ is an operator that inherits the commutators for $u_{\rm r}$ and satisfies the homogenous quantum Mathieu equation and $\bar{u}_{\rm r}$ is a classical variable corresponding to a special solution of the Mathieu equation $\frac{d^2\bar{u}_{\rm r}}{d\xi^2} + (a_{\rm r} - 2q_{\rm r}\cos(2\xi))\,\bar{u}_{\rm r} = f_0$. The special solution $\bar{u}_{\rm r}$ can be found through the series expansion $\bar{u}_{\rm r} = f_0\sum_{n=0}^{+\infty} c_n\cos(2n\xi)$, where the expansion coefficients c_n satisfy the recursion relations $a_{\rm r}c_0 - q_r c_1 = 1$ and $c_n = D_n\left(c_{n-1} + c_{n+1} + c_0\delta_{n,1}\right)$ for $n \geq 1$ with $D_n \equiv -q_r/\left(4n^2 - a_r\right)$. When $a_r \ll 1$ and $q_{\rm r} \ll 1$, which is typically true under real experimental configurations, c_n rapidly decays to zero with $|c_{n+1}/c_n| \approx q_{\rm r}/4\,(n+1)^2$ and we can keep only the first few terms in the expansion and obtain an analytical expression for $\bar{u}_{\rm r}$ (see Appendix D for details). The complete solution of $u_{\rm r}$ is therefore given by

$$u_{\rm r}(t) = u_{0\rm r}\left(v^*_{\rm r}(t)\hat{a}_{\rm r} + v_{\rm r}(t)\hat{a}^\dagger_{\rm r}\right) + \bar{u}_{\rm r}(t), \tag{4.2.7}$$

where $u_{0\rm r} \equiv \sqrt{\hbar/2m\omega_{\rm r}}$.

Now we show how to design high fidelity quantum gates under micromotion. To perform the controlled phase flip (CPF) gate as introduced in Chapter I of this dissertation, we apply laser induced spin dependent force on the ions, with the interaction Hamiltonian described by [11]

$$H = \sum_{j=1}^{2}\hbar\Omega_j\cos\left(k_\delta z_j + \mu_\delta t + \phi_j\right)\sigma^z_j. \tag{4.2.8}$$

where k_δ is the wave vector difference of the two Raman beams along the z direction, μ_δ is the

two-photon Raman detuning, Ω_j (real) is the Raman Rabi frequency for the ion j, and ϕ_j is the corresponding initial phase. In terms of the normal modes, the position operator $z_j = u_{\rm cm} - (-1)^j u_{\rm r}/2$, where $u_{\rm cm}$, $u_{\rm r}$ are given by Eqs. (4.2.6) and (4.2.7). We introduce three Lamb-Dicke parameters, $\eta_{\rm cm} \equiv k_\delta u_0^{\rm cm}$ for the CM mode, $\eta_{\rm r} \equiv k_\delta u_0^{\rm r}/2$ for the relative mode, and $\eta_{\rm mm} \equiv k_\delta \bar{u}_{\rm r}/2$ for pure micromotion. Under typical experimental configurations, $\eta_{\rm cm} \sim \eta_{\rm r} \ll 1$. The parameter $\eta_{\rm mm}$ is a classical variable that oscillates rapidly with time by multiples of the micromotion frequency Ω_T. In Fig. 4.2.1(a), we show a typical trajectory of $\eta_{\rm mm}(t)$. The magnitude of variation of $\eta_{\rm mm}$ is considerably larger than 1. In Fig. 4.2.1(b), we also plot the function $v_{\rm cm}(t)$, which is dominated by the oscillation at the secular motion frequency $\omega_{\rm cm}$ with small correction from the micromotion. The magnitude of $v_{\rm cm}(t)$ is bounded by a constant slightly larger than1. The function $v_r(t)$ has very similar behavior except that $\omega_{\rm cm}$ is replaced by $\omega_{\rm r}$. From this consideration of parameters, we can expand the term $\cos\left(k_\delta z_j + \mu t + \phi_j\right)$ with small parameters $\eta_{\rm cm}, \eta_{\rm r}$, but $\eta_{\rm mm}$ is a big term which needs to be treated exactly. After the expansion, to leading order in $\eta_{\rm cm}$ and $\eta_{\rm r}$, the Hamiltonian H takes the form

$$H \approx -\left[\chi_1(t)\sigma_1^z + \chi_2(t)\sigma_2^z\right]\hat{f}_{\rm cm} - \left[\chi_1(t)\sigma_1^z - \chi_2(t)\sigma_2^z\right]\hat{f}_{\rm r}, \tag{4.2.9}$$

where we have defined

$$\begin{aligned} \hat{f}_\mu &\equiv \eta_\mu\left(v_\mu^*(t)\hat{a}_\mu + v_\mu(t)\hat{a}_\mu^\dagger\right), \\ \chi_j(t) &\equiv \hbar\Omega_j \sin\left[\mu_\delta t + \phi_j - (-1)^j \eta_{\rm mm}(t)\right], \end{aligned} \tag{4.2.10}$$

where the subscript $\mu = $ cm, r. In Eq. (4.2.9), we have dropped the term $\cos\left(\mu_\delta t + \phi_j \pm \eta_{\rm mm}\right)$ which induces single-bit phase shift but is irrelevant for the CPF gate. The evolution operator at

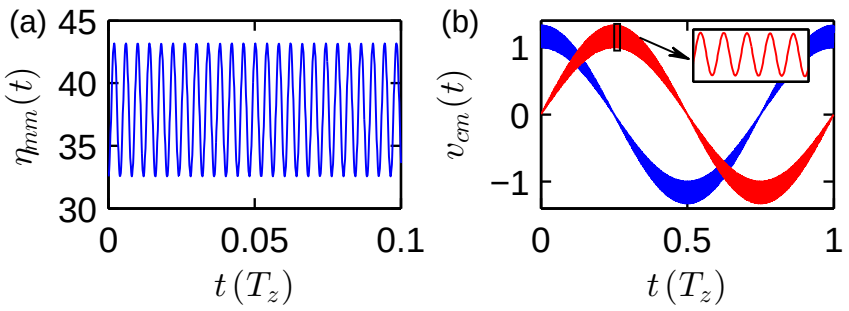

Figure 4.2.1: (a) The time dependent parameter $\eta_{mm}(t)$ and (b) the function$v_{\rm cm}(t)$. The real/imaginary part (blue/red curves) of $v_{\rm cm}(t)$ has even/odd parity as a function of time and looks similar to cos / sin function. Unit of time is the trap frequency $T_z = 2\pi/\omega_{cm}$. The parameters used are: ion mass $m = 9u$ (u is the atomic mass unit); r.f. trap frequency $\Omega_T = 2\pi \times 240$MHz; the characteristic electrode size is $d_0 = 200$ μm; AC/DC voltages, V_0/U_0 are 300V and 21V respectively. The resulting secular trap frequencies are $\omega_{cm} = 2\pi \times 0.965$MHz , $\omega_r = 2\pi \times 3.62$MHz along the z-axis, and $\omega_x = \omega_y = 2\pi \times 20.8$MHz along x- and y-axis.

the gate time τ generated by the Hamiltonian H can be expressed as

$$U(\tau) = D_{\rm cm}(\alpha_{\rm cm}) D_{\rm r}(\alpha_{\rm r}) \exp\left[i(\gamma_{\rm r} - \gamma_{\rm cm})\sigma_1^z \sigma_2^z\right], \tag{4.2.11}$$

where the displacement operator $D_\mu(\alpha_\mu) \equiv \exp\left(\alpha_\mu \hat{a}_\mu^\dagger - \alpha_\mu^* \hat{a}_\mu\right)$ ($\mu =$ cm, r). Let $j_\mu = 1$ for $\mu =$ cm and $j_\mu = -1$ for $\mu =$ r. The displacement α_μ and the accumulated phase γ_μ have the following expression

$$\begin{aligned} \alpha_\mu &= i\eta_\mu \int_0^\tau \left(\chi_1(t)\sigma_1^z + j_\mu \chi_2(t)\sigma_2^z\right) u_\mu(t)\, dt \\ \gamma_\mu &= i\left(\eta_\mu\right)^2 \int_0^\tau dt_1 \int_0^{t_1} dt_2 \mathscr{S}[\chi_1\chi_2] \mathrm{Im}\left[u_\mu(t_1) u_\mu^*(t_2)\right] \end{aligned} \tag{4.2.12}$$

where $\mathscr{S}[\chi_1\chi_2] \equiv \chi_1(t_1)\chi_2(t_2) + \chi_1(t_2)\chi_2(t_1)$.

To realize the CPF gate, we require $\alpha_\mu = 0$ and $\gamma_{\rm r} - \gamma_{\rm cm} = \pi/4$. We normally take $\Omega_1 = \Omega_2 \equiv \Omega$.

Note that even in this case $\chi_1(t_1) \neq \chi_2(t_2)$ with the micromotion term $\eta_{\rm mm}(t)$. This is different from the case of a static trap. From Eq. (4.2.12), we see that $\alpha_\mu = 0$ for a fixed μ gives two complex and thus four real constraints. With excitation of N motional modes, the total number of (real) constraints to realize the CPF gate is therefore $4N+1$ (the condition $\gamma_{\rm r} - \gamma_{\rm cm} = \pi/4$ gives one constraint). To satisfy these constraints, we divide the Rabi frequency $\Omega(t)$ $(0 \leq t \leq \tau)$ into m equal-time segments, and take a constant Ω_β $(\beta = 1, 2, \cdots, m)$ for the βth segment [10, 11]. This kind of modulation can be conveniently done through an acoustic optical modulator in experiments [90]. The Rabi frequencies are our control parameters. For the two ion case, under fixed detuning μ_δ and gate time τ, in general we can find a solution for the CPF gate with $m = 9$ segments. For some specific detuning μ_δ very close to a secular mode frequency, off-resonant excitations become negligible and a solution is possible under one segment of pulse by tuning of the gate time τ, which corresponds to the case of the Mølmer-Sørensen gate [9] generalized to include the micromotion correction.

To characterize the quality of the gate, we use the fidelity $F \equiv tr_\mu \left[\rho_\mu \left|\langle\Psi_0| U_{\rm CPF}^\dagger U(\tau) |\Psi_0\rangle\right|^2\right]$, defined as the overlap of the evolution operator $U(\tau)$ with the perfect one $U_{\rm CPF} \equiv e^{i\pi\sigma_1^z\sigma_2^z/4}$ under the initial state $|\Psi_0\rangle$ for the ion spins and the thermal state ρ_μ for both of the phonon modes. In our calculation, without loss of generality, we take $|\Psi_0\rangle = (|0\rangle + |1\rangle) \otimes (|0\rangle + |1\rangle)/2$.

The essential integral in evaluating $\alpha_{\rm cm/r}$ has the form $I = \int \chi(t) v(t) dt = \int \sin(\mu t + \phi_1 + \Delta k \cdot \bar{u}_{\rm rel}(t)/2) v(t) dt$. Here $v(t)$ and $\bar{u}_{\rm rel}(t)$ contain multiple frequency components. The classical trajectory $\bar{u}_{\rm r}(t)$ contains the secular frequency ω, micro-motion frequencies $n\Omega$, $n\Omega \pm \omega$ for integer n; $v(t)$ contains a potentially different secular frequency ω' and micromotion frequencies $n\Omega \pm \omega'$. Here Ω is the radio frequency and $\Omega \gg \omega, \omega'$. Henceforth we keep only terms with frequencies around Ω and ignore those with frequencies $n\Omega$, $n\Omega \pm \omega$ for $n \geq 2$. Since the integral contains two well separated time scale, we can first integrate over a small time period, resulting a slowly varying

integrand. Quantitatively, consider for example the integral $I_1 = \int_0^\tau \sin\left(a_0(t) + a_1(t)\cos(\Omega t + \phi(t))\right) b_0(t)\, dt$, where $a_0(t)$, $a_1(t)$, $b_0(t)$, $\phi(t)$ are real and vary in a much longer time scale than $1/\Omega$. So during a period of the micromotion, $\cos(\Omega t + \phi)$, $a_0(t)$, $a_1(t)$, $b_0(t)$ and $\phi(t)$ remain approximately constant. We find that

$$\begin{aligned}
I_1 &\approx \int_0^\tau dt \frac{\Omega}{2\pi} \int_t^{t+2\pi/\Omega} dt_1 \sin\left(a_0(t) + a_1(t)\cos(\Omega t_1 + \phi)\right) b_0(t) \\
&= \int_0^\tau dt \frac{1}{2\pi} \int_{-\pi}^{\pi} dt' \sin\left(a_0(t) + a_1(t)\cos(t')\right) b_0(t) \\
&= \mathrm{Im}\left[\int_0^\tau dt \exp\left(i a_0(t)\right) \frac{1}{2\pi} \int_{-\pi}^{\pi} dt' \exp\left(i a_1 \cos(t')\right) b_0(t)\right] \\
&\quad \mathrm{Im}\left[\int_0^\tau dt \exp\left(i a_0(t)\right) J_0(a_1) b_0(t)\right] \\
&= \int_0^\tau dt \sin\left(a_0(t)\right) b_0(t) J_0(a_1(t))
\end{aligned}$$

where J_0 is a Bessel function of the first kind. Looking at the longer time scale, the existence of the fast oscillating term contributes only a modulation factor $J_0(a_1(t))$. Effectively one can think of the laser amplitude being modulated by $J_0(a_1(t))$. Note I_1 takes into account the secular part of $v(t)$ only. We can perform similar time average to get the contribution from the micromotion part of $v(t)$, I_2, which is typically much smaller than I_1

$$\begin{aligned}
I_2 &= \int_0^\tau dt \sin\left(a_0(t) + a_1(t)\cos(\Omega t + \phi)\right) b_1(t) \cos\left(\Omega t + \varphi(t)\right) \\
&\approx \int_0^\tau dt \frac{\Omega}{2\pi} \int_t^{t+2\pi/\Omega} dt_1 \sin\left(a_0(t) + a_1(t)\cos(\Omega t_1 + \phi)\right) b_1(t) \cos\left(\Omega t_1 + \varphi\right) \\
&= \int_0^\tau dt \cos\left(a_0(t)\right) \cos(\varphi - \phi) J_1(a_1(t))
\end{aligned}$$

Similar to the case of I_1, here micromotion gives rise to a slowly varying modulation factor $\cos(\varphi - \phi)J_1(a_1(t))$. In addition the phase of the original integrand is also shifted, $\sin(a_0(t)) \to \cos(a_0(t))$.

These approximate treatments reveal the fact that micromotion merely modulate the laser amplitude seen by the ions by a slowly varying factor, typically around the secular frequency. Therefore the previous quantum gate formalism [10, 11] only requires minor modification to work in the case with significant micromotion. We now quantitively demonstrate a two-qubit phase gate. We consider two Berrylium ions with $9u$ where u is the atomic mass unit. The r.f. trap frequency is $\Omega_T = 2\pi \times 240$ MHz; the characteristic electrode size is $d_0 = 200$ μm; AC/DC voltages, V_0/U_0 are 300V and 21V respectively. The resulting secular trap frequencies are $\omega_{cm} = 2\pi \times 0.965$MHz , $\omega_r = 2\pi \times 3.62$MHz along the z-axis, and $\omega_x = \omega_y = 2\pi \times 20.8$MHz along x- and y-axis. Both motional degrees of freedom are assumed to have a temparture $k_B T = 10\hbar\omega_{\mathrm{cm}}$. The effective laser wave vector is chosen to be $\Delta k = 8\mu\mathrm{m}^{-1}$ so that the quantum motion is within the Lamb-Dicke regime, with $\eta_{\mathrm{cm}} \approx 0.12$ and $\eta_{\mathrm{r}} \approx 0.061$. However the micromotion amplitude $\Delta\bar{u}_r$ is large compared to the laser wavelength, with the Lamb-Dicke parameter $\Delta k \cdot \Delta\bar{u}_r \approx 15.8$. In principle for any chosen laser detuning, there are certain time points at which the motional displacements for both modes $\alpha_{\mathrm{cm/r}}$ are zero (or approximately zero), which means that spin and motion are disentangled. Different laser Rabi frequency would induce different motional amplitudes in the phase space but does not affect motional frequencies. A mode with frequency ω_k driven by a laser with detuning μ will have frequency components $|\mu \pm \omega_k|$, corresponding to period $T_k^{\pm} = 2\pi/|\mu - \omega_k|$. With a single segment laser pulse with constant Rabi frequency (Mølmer-Sørensen gate), at the common multiple of all the $T_k^{\pm}$, all the modes are disentangled with the spin. To get the desired phase flip gate one then chooses the Rabi frequency so that the accumulated spin dependent phase is $\pi/4$. We show the gate fidelities as a function of gate time for $\mu = 0.95\omega_{\mathrm{cm}}$ in Fig. 4.2.2. The center of mass mode is excited much more strongy than the relative mode. The (approximate) least

common multiples of all the periods involved happens to be around $20T_z = 20 \times 2\pi/\omega_{cm}$ for this case. We compared the cases with and without micromotion, and the results obtained by applying the parameters calculated for the case without micromotion to that with the micromotion. We notice that ignoring micromotion in the gate design would cause the fidelity to be rather low. While following our treatment we obtained results very similar to the case where micromotion is absent. For a general value of detuning, segmented pulses are usually needed to close all the motional trajectories. In the case without micromotion, the two ions can experience an identical laser force, i.e. $\chi_1(t) = \chi_2(t) = \chi(t)$ and there are N complex valued motional integrals of the form $\int_0^\tau \chi(t)u^k(t)\,dt$ to be set to 0. In the presence of micromotion $\chi_1(t) \neq \chi_2(t)$ as we mentioned earlier and there are $2N$ such complex valued integrals. Considering also requirement that the total phase be $\pi/4$ we will need $4N+1$ degrees of freedom to have a perfect phase gate, although in practice a pulse with 5 or 11 segments may suffice. Here we show the results with 9-segment pulses for an arbitrarily chosen $\mu = 1.4\omega_{cm}$ and a series of different gate times τ. In theory the optimal fidelities are 1. We compare the Rabi frequencies required by the case with/without micromotion, in Fig. 4.2.3. Since micromotion causes a reduction of the effective Rabi frequency, typically we need to apply a laser with Rabi frequency 5 times larger to compensate that.

4.3 Extension to 2D Ion Crystals

The techniques demonstrated above can also be extended to the many-ion case, e.g. a two dimensional planer ion crystal in a Paul trap. First we adopt the static harmonic trap approximation and solve for the equilibrium positions of all the ions in the crystal. Then we expand the Coulomb potential up to second order for each ion, and find all the normal modes of motion. It is important to note that the normal mode structure is determined by the equilibrium positions only, and the

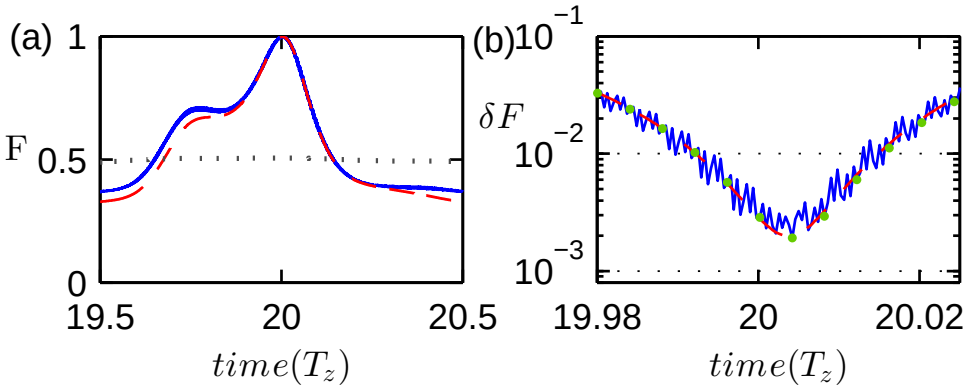

Figure 4.2.2: (a) The fidelity of a two-ion conditional phase flip gate as a function of gate time, where the units of time is the period of the center of mass motion along z-direction $T_z = 2\pi/\omega_{cm}$. The detuning was chosen to be $\mu = 0.95\omega_{\rm cm}$. Blue solid line indicates the optimal results with micromotion taken into account; red dashed line is the result for a genuine static harmonic trap without micromotion; gray dotted line is obtained by applying the optimal solution for a static harmonic trap to the case with micromotion, which results in poor performance. (b) The infidelity (1-fidelity) near the optimal evolution time, eseentially a zoom-in of panel (a) near $t = 20T_z$. Green dots in (b) show the time points that are an integral multiple of the micromotion period. Other parameters used are: temperature of both motional degrees of freedom $k_BT = 10\hbar\omega_{\rm cm}$; effective laser wave vector $\Delta k = 8\mu{\rm m}^{-1}$ so $\eta_{\rm cm} \approx 0.12$ and $\eta_{\rm r} \approx 0.061$.

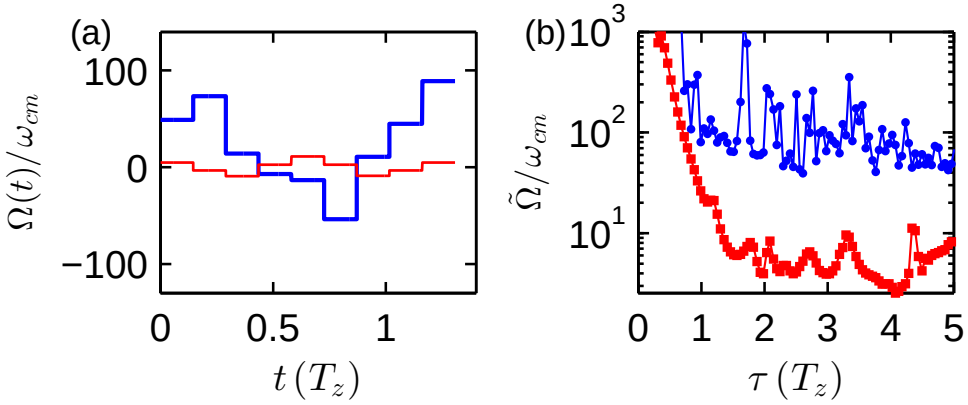

Figure 4.2.3: (a) The waveform of the optimal segmented pulse calculated for the gate with duration $\tau = 1.31T_z$. The thick blue (thin red) line correspondes to the case with (without) micromotion. (b) The maximal Rabi frequency $\tilde{\Omega} \equiv \max_t |\Omega(t)|$ as a function of the gate time τ. The upper blue (lower red) curve corresponds to the case with (without) micromotion.

introduction of a time dependent single-body potential does not change it. Therefore we can now introduce the r.f. potential to the equations of motion for each normal mode as we have done in the two-ion case and get the micromotion corrected equilibrium positions. These two steps need to be done in a self-consistent manner to find out the true equilibrium positions. Then we can calculate the motional integrals and accumulated phases and go through the segmented pulse optimization procedure to obtain high fidelity gates.

4.4 Chapter Summary

In summary, in this chapter we solved the quantum mechanical motion of ions inside a r.f. trap and demonstrated that the original conditional phase flip gate with optimized segmented pulse can be extended to the case with significant ion micromotion. Our formalism applies to ion crystals with a general 1D or 2D structure. We believe this work will open up new possibilities in designing a new scalable trapped ion quantum computer architecture.

CHAPTER V

Efficient Spin Squeezing with Optimized Pulse Sequences

5.1 Introduction

Spin squeezed states are a class of entangled states of spins that have practical applications to precision measurements. In recent years spin squeezing with one-axis twisting (OAT) has been demonstrated experimentally with spinor BECs with more than 10^3 atoms. Although the noise is below the standard quantum limit, the OAT scheme cannot reduce the noise down to the ultimate Heisenberg limit. Here we propose an experimentally feasible scheme based on optimized quantum control to greatly enhance the performance of OAT to approach the Heisenberg limit, requiring only an OAT Hamiltonian and the use of several coherent driving pulses. The scheme is robust against technical noise and can be readily implemented for spinor BECs or trapped ions with current technology.

Spin squeezed states [91] have attracted a lot of interest due to both its role in the fundamental study of many-particle entanglement and its practical application to precision measurements with Ram-

sey interferometers [92–97]. In recent years, much progress has been made on the experimental squeezing of a large number ($10^3 \sim 10^6$) of ultracold atoms [98–102]. Many of these experiments follow the so-called one-axis twisting (OAT) scheme, which is known to reduce the noise/signal ratio from the classical case by a amount that scales as $N^{-2/3}$with the particle number N [91]. This reduction is not optimal yet and still above the so-called Heisenberg limit which scales as N^{-1}. There have been several theoretical proposals to enhance the OAT [103, 104]. For example, one of the approaches [103] involves inducing a better squeezing Hamiltonian, the so called two-axis twisting (TAT) Hamiltonian, with Raman assisted coupling for trapped spinor BECs. This is a hardware level engineering, requiring modification of a particular experimental setup and does not apply to other physical systems. Another approach [104] employs a digital quantum simulation technique to convert an OAT Hamiltonian to an effective TAT Hamiltonian by stroboscopically applying a large number of pulses. This software level solution is universal but sensitive to the accumulation of control errors. None of these proposals have been experimentally tested yet due to various difficulties.

Inspired by the idea of optimized quantum control, we propose an experimentally feasible scheme to greatly improve the performance of OAT, requiring only two or three additional coherent driving pulses to carry out collective spin rotations, which is a routine technique with the current technology. The scheme is shown to be robust to noise and imperfection in control pulses. Using this scheme, it is possible to generate more spin squeezing and detect a significantly larger entanglement depth for the many-particle atomic ensemble [94]. This new scheme enhances the OAT squeezing on the software level and therefore can be applied to any physical system that is endowed with these operations. The idea of optimized squeezing may also be easily transferred to cases where the interaction term deviates from the OAT Hamiltonian.

5.2 Basic Idea

We consider the general scenario of one-axis twisting independent of the underlying physical system with the Hamiltonian $H = \chi S_z^2$ ($S_z = \sum_i^N s_z^i$) (setting $\hbar = 1$). The system starts from a collective spin coherent state polarized along x-axis. As time goes on the initially homogenous spin fluctuation gets distorted and redistributed among different directions and the direction along which spin fluctuation gets suppressed gradually changes over time. The squeezing is measured by the parameter ξ^2, defined as $\xi^2 = N\left\langle S_{\vec{n}}^2 \right\rangle / |\langle S_x \rangle|^2$, where $\vec{n}$ is the direction along which spin fluctuation is minimized. The decreasing rate of ξ^2 slows down with time, and after the optimal squeezing point, ξ^2 increases again. Aside from the initial state, which is rotationally symmetric about x-axis, all the subsequent states breaks this symmetry and picks out a special direction, i.e. the direction along which fluctuation is minimized. It is well known that the two-axis twisting (TAT) Hamiltonian $H_2 = \chi_2 \left(S_x^2 - S_y^2\right)$ can produce better squeezing [91], which, after doing the Trotter decomposition with an infinitesimal time interval, could be seen as switching the squeezing axis back and forth very fast between two orthogonal directions [104]. To avoid the noise accumulation from a large number of switching pulses inherent in the Trotter expansion scheme, we take an alternative approach based on optimization of a few control pulses to maximize the squeezing of the final state. We consider an n-step squeezing protocol (where n is typically 2 or 3 for a practical scheme) defined as follows: at step j ($j = 1, 2, ..., n$), we first apply an instantaneous collective spin rotation around x-axis, $U(\alpha_i) = exp(-iS_x\alpha_i)$, and then let the state evolve under the OAT Hamiltonian $H = \chi S_z^2$ for a duration T_i. Effectively, we squeeze the state along a different axis lying in the $y-z$ plane in each step, so the effective evolution operator can be written as

$$U(\theta_i, T_i) = \prod_{i=n}^{1} exp(-i\chi S_{\theta_i}^2 T_i), \tag{5.2.1}$$

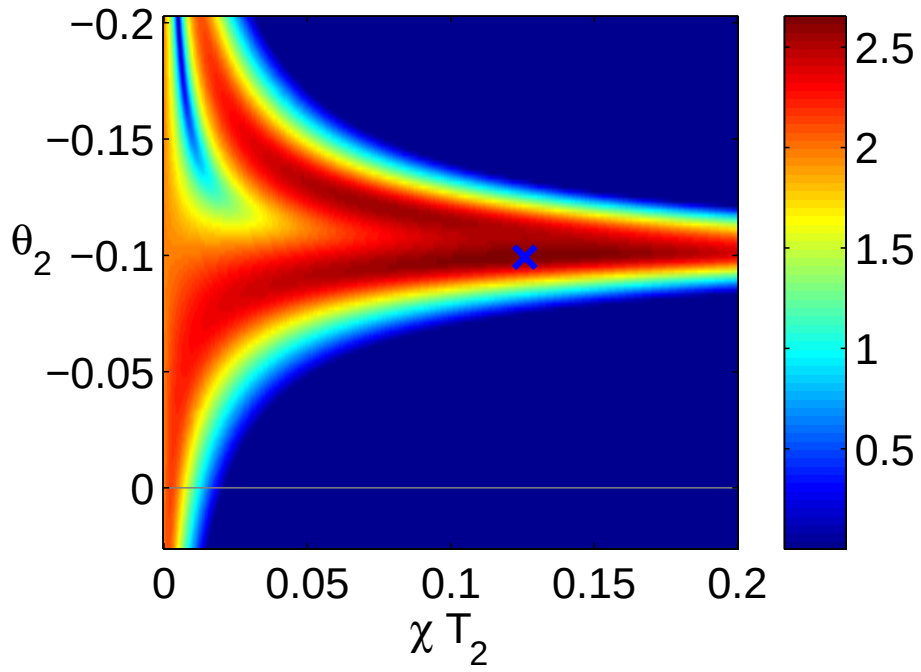

Figure 5.2.1: The squeezing $-log(\xi^2)$ as a function of the control parameters θ_2 and T_2 for a typical value of T_1, calculated with N=2000 spin-1/2 particles. See Eq. (5.2.1) and text for definition of θ_i and T_i. The cross symbol marks the point of optimal squeezing. The horizontal line $\theta_2 = 0$ corresponds to the case of the OAT scheme.

where $S_{\theta_j} \equiv cos\theta_j S_z + sin\theta_j S_y$ and the factors are arranged from right to left with increase of j. This evolution operator coincides with that of a quantum kicked-top model with n kicks. Since the initial state is assumed to be polarized along x-direction, which is symmetric around x-axis, θ_1 is irrelevant and can be chosen to be 0 (so no control pulse is needed for step 1). Therefore, for an n-step squeezing protocol, there are $(2n-1)$ tunable parameters: T_i and θ_i (excluding θ_1). The final squeezing parameter is thus a multi-variable function $\xi^2(T_i, \theta_i)$. Note that as n becomes very large, our protocol includes the proposed sequence in [104] as a special case and so in principle our protocol can approach the Heisenberg limit as n grows. Our purpose is to find the best available squeezing $\xi^2(T_i, \theta_i)$ with a minimum number n of the time steps.

5.3 Numerical Results

In the case of $n = 2$ or 3, the landscape of $\xi^2(T_i, \theta_i)$ in the parameter space is quite simple and well behaved. Take the $n = 2$ case as an example. For a typical value of T_1 smaller than the optimal OAT squeezing time, $-log(\xi^2)$ as a function of θ_2 and T_2 is shown in Fig. 5.2.1. The optimal squeezing point marked by the cross lies way off the OAT trajectory, the horizontal line with $\theta_2 = 0$. For the $n = 3$ case, with θ_2 and T_2 fixed near the optimal values of the $n = 2$ case, $-log(\xi^2)$ as a function of θ_3 and T_3 shows a similar landscape. These solutions already exceed that of the OAT scheme by a large margin. The results indicate that the optimization technique with n as small as 2 or 3 suffices to significantly improve over the OAT scheme.

Next, we investigate performance of the optimized squeezing scheme, focusing on the scaling of the squeezing $\xi^2(T_i, \theta_i)$ as a function of the total particle number N. For a given set of parameters, we can numerically calculate the evolution operator in Eq. (5.2.1) by exactly diagonalizing the effective Hamiltonians $S^2_{\theta_i}$ and then obtain the squeezing parameter ξ^2. To account for the fact that in reality the coherent spin rotations cannot be generated instantaneously, in the numerical simulation we actually keep the OAT Hamiltonian on all the time, even during the spin rotations. However we do assume the effective magnetic field B effecting the spin rotation to be much stronger than the squeezing Hamiltonian, $B \gg N\chi$, as is the case in experiments. We randomly sample from the parameter space for a large number of times, use these random samples as initial guesses to start unconstrained local optimization of the squeezing parameter, and pick the best one as our solution. Repeating this procedure for every system size N is extremely resource intensive especially when N gets as large as 10^5. Taking advantage of the fact that adding several more to 10^3 particles should not change the solution much, we can feed the previously found non-local optimal solution as an initial guess to the local optimizer of a larger system and obtain a near

optimal solution quickly. In this way we managed to obtain (near) optimal solutions for systems all the way up to $N = 10^5$ particles, with only a cost of classical computing time on the order of tens of hours on a typical multi-core computer. As shown in Fig. 5.3.1, with $n = 2$, the squeezing parameter ξ^2 gets reduced by a significant amount already compared with the OAT scheme, and with $n = 3$, ξ^2 decreases further. The scaling of ξ^2 with the number of particles shows a clear power law $\xi^2 \sim 1/N^\beta$. A simple OAT scheme gives $\beta = 2/3$ and the TAT scheme gives $\beta = 1$ [91]. The Heisenberg limit of noise gives a bound $\beta \leq 1$ for the scaling, and this bound is saturated by the TAT scheme. Remarkably we observe that the optimized $n = 2, 3$ protocols can give $\beta = 0.92$ and 0.98, respectively, very close to the ultimate Heisenberg limit. Moreover, the $n = 3$ optimized scheme has a smaller multiplicative constant compared with the TAT scheme, so in the realistic range of particle number $N \lesssim 10^6$, it actually outperforms the TAT scheme. This shows that a moderate alternation of the OAT scheme through optimization can significantly increase the spin squeezing.

We have demonstrated a significant improvement over the conventional OAT by applying very few optimized control pulses. A cost of the proposed scheme is that it takes longer evolution time to achieve the optimal squeezing. A typical evolution of ξ^2 with time t is shown in Fig. 5.3. We notice that in general the $(i+1)$-th squeezing step takes longer time than the i-th step. Since the time cost in the first step is on the order of the optimal OAT duration, the overall duration of the new protocol is usually longer than that of the OAT scheme. An excessively long duration would be an obstacle in systems with short coherence time. The two relevant time scales here are the coherence time τ and the inverse of interaction strength $1/\chi$. The time cost of the new scheme is around $0.01/\chi \sim 0.1/\chi$. If $\tau \gtrsim 0.1/\chi$ the new scheme can be implemented without compromise. On the other hand, if that is not the case, decoherence effect would play a role and our unconstrained optimization no longer yields the best result. However, we can work around this problem by

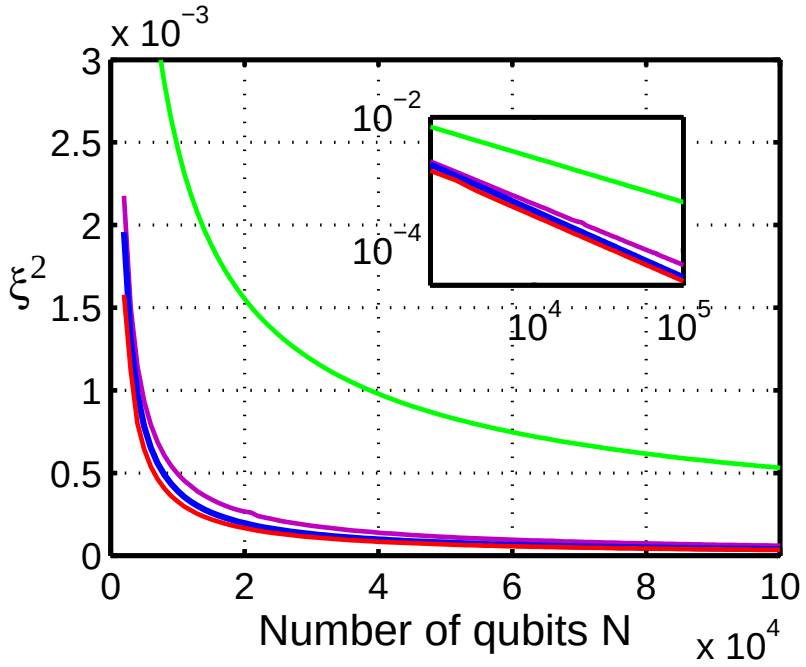

Figure 5.3.1: Scaling of the squeezing parameter ξ^2 with the number of qubits. Curves from top to bottom are for one-axis twisting (OAT), two-step optimized squeezing, two-axis twisting (TAT) and three-step optimized squeezing. Inset shows the same curves in log-log scale.

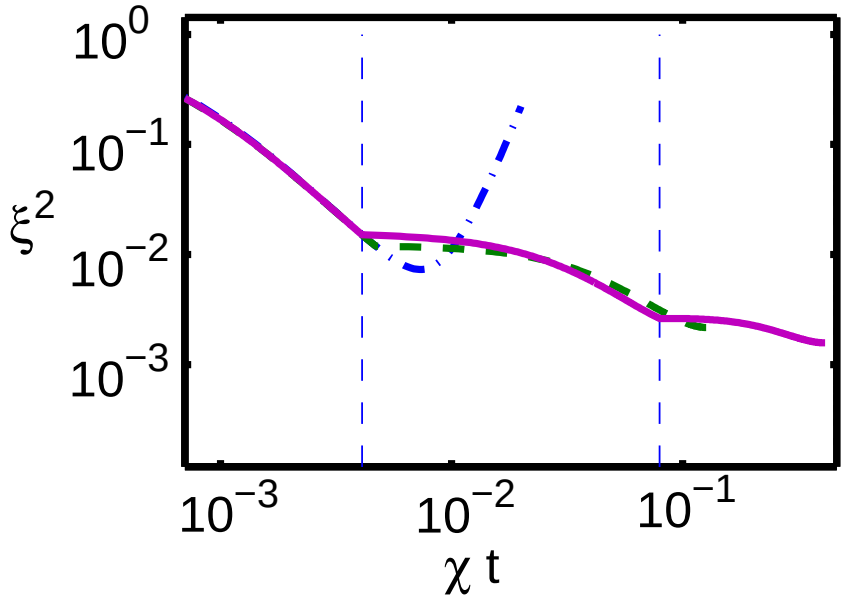

Figure 5.3.2: Evolution of the squeezing parameter ξ^2 with time, calculated with N=2000 spin-1/2 particles. The dash-dot line is for one-axis twisting (OAT), the dash line for the two-step optimized squeezing scheme, and the solid line for the three-step optimized squeezing.

performing an optimization with the total duration added as a cost function and get a compromised optimal pulse sequence. By tuning the weight of the cost function we could obtain a continuous series of compromised optimal solutions as shown in Fig. 5.3.3. These solutions of two-step and three-step schemes form two line segments, continuously connecting the optimal OAT squeezing protocol to that of the unconstrained optima, offering a trade off between the protocol duration and the squeezing magnitude. For each real experimental setup, one could correspondingly pick up the best point in accordance with the coherence time of the system. How much one can gain over the OAT scheme depends on how long the coherence time can reach.

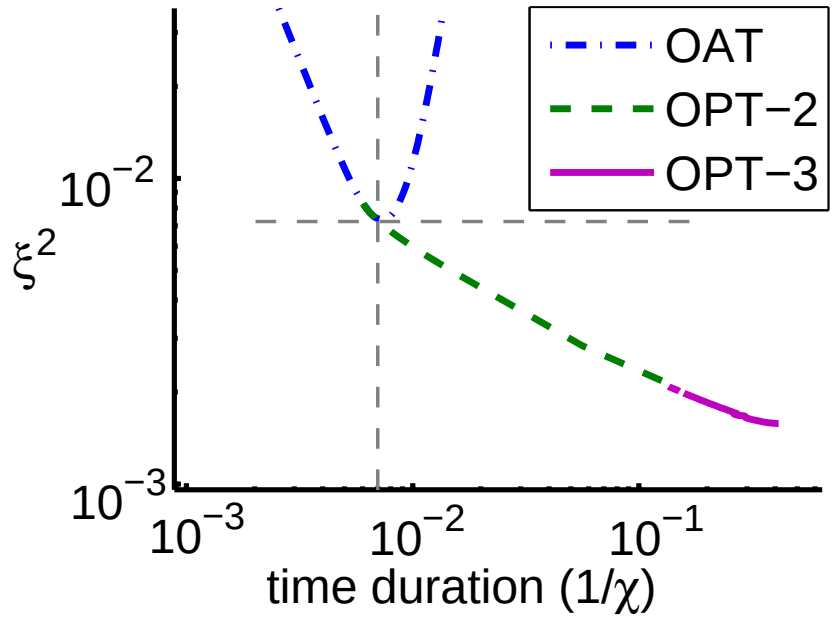

Figure 5.3.3: Constrained optimization of ξ^2 with the total time duration as a cost function. We take $1/\chi$ as the time unit. Achievable squeezing ξ^2 as a function of the total duration is shown, together with one-axis twisting (OAT), calculated with $N = 2000$ spin-$1/2$ particles. OPT-2 (3) stands for optimized squeezing sequence with $n = 2(3)$ segments. Horizontal and vertical dashed lines are guides to the eye.

5.4 Noise Resistance and Physical Realization

Next we test noise resistance of the proposed scheme. There are only $3(5)$ control parameters in the $n = 2(3)$ scheme, making the accumulation of control noise negligible. We have done numerical simulation of our scheme adding random pulse area/timing noise and confirmed the robustness of the squeezing parameter ξ^2 as shown in Fig. 5.4.1. This contrasts to the proposals [104, 105] requiring a large number of coherent rotation pulses where control errors accumulate and significantly degrade the performance. Thus our proposed scheme offers a useful alternative to the previous works. Another practical issue related to control noise is the uncertainty in number of particles in a real experiment. Our pulse scheme depends on the number of particles N while in experiments such as ultracold gas we do not typically know the number N exactly. Fortunately we notice that the control parameters vary slowly with N, e.g. in going from N=1900 to N=2100, the control parameters only vary by 1%-5%. So a $\pm$5% uncertainty in N at N=2000 is equivalent to an extra noise below 5% in the control parameters, to which ξ^2 is not so sensitive as we have shown in Fig. 5.4.1.

Finally we discuss possible physical realizations of the scheme proposed here. The scheme only requires two ingredients, the nonlinear collective spin interaction S_z^2 and the ability to rotate the collective spin around an orthogonal axis, say x. Several experimental systems meet these requirements, e.g., trapped ions and spinor BECs. In trapped ion systems, depending on the ion species, one can use bichromatic lasers or two pairs of Raman laser beams (the Mølmer-Sørensen scheme) to induce the S_z^2 or S_x^2 type of interaction. The strength of this interaction χ can reach kHz scale, giving $1/\chi \sim ms$. The coherence time usually exceeds $1/\chi$ and our scheme can apply without compromise. Collective spin rotation can be simply done by shining laser on all the ions driving the corresponding single-qubit $\sigma_{x/y}$ or rotation. The rotation pulses have durations much shorter

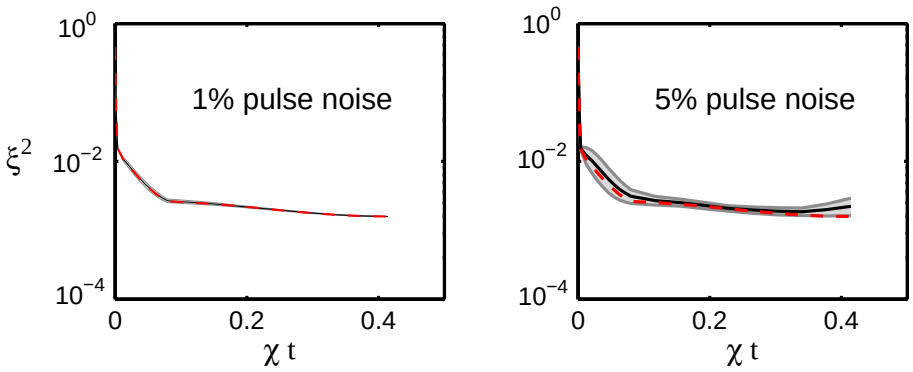

Figure 5.4.1: Optimized squeezing in the presence of control noise. We use the three-step optimization scheme as an example and assume all the five control parameters in this scheme have the same magnitude of relative errors as specified in this figure. The dash line is for the ideal case with no error in the control parameters, the solid line denotes the average of many random trajectories (50 random trials) and the shaded area marks the range of those trajectories. In the left panel, the shaded region is too small to be distinguished from the ideal case.

than $1/\chi$. While linear Paul traps [46, 73] can now coherently control only about a dozen of ions, too few for the purpose of spin squeezing, planar Penning traps can manipulate more than 200 ions [106]. For the purpose of precision measurement, 200 ions may seem less impressive than 10^5 particles, but we show that using our scheme we can create genuine multi-particle entangled states with a significantly larger entanglement depth. The entanglement depth, defined in [94], is a way to measure how many particles within the whole sample have been prepared in a genuine entangled state. Our result is shown in Fig. 5.4.2. In this figure, a point lying below the optimal squeezing curve of n particles correspond to a state that contains genuine n-particle entanglement. Our scheme produces states that lie below the OAT states in a large range of $\langle S_x \rangle$ values, which means that experimentally one can achieve a significantly larger entanglement depth by this optimization technique.

Another class of physical system is a spinor Bose-Einstein condensate of atoms with two chosen internal states mimicking spin-1/2 particles [99, 100]. The desired S_z^2 interaction is induced by

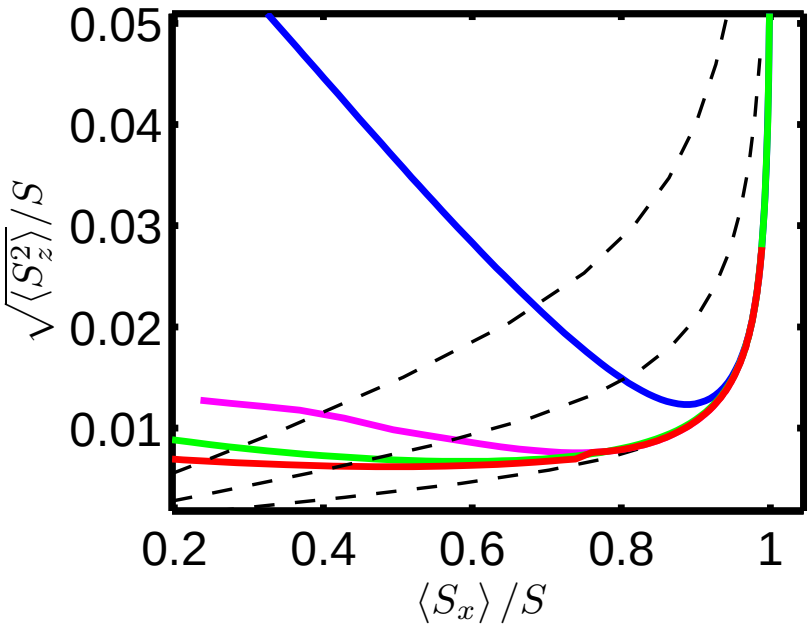

Figure 5.4.2: The entanglement depth achievable with different approaches for 200 spin-$1/2$ particles. The solid lines from top to bottom correspond respectively to the OAT scheme, the two-step optimized squeezing, the TAT, and the three-step optimized squeezing. The dashed lines from top to bottom correspond to the optimal squeezing for 50, 100, and 200 particles respectively. Lying below the curve of optimal squeezing for n particles is a certificate of genuine n-particle entanglement.

spin-dependent s-wave scattering as proposed in [95]. Coherent laser pulses illuminating the whole condensate can implement spin rotations similar to the trapped ion case. However, the strength of S_z^2 interaction is much smaller compared with the trapped ion case, $\chi = 0.3 \sim 0.5$ Hz as reported in [99, 100]. The coherence time for the spinor BEC is also shorter. Hence we typically need to apply the compromised scheme, using the actual coherence time and interaction strength of the system as input parameters.

5.5 Chapter Summary

In summary, we have proposed a new method based on optimization to significantly enhance spin squeezing using the one axis twisting Hamiltonian. To achieve significant improvement in spin squeezing, we need to apply only one or two global rotation pulses at an appropriate evolution time and with optimized rotation angles. Using two pulses, the final squeezing is very close to the Heisenberg limit already. Comparing to the previous proposal [104], apart from requiring a simpler pulse sequence, the major advantage of this new method is the robustness to control noise due to the very small number of coherent pulses used. A scheme involving a large number of pulses usually suffers the accumulation and amplification of control errors in each pulse and tolerates only a very small technical noise. The major drawback that limits the applicability of our proposal is the longer evolution time compared to [104], although still being faster than adiabatic preparation. We believe this new proposal can be readily applied in certain experimental systems where coherence time is not the bottleneck, without significant modification of the setup.

It is an interesting future direction to extend our optimization technique to generate continuous wave forms, like that reported in [107] where a similar Hamiltonian was considered and optimal control techniques were used to obtain a continuous wave form of effective magnetic field for the

squeezing of a collection of F=3 spins.

CHAPTER VI

State Detection Error Correction with Statistical Methods

6.1 Introduction

The prospect of quantum computation and quantum communication [49] strongly stimulates interest in engineering of various non-classical states with multi-partite entanglement as a resource for quantum information. Due to the volatile and elusive nature of entanglement, verifying it alone is not a trivial problem. Many approaches to this problem have been proposed (see [108] for a review). Those detection schemes, e.g. entanglement witnesses, generally involve an inequality of certain observables, the violation of which indicates entanglement. However there is an issue with these schemes previously unconsidered, associated with the imperfect efficiency of the detectors used in real experiments, which causes detection error and potentially false estimation of the state.

In this chapter, we describe a simple method to correct the detection error caused by the detectors, which is practically a significant obstacle to the observation of multipartite entanglement in quantum state engineering [46, 109, 110]. We show here that this type of error can be corrected at

any magnitude as long as the error magnitude has been calibrated (for instance, through prior test experiments). The detection error distorts the experimental data by a transformation that depends on the magnitudes of various error possibilities. When the relevant error magnitudes have been calibrated for the detectors by the prior test experiments, the form of the distortion transformation induced by the detection error is known, and then we can find a way to invert this transformation to reconstruct the original signal. In this way, we can use imperfect detectors to simulate perfect detectors as long as their imperfection has been calibrated. The proposed method is straightforward for experimental implementation as it is based on data processing and does not increase the complexity of the setup. To correct the detection error, we only require to repeat the same experiments by some additional rounds to have small statistical error for the inverse transformation. To illustrate its applications, the method is used to significantly improve the detection of multi-qubit entanglement and spin squeezing. In many cases, the signal of multipartite entanglement only becomes visible after the proposed correction of the detection error, in particular when the number of qubits is large.

6.2 Mathematical Formulation

Any measurements in quantum information can be reduced to population measurements in certain bases (including possibly several complementary bases). If we want to measure properties associated with a state ρ (generally mixed) of n qubits, for each chosen measurement basis, there are 2^n possible measurement outcomes. By performing measurements we determine the probability f_i associated with each outcome i ($i = 1, 2, \cdots, 2^n$). For instance, if we repeat the same experiment N times and get the ith outcome N_i times, we estimate the probability f_i by $f_i = N_i/N$ and its standard deviation (the error bar) by $\Delta f_i = \sqrt{f_i(1-f_i)/N}$ using the binomial distribution. If the detectors

are perfect, the measured probabilities f_i just give the distribution $g_i \equiv \langle i|\rho|i\rangle$ of the state ρ in the measurement basis $\{|i\rangle\}$. In reality, however, the detectors always have errors, which distort the distribution g_i, potentially making the measured distribution f_i significantly different from g_i. The purpose of this chapter is to show how to reconstruct the real distribution g_i from the measured distorted probabilities f_i.

6.2.1 Individual Qubit Addressing Case

We first consider the case where the measurements have individual addressing, and each qubit is measured by an independent detector. For detection on a qubit, the most general error model is characterized by a 2×2 matrix

$$D = \begin{bmatrix} 1-p_0 & p_1 \\ p_0 & 1-p_1 \end{bmatrix}, \tag{6.2.1}$$

where p_0 (p_1) denotes respectively the error probability that the detector gives outcome 1 (0) for the input signal of 0 (1). For simplicity of notation, we assume the error matrix D has the same form for detection of each qubit (it is straightforward to generalize the formalism to the case where the error rates p_0 and p_1 in the D matrix are qubit-dependent). Furthermore, we assume p_0 and p_1 have been well calibrated by a prior test experiment. For instance, we may input a known state to the detector and can calibrate p_0 and p_1 easily from the measurement data.

For n qubits, the error model for the detection is then characterized by a $2^n \times 2^n$ matrix $M = \left[M_{ji}\right]$, with the element M_{ji} corresponding to the probability of recording the outcome j with the input signal i. Assume the detection error rates on different qubits are independent of each other and the binary string i has n_0 zeros and $n_1 = n - n_0$ ones. If we need α flips from 0 to 1 and β flips from 1

to 0 to change the string from i to j, the matrix element M_{ji} is given by

$$M_{ji} = (1-p_0)^{n_0-\alpha}\,(1-p_0)^{n_1-\beta}\,p_0^{\alpha}p_1^{\beta}. \tag{6.2.2}$$

The measured probabilities f_j are connected with the real distribution g_i through the distortion transformation $f_j = \sum_{i=1}^{2^n} M_{ji}g_i$.To reconstruct the real signal g_i from the measured distribution f_j, in principle we only need to invert the matrix M. However, as M is a huge $2^n \times 2^n$ matrix, it is not clear how to invert this matrix (it is even a question whether the inverse exists).

Our key observation is that the matrix M, with the elements given by Eq. (6.2.2), has a simple tensor product structure. It is straightforward to show by mathematical induction that

$$M = \bigotimes_{k=1}^{n} D_k, \tag{6.2.3}$$

where all the D_k are identical and given by D in Eq. (6.2.1). Therefore, the inverse can be easily done in an analytic form with

$$M^{-1} = \bigotimes_{k=1}^{n} D_k^{-1} = \bigotimes_{k=1}^{n} \begin{bmatrix} 1-p_0' & p_1' \\ p_0' & 1-p_1' \end{bmatrix}_i, \tag{6.2.4}$$

where the parameters p_0' and p_1' are given by

$$\begin{aligned} p_0' &= p_0/(p_0+p_1-1), \\ p_1' &= p_1/(p_0+p_1-1). \end{aligned} \tag{6.2.5}$$

Note that with the substitution in Eq. (6.2.5), M^{-1} and M have the same form except that p_0' and

p_1' can not be interpreted as error rates any more since in general they are not in the range $[0,1]$. The formula also shows that the inverse transformation M^{-1} always exists except for the special case with $p_0 + p_1 = 1$.

6.2.2 Collecive Measurement Case

In some experimental systems we do not have the ability to resolve individual qubits. Instead, we perform collective measurements on n qubits by detecting how many qubits (denoted by j, $j = 0, 1, \cdots, n$) are in the state $|1\rangle$ in a chosen detection basis (this is equivalent to measurement of the collective spin operator along a certain direction). In this case, the detection only has $n+1$ outcomes for an n-qubit system. For collective measurements on n qubits, the detection error matrix is represented by an $(n+1)\times(n+1)$ matrix $L = \left[L_{ij}\right]$. The matrix element L_{ij} corresponds to the probability to register outcome i when j qubits are in the $|1\rangle$ state. If the detection error matrix for an individual qubit is still given by D in Eq. (6.2.1), we can directly calculate L_{ij} from D: from signal j to i, if n_{10} qubits flip from 0 to 1 and n_{01} qubits flip from 1 to 0, with the constraints $0 \le n_{01} \le j$, $0 \le n_{10} \le n-j$ and $n_{01} - n_{10} = j - i$, L_{ij} is given by

$$\begin{aligned} L_{ij} &= \sum_{\substack{0\le n_{01}\le j,\\ 0\le n_{10}\le n-j,\\ n_{01}-n_{10}=j-i}} B(j,p_1,n_{01})B(n-j,p_0,n_{10}) \\ &= \sum_{q=\max\{0,i+j-n\}}^{\min\{i,j\}} B(j,1-p_1,q)B(n-j,p_0,i-q), \end{aligned} \tag{6.2.6}$$

where $B(n,p,k) \equiv \binom{n}{k} p^k (1-p)^{n-k}$ and we have let $q = i - n_{10}$, and hence q satisfies the constraint $\max\{0, i+j-n\} \le q \le \min\{i,j\}$. As the dimension of the L matrix depends linearly on the qubit

number n, it is typically not difficult to numerically calculate its inverse matrix L^{-1} if n is not very large. As shown in Appendix E, there is also a simple analytic formula for $L^{-1} = \left[L_{ij}^{-1}\right]$: if we denote the dependence of L_{ij} in Eq. (6.2.6) on p_0, p_1 as $L_{ij} = L_{ij}(p_0, p_1)$, we have

$$L_{ij}^{-1} = L_{ij}\left(p_0', p_1'\right) \tag{6.2.7}$$

where p_0', p_1' are given by the simple substitution in Eq. (6.2.5). With the inverse matrix L^{-1}, the real signal g_i can be similarly reconstructed from the measured data f_j as $g_i = \sum_j L_{ij}^{-1} f_j$.

The above formulation can be extended straightforwardly to qudit (d-dimensional) systems where the individual detection error matrix D in Eq. (6.2.1) is replaced by a $d \times d$ matrix. For independent detection of n-qudits, the overall error matrix M still has the tensor-product structure as shown by Eq. (6.2.3), which allows for an easy calculation of M^{-1} from D^{-1}.

6.2.3 Cost of Error Correction

With the inverse error matrix M^{-1}, it is straightforward to reconstruct the true distribution g_i from the measured data f_i. The price we need to pay is that compared with $\Delta f_i = \sqrt{f_i(1-f_i)/N}$, there is an increase of the standard deviation (error bar) Δg_i in our estimate of g_i by the formula $g_i = \sum_{j=1}^{2^n} M_{ij}^{-1} f_j$. With some tedious but straightforward calculation, we find

$$\Delta g_i = \sqrt{[\sum_j (M_{ij}^{-1})^2 f_j - g_i^2]/N} \tag{6.2.8}$$

As $M^{-1} = \bigotimes_{k=1}^{n} D_k^{-1}$ and D_k^{-1} has matrix element $1 - p_0' \approx e^p > 1$ (when $p_0 \sim p_1 \sim p \ll 1$), M^{-1} has matrix element $\sim e^{np}$ which leads to exponential increase of the error bar Δg_i with the qubit number n. To maintain the same error bar Δg_i, the number of repetitions N of the experiment

eventually needs to increase exponentially with n. For practical applications, this exponential increase of N by the factor e^{np} is typically not a problem for two reasons. First, as the detection error rate p is usually at a few percent level, the exponential factor e^{np} remains moderate even for hundreds of qubits. Second, this exponential increase only applies when we need to measure each element of the distribution g_i. In most of quantum information applications, we only need to measure certain operators which are expressed as tensor products of a constant number of Pauli operators for different qubits. In this case, N does not have the exponential increase as we show now.

Suppose we need to measure an operator $\hat{O}$, which is expressed as $\hat{O} = \otimes_{k=1}^{n} \sigma_k^{\mu_k}$, where $\sigma_k^{\mu_k}$ is a component of the Pauli matrices when $\mu_k = 1,2,3$ or the identity operator when $\mu_k = 0$. The number of the Pauli matrices n_p in the tensor product expansion of $\hat{O}$ is called the support of $\hat{O}$. To measure the operator $\hat{O}$, we choose the measurement basis to be the eigenbasis of $\sigma_k^{\mu_k}$ for the kth qubit. In this measurement basis, $\hat{O}$ is diagonal with the matrix element $\hat{O} = \otimes_{k=1}^{n} \mathrm{diag}\left(\sigma_k^{\mu_k}\right)$, where $\mathrm{diag}\left(\sigma_k^{\mu_k}\right) = [1,1]$ for $\mu_k = 0$ and $\mathrm{diag}\left(\sigma_k^{\mu_k}\right) = [1,-1]$ for $\mu_k = 1,2,3$. Under the distribution g_i, the expectation value of $\hat{O}$ is given by $\left\langle \hat{O} \right\rangle = \sum_i \hat{O}_i g_i = \sum_i \hat{O}_i \sum_j M_{ij}^{-1} f_j = \sum_j (\sum_i \hat{O}_i M_{ij}^{-1}) f_j \equiv \sum_j \hat{O}_j^c f_j$, where $\hat{O}_i$ denotes the diagonal matrix element of $\hat{O}$. Therefore, by defining a corrected operator $\hat{O}^c$, we can get the true expectation value $\left\langle \hat{O} \right\rangle$ directly from the experimental data f_j. Using the relation $M^{-1} = \bigotimes_{k=1}^{n} D_k^{-1}$, $\hat{O}^c$ is expressed as $\hat{O}^c = \bigotimes_{k=1}^{n} \left[\mathrm{diag}(\sigma_k^{\mu_k}) D_k^{-1}\right]$. For $\mu_k = 1,2,3$,

$$\begin{aligned}\mathrm{diag}(\sigma_k^{\mu_k})D_k^{-1} &= \begin{bmatrix} 1 & -1 \end{bmatrix} \begin{bmatrix} 1-p_0' & p_1' \\ p_0' & 1-p_1' \end{bmatrix} \\ &= \begin{bmatrix} (1-2p_0') & -(1-2p_1') \end{bmatrix} \end{aligned} \tag{6.2.9}$$

and for $\mu_k = 0$, $\mathrm{diag}(\sigma_k^{\mu_k})D_k^{-1} = [1,1]$. For simplicity of notation, we take $p_0 = p_1 = p$. In this case, $\mathrm{diag}(\sigma_k^{\mu_k})D_k^{-1} = (1-2p)^{-1}\mathrm{diag}(\sigma_k^{\mu_k})$ for $\mu_k = 1,2,3$, and the corrected operator $\hat{O}^c$ is related with the original operator $\hat{O}$ by a simple scaling transformation $\hat{O}^c = (1-2p)^{-n_p}\hat{O}$. The scaling transformation is independent of the qubit number n, so the error bar of $\langle \hat{O} \rangle$ does not have exponential increase with n when the operator $\hat{O}$ has a constant support n_p.

The scaling transformation also applies to collective operators, but some caution needs to be taken for calculation of their variance. For instance, if we take the collective spin operator $J_z \equiv \sum_{k=1}^{n} \sigma_k^z/2$, it is easy to see that $J_z^c = (1-2p)^{-1} J_z$ as each of the terms of J_z has support $n_p = 1$. However, as $J_z^2 \equiv n/4 + \sum_{k\neq l} \sigma_k^z \sigma_l^z/4$ which has non-uniform support for its superposition terms, one finds that $\left(J_z^2\right)^c = n/4 + (1-2p)^{-2}\left(J_z^2 - n/4\right) = (1-2p)^{-2}\left[J_z^2 - np(1-p)\right]$. With this transformation, we can correct the distortion to the spin squeezing parameter by the detection error. Assume that the mean value of $\langle \mathbf{J} \rangle$ is along the x-direction with $\langle \mathbf{J} \rangle = \langle J_x \rangle$ and the squeezing is along the z-direction. The squeezing parameter is given by $\xi = \sqrt{n\langle J_z^2 \rangle / \langle J_x \rangle^2}$ [93]. Using the transformation for $\left(J_z^2\right)^c$ and J_x^c, we find that

$$\xi^c = \sqrt{n\langle \left(J_z^2\right)^c \rangle / \langle J_x^c \rangle^2} = \sqrt{\xi^2 - \xi_d^2} \tag{6.2.10}$$

where $\xi_d^2 = n^2 p(1-p)(1-2p)^{-2}\langle J_x \rangle^{-2}$ is the contribution to ξ^2 by the detection noise. After correction of the detection error, ξ^c gets significantly smaller compared with ξ in particular when

the qubit number n is large, and thus can be used to verify a much bigger entanglement depth using the criterion in Ref. [94]. From Eq. (6.2.10), we find that the variation $\Delta\xi^c/\Delta\xi = \xi/\xi^c$. As typically $\xi \gg \xi^c$, the error bar for ξ^c after correction of the detection error gets significantly larger, and we need to correspondingly increase the rounds of the experiment N to reduce the statistical error.

6.3 Application Example

To illustrate application of the error correction method here, as an example, we apply it to detection of genuine multi-partite entanglement in graph states. For a graph state $|G_n\rangle$ of n qubits associated with a q-colorable graph G, the genuine n-party entanglement can be detected with the following witness operator [108]

$$W_{G_n} = 3\mathbb{I} - 2\left[\sum_{l=1}^{q}\left(\prod_{k\in Q_l}(S_k+\mathbb{I})/2\right)\right] \tag{6.3.1}$$

where Q_l denotes the set of qubits with the lth color ($l = 1,2,\cdots,q$), $\mathbb{I}$ is the identity operator, and S_k is the stabilizer operator for the kth qubit (which is a tensor product of the Pauli operators σ_k^x for the kth qubit and $\sigma_{k'}^z$ for all it neighbors k' in the graph G). A state ρ has genuine n-qubit entanglement if $tr(\rho W_{G_n}) = \langle W_{G_n}\rangle < 0$. For an ideal graph state, all its stabilizer operators S_k have expectation values $\langle S_k\rangle = 1$. With detection error, the value of $\langle S_k\rangle$ gets significantly degraded. As an example, Fig. 6.3 shows the values of all $\langle S_k\rangle$ for two particular 2-colorable graph states: a 10-qubit GHZ state (GHZ_{10}) and a linear cluster state (LC_{10}). We assume 3% detection error with $p_0 = p_1 = p = 0.03$ for each qubit. With a known magnitude p, the detection error can be easily corrected by a scaling transformation $S_k^c = (1-2p)^{-n_{pk}} S_k$, where n_{pk} is the

support of the corresponding stabilizer operator S_k. Fig. 6.3 shows that after error correction, $\langle S_k^c \rangle$ is almost unity. Its error bar increases a bit after the correction, but is still small. To show the influence on the entanglement detection, we assume the experimentally prepared graph state ρ_{ex} corresponds to the ideal target state ρ_{id} distorted by small depolarization noise independently acting on each qubit, so $\rho_{ex} = \widehat{\$}(\rho_{id})$, where the noise super-operator $\widehat{\$} = \bigotimes_{k=1}^{n} \widehat{\$}_k$ and $\widehat{\$}_k(\rho_{id}) = (1-3p_n/4)\rho_{id} + p_n/4 \sum_{\mu=x,y,z} \sigma_k^{(\mu)} \rho_{id} \sigma_k^{(\mu)}$ [111]. In Fig. 6.3, we show the witness $\langle W_{G_n} \rangle$ as a function of the preparation error rate p_n, both before and after correction of the detection error (with an error rate $p = 3\%$). For both GHZ_{10} and LC_{10} states, without correction of the detection error, we cannot detect any n-qubit entanglement even for a perfectly prepared state with $p_n = 0$. After correction of the detection error, we can confirm genuine n-qubit entanglement as long as the preparation error $p_n \lesssim 5\%$. So, correction of the detection error significantly improves the experimental performance, and the improvement gets more dramatic when the qubit number increases.

6.4 Sensitivity on Detector Calibration

We briefly comment on the sensitivity of our error correction method to calibration of the detection error. In this method, the error magnitude p (or magnitudes p_i, $i = 0, 1, \cdots$, for general cases) is assumed to be known. If we have a relative error e in calibration of the magnitude p, .i.e., $\delta p / p \sim e$, the scaling transformation on the detected operator $\hat{O}$ leads to a relative error in the observed quantity $\delta \langle \hat{O} \rangle / \langle \hat{O} \rangle \sim 2n_p \delta p (1-2p)^{-1} \sim 2n_p pe$. As long as $2n_p p \lesssim 1$, which is typically the case as $p \ll 1$, the relative error actually gets reduced and the method here can tolerate some uncertainty in calibration of the error magnitude p.

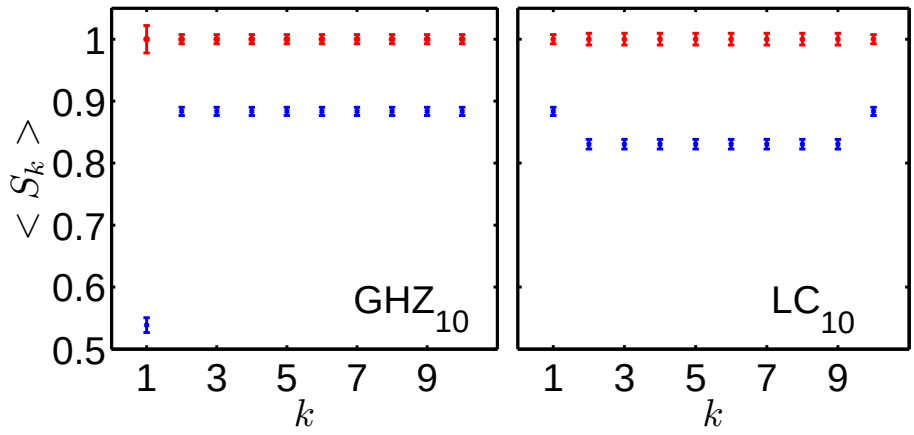

Figure 6.3.1: Values of stabilizers before (lower points) and after (upper points) correction of the detection error (with the error rate $p = 0.03$) for the 10-qubit GHZ state (GHZ_{10}) and the linear cluster state (LC_{10}). Error bars account for the statistical error by assuming $N = 5000$ independent measurements in each detection setting.

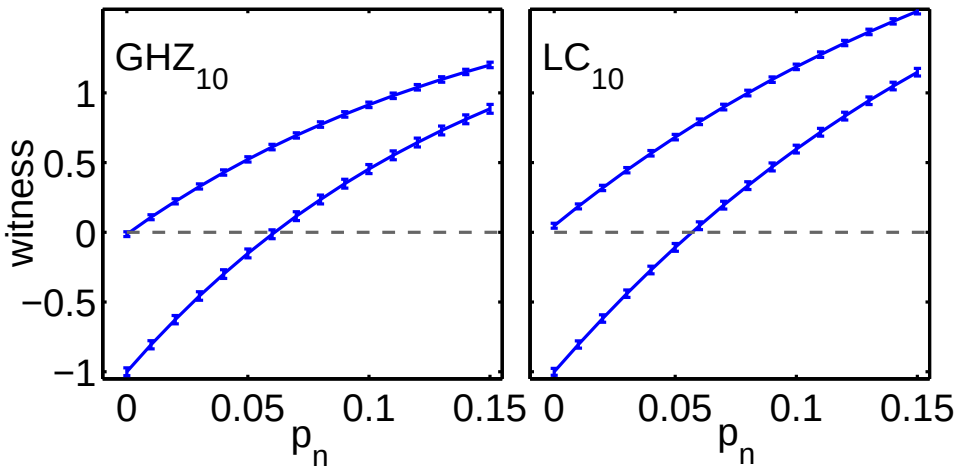

Figure 6.3.2: The entanglement witness $\langle W_{G_n} \rangle$ under different state preparation errors p_n for GHZ (GHZ_{10}) and cluster (LC_{10}) states before (upper lines) and after (lower lines) corection of the detection error (error rate $p = 0.03$). The error bars are obtained by assuming $N = 5000$ rounds of measurements in each detection setting.

6.5 Chapter Summary

In summary, we have shown a method to correct any detection error through simple processing of the experimental data. The method applies to measurements in general many-particle settings, with or without separate addressing. Moreover the method does not require change of the experimental setup and works under arbitrary magnitudes of the detection noise, as long as the error magnitude has been calibrated. The cost of this method is moderate as it only requires repetition of the same experiment by some additional rounds to gain enough statistics and thus the method can readily apply to many experimental settings used in quantum state engineering.

CHAPTER VII

Conclusions

7.1 Summary

In this dissertation, we have investigated several topics centering around quantum information processing with atomic, molecular and optical systems. For the trapped ion platform, we first discussed construction of a scalable boson sampler with the transverse motional phonons of a chain of ions in a linear Paul trap in Chapter II. We devised a complete scheme for the laser assisted initialization, universal mode mixing and projective readout of the final state. Our protocol is based on the conventional Paul trap so we believe it is easier to realize than other protocols based on novel strucutres like microtrap arrays [112]. Compared to the original optical realization [15–18], our state initialization is deterministic and does not suffer low Fock state generation rate and should be much easier to scale up to the interesting regime with 20-30 bosons.

In Chapter III, as a second topic we discussed a spatial refocusing approach to effective achieve single ion addressing with a few interfering Gaussian beams whose width is comparable to the ion spacing. We used two-ion quantum gates to demonstrate that typically only a few correction pulses

are needed to significantly increase the operation fidelity. The cost in additional laser power and resistance to control noise were analyzed. It turned out that the overhead is moderate as long as the Gaussian beam width is only slightly larger than the ion spacing.

We then extended the transverse motion mediated conditional phase flip gate to the regime where ion micromotion is non-negligible in Chapter IV. A rigorous mathematical framework was established for the description of ion micromotion and with the two-ion case as an example the design of quantum gates with micromotion taken into account was demonstrated for the first time. Compared to the case without micromotion, typically the number of control parameters needs to double to achieve similar performance. However, the upside is that we no longer need to restrict the ion crystal geometry to be 1D to avoid micromotion. We can now have a 2D crystal and still perform high fidelity operations to the ions. This might turn out an alternative way to scale up the trapped ion quantum computer.

In Chapter V we turned to cold atom gas, and explored how to efficiently squeeze a collection of spins with dynamically applied pulses. We showed that by adding coherent spin rotation pulses, even a single-axis twisting Hamiltonian can squeeze the spin state to close to the Heisenberg limit, typically achieved with a two-axis twisting Hamiltonian that is more complicated. The disadvantage compared to the real two-axis twisting case is a longer evolution time. So essentially this approach offers a trade-off between squeezing quality and evolution time.

Finally in Chapter VI we considered the general problem of state detection with faulty detectors. Real detectors of any kind have a non-zero error rate. This detector induced noise could render the genuine entanglement properties in the target system invisible, i.e. entanglement witnesses may fail to report. However after simple statistical post-processing of data we can reveal the true entanglement properties without bias, at the expense of increasing the errorbars. In other words we could remove the systematic bias at the expense of increasing statistical fluctuation. One thus

needs to increase the number of repetitions to control the uncertainty.

7.2 Outlook

Based on the previous works both presented in this dissertation and in the literature, we now idenitify several possible directions for future research work in this field.

Micromotion in trapped ion quantum computation/simulation. Our demonstration in Chapter III with two ions has proved that in principle high fidelity operations can be carried in presence of micromotion. But a more singificant and convincing example would be gate operations in a real 2D ion crystal. In advancing to 2D there are also several new theoretical challenges. Also the computation becomes more involved. So we leave the 2D case as future work. On the other hand, with the mathematical description of ion micromotion we developed, we can study the implications of micromotion for other applications of the ion platform, e.g. quantum simulation. In most previous works on quantum simulation with trapped ions micromotion is ignored. We can apply our formalism to systematically analyze whether micromotion would change the general picture significantly or bring new features.

Optimal spin squeezing for precision measurement. Although the optimization technique used in Chapter V enhances squeezing significantly compared to the one-axis twisting scheme, the evolution time is still longer than what experimentalists would like. It is worth further investigation to find pulse sequences that take less time. Adopting an alternative parametrization of the pulse, increasing the number of control parameters, and constraining the overall evolution time are possible solutions to try out next.

Boson sampling on other platforms. There now exist two possible platforms for realizing boson

sampling, photons and phonons in ion crystals. It is possible that there exists more suitable platforms. We can explore boson sampling with neutral atoms/molecules confined in a optical lattice or other kind of bosons hosted by some artificial solid state structures. The race for building a large scale boson sampler has just started and it is still an open question which platform will stand out as the winner.

Statistical methods in quantum information. Our study in Chapter VI is only a minor example of the application of statistical methods in quantum physics experiments. Quantum mechanics is probabilistic in nature and the large body of statistics naturally apply to quantum experiments. In recent years there appeared a lot of works that transfered powerful statistical methods (e.g. compressed sensing) to the field of quantum information, with successful applications in quantum state/process tomography and benchmarking [113–122]. We expect a lot more to be done along this direction.

APPENDICES

APPENDIX A
Trapped Ion Gate Fidelity at Finite Temperature

In this appendix we will show how to calculate the gate fidelity of a trapped ion conditional phase flip (CPF) gate at finite temperature. For the simplified case where only two ions are illuminated by laser, i.e. only $F_i, F_j \neq 0$, which means $\phi_k = 0$, if $k \neq i, j$ and $\phi_{pq} = 0$ unless $\{p, q\} = \{i, j\}$. The quantities ϕ_k and ϕ_{ij} are defined in the main text of Chapter I. The We have a simple form of $U(\tau)$ written with the internal state basis of the illuminated ions i and j $|00\rangle, |01\rangle, |10\rangle, |11\rangle$:

$$U(\tau) = \begin{pmatrix} e^{i\Phi_{00}} & & & \\ & e^{i\Phi_{01}} & & \\ & & e^{i\Phi_{10}} & \\ & & & e^{i\Phi_{11}} \end{pmatrix},$$

where

$$\begin{aligned} i\Phi_{00} &= i(\phi_i + \phi_j + \phi_{ij}) \\ i\Phi_{01} &= i(\phi_i - \phi_j - \phi_{ij}) \\ i\Phi_{10} &= i(-\phi_i + \phi_j - \phi_{ij}) \\ i\Phi_{11} &= i(-\phi_i - \phi_j + \phi_{ij}) \end{aligned}$$

And we assume the initial state is $|\Phi_0\rangle = 1/2(|0\rangle + |1\rangle) \otimes (|0\rangle + |1\rangle)$. Now we have

$$U(\tau)\,|\Psi_0\rangle\,\langle\Psi_0|\,U(\tau)^\dagger = \frac{1}{4}\begin{pmatrix} e^{i(\Phi_{00}-\Phi_{00}^\dagger)} & e^{i(\Phi_{00}-\Phi_{01}^\dagger)} & e^{i(\Phi_{00}-\Phi_{10}^\dagger)} & e^{i(\Phi_{00}-\Phi_{11}^\dagger)} \\ e^{i(\Phi_{01}-\Phi_{00}^\dagger)} & e^{i(\Phi_{01}-\Phi_{01}^\dagger)} & e^{i(\Phi_{01}-\Phi_{10}^\dagger)} & e^{i(\Phi_{01}-\Phi_{11}^\dagger)} \\ e^{i(\Phi_{10}-\Phi_{00}^\dagger)} & e^{i(\Phi_{10}-\Phi_{01}^\dagger)} & e^{i(\Phi_{10}-\Phi_{10}^\dagger)} & e^{i(\Phi_{10}-\Phi_{11}^\dagger)} \\ e^{i(\Phi_{11}-\Phi_{00}^\dagger)} & e^{i(\Phi_{11}-\Phi_{01}^\dagger)} & e^{i(\Phi_{11}-\Phi_{10}^\dagger)} & e^{i(\Phi_{11}-\Phi_{11}^\dagger)} \end{pmatrix}$$

where in the above we made use of the fact that $e^{i\phi_i}$ is a displacement operator $D(\alpha)$ for a quantum harmonic oscillator and that $D(\alpha)D(\beta) = e^{(\alpha\beta^* - \alpha^*\beta)}D(\alpha+\beta)$. Here our $\alpha_j^k \alpha_i^{k*}$ are real quantities so the first factor is zero. resulting $D(\alpha_i^k)D(\alpha_j^k) = D(\alpha_i^k + \alpha_j^k)$. Notice also that ϕ_{ij} is a real scalar and ϕ_i, ϕ_j are real too. The trace over motional states can be calculated as

$$\begin{aligned} tr_m(e^{i(\Phi_{00}-\Phi_{01}^\dagger)}) &= tr_m(e^{2i(\phi_j+\phi_{ij})}) \\ &= e^{2i\phi_{ij}} tr_m(e^{2\sum_k[\alpha_j^k a_k^\dagger - \alpha_j^{k*} a_k]}) \\ &= e^{2i\theta}\prod_k tr_m(D(2\alpha_j^k)) \\ &= e^{2i\theta} e^{-\sum_k \frac{\left|2\alpha_j^k\right|^2}{2} coth(\hbar\omega_k/2k_BT)} \end{aligned}$$

where $\theta \equiv \phi_{ij}$ for short.

In the above equation we used the handy formula

$$tr_m[D(\alpha)] = e^{-\frac{|\alpha|^2}{2} coth(\hbar\omega/2k_BT)}$$

Denoting $\Gamma_{i(j)} = tr_m[D(2\alpha_{i(j)})]$ and $\Gamma_{+(-)} = tr_m[D(2(\alpha_i + (-)\alpha_j))]$. Finally we obtain

$$\begin{aligned}
\rho_r &= tr_m\{U(\tau)\left|\Psi_0\right\rangle\left\langle\Psi_0\right|U(\tau)^\dagger\} \\
&= \frac{1}{4}\begin{pmatrix} 1 & \Gamma_j e^{2i\theta} & \Gamma_i e^{2i\theta} & \Gamma_+ \\ \Gamma_j e^{-2i\theta} & 1 & \Gamma_- & \Gamma_i e^{-2i\theta} \\ \Gamma_i e^{-2i\theta} & \Gamma_- & 1 & \Gamma_j e^{-2i\theta} \\ \Gamma_+ & \Gamma_i e^{2i\theta} & \Gamma_j e^{2i\theta} & 1 \end{pmatrix}
\end{aligned}$$

And the fidelity of the gate is

$$\begin{aligned}
F_g &= \left\langle\Psi_0\right|(U_{ij}^{ideal})^\dagger \rho_r U_{ij}^{ideal}\left|\Psi_0\right\rangle \\
&= \frac{1}{2}\begin{pmatrix} e^{-i\pi/4} & e^{+i\pi/4} & e^{+i\pi/4} & e^{-i\pi/4} \end{pmatrix}\frac{1}{4}\begin{pmatrix} 1 & \Gamma_j e^{2i\theta} & \Gamma_i e^{2i\theta} & \Gamma_+ \\ \Gamma_j e^{-2i\theta} & 1 & \Gamma_- & \Gamma_i e^{-2i\theta} \\ \Gamma_i e^{-2i\theta} & \Gamma_- & 1 & \Gamma_j e^{-2i\theta} \\ \Gamma_+ & \Gamma_i e^{2i\theta} & \Gamma_j e^{2i\theta} & 1 \end{pmatrix}\frac{1}{2}\begin{pmatrix} e^{i\pi/4} \\ e^{-i\pi/4} \\ e^{-i\pi/4} \\ e^{i\pi/4} \end{pmatrix} \\
&= \frac{1}{8}\left\{2 + 2(\Gamma_i + \Gamma_j)\sin(2\theta) + \Gamma_+ + \Gamma_-\right\}.
\end{aligned}$$

This is a complicated nonlinear function of the effective laser Rabi frequencies Ω and its optimization is in general hard. However we can approach it approximately. All the exponentials involved can be expanded to leading order

$$e^{-\frac{|\alpha|^2}{2}coth(\hbar\omega/2k_BT)} \approx 1 - \frac{|\alpha|^2}{2}coth(\hbar\omega/2k_BT).$$

This approximation is accurate in the high fidelity regime, where $\alpha_j^k \approx 0$ and $F_g \approx 1$. Since α's are proportional to Ω's, Γ_i, Γ_j and $\Gamma_\pm$ depend on Ω's quadratically. We also impose the constraint that

$\theta = \pi/4$, which is a quadratic constraint on Ω's. This way we can solve this quadratic optimization problem to get good solutions, which can then be verified with the exact expression for fidelity.

APPENDIX B
Demonstration of Boson Sampling

In this appendix we will perform a classical simulation of the Boson sampling experiment to demonstrate how the proposed scheme works. The hopping Hamiltonian for the local phonons is

$$\begin{aligned} H_{hop} &= \sum_{i<j}^{M} t_{i,j}\left(a_i^\dagger a_j + a_i a_j^\dagger\right) \\ &= \sum_{i,j}^{M} a_i^\dagger H_{ij} a_j. \end{aligned}$$

Combining with the ability to phase shift each oscillator, i.e.

$$a_i \rightarrow a_i \exp(-i\theta_i),$$

we can generate a series of Hamiltonians

$$H_{hop}(\vec{\theta}) = \sum_{i,j}^{M} a_i^\dagger H_{ij} a_j \exp\left(i(\theta_i - \theta_j)\right).$$

By tuning the $\vec{\theta}$ vector we have the freedom to engineer the effective Hamiltonian. In addition we are also free to choose the evolution time t for a particular choice of $\vec{\theta}$. So our building block of

the evolution is

$$\begin{aligned} U(\vec{\theta},t) &= \exp\left(-iH_{hop}(\vec{\theta})t\right) \\ &= \exp\left(-i\sum_{i,j}^{M} a_i^{\dagger} H_{ij} \exp\left(i(\theta_i-\theta_j)\right) a_j\right) \end{aligned}$$

Noting that the Hamlitonians $H_{hop}(\vec{\theta})$ are quadratic in a and $a^{\dagger}$, a canonical transformation can be performed to find the normal modes b_i satisfying $b_i = u_{ij}a_j$ so that

$$U(\vec{\theta},t) = \exp\left(-i\sum_{j} D_{jj} b_j^{\dagger} b_j\right)$$

where D is a diagonal matrix resulting from the canonical transformation. This evolution operator is nothing more than a set of phase shifters for the phonon modes b_j, each of which having a phase shift D_{jj}. Therefore the overall effect of $U(\vec{\theta},t)$ can be described as a three-step process: (1) do a basis transformation from a_i to b_j; (2) phase shift each mode b_j; (3) transform back to the original basis. Thus the output of $U(\vec{\theta},t)$ can be related to the input as

$$\begin{aligned} \vec{a}' &= u^{\dagger} diag(e^{-iD_{11}}, e^{-iD_{22}}, \cdots) u\vec{a} \\ &= \Lambda(\vec{\theta},t)\vec{a}. \end{aligned}$$

The universality of the model was established in the main text of Chapter II, so one can concatinate the building blocks $\Lambda(\theta,t)$ to form an arbitrary N-dimensional unitary in principle. Notice that the computation of $\Lambda(\theta,t)$ given parameters$\vec{\theta}$ and t only requires diagonalizing an $N \times N$ matrix so it can be done very efficiently.

Now let us work out a numerical example and study the effect of control noise in the $\vec{\theta}$ vectors.

We assume $N = 10$ ions, calculated the equilibrium positions in a trap with aspect ratio $\omega_x/\omega_z = 10$, and found the hopping coefficients $t_{ij} = t_0/\left|z_i^0 - z_j^0\right|^3$. We consider a three stage evolution $U_3 = \prod_{i=1}^{3} U(\vec{\theta}_i, t)$ with randomly chosen $\vec{\theta}_i$ and fixed $t = 1/t_0$. Following the approach above, the corresponding $\Lambda_3 = \prod_{i=1}^{3} \Lambda(\vec{\theta}_i, t)$ can be easily found. Then we introduce Gaussian random additive errors to all the $\vec{\theta}_i$ with zero mean and standard deviation σ. For different values of σ we calculate the distance between $\Lambda_3^{'}$ with noise and the ideal Λ_3. To remove the irrelevant local phase factors for each mode, we define a distance measure as follows

$$dist(\Lambda, \Lambda^{'}) \equiv 1 - \frac{1}{N} \sum_{j=1}^{N} \left| \sum_{i=1}^{N} \Lambda_{ij}^{*} \Lambda_{ij}^{'} \right|.$$

This distance measure essentially is determined by the average absolute value of the inner products of corresponding column vectors from the two unitaries. Only when each column of Λ and $\Lambda^{'}$ is the same up to a phase factor, the distance is zero. We plot the distance from the ideal unitary as a function of σ in Fig. B.1. We can see from the figure that Λ_3 is quite robust against random noise in the parameters $\vec{\theta}_i$.

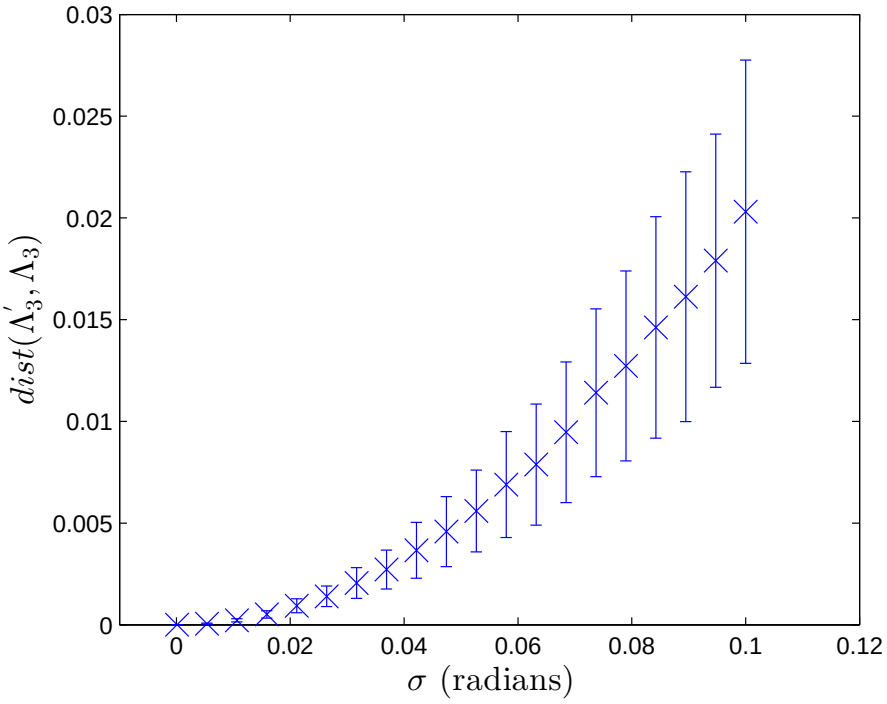

Figure B.1: Distance between the transformation with error Λ_3' and the ideal transformation Λ_3, as a function of the standard deviation of the noise σ. Each data point is obtained with 1000 randomized simulation of the noise for a fixed set of arbitrary $\vec{\theta}_i$. The errorbar is show one standard deviation of the quantity. See text for detailed parameters used for the system.

APPENDIX C
Solving the Envelope Function with Toeplitz Matrix Theory

According to the Toeplitz matrix theory, the general solution to the equation $M_{lj}f_{ji} = \delta_{li}$ has the form $f_{ji} = \sum_k c_k^{+/-} (a_k)^{j-i}$ where c_k^+ and c_k^- are for the regions $j > i$ and $j < i$, respectively. Here a_k are the roots of the polynomial $P_n(x) = x^n \left(1 + \sum_{m=1}^n \left(1/x^m + x^m\right) \gamma^{m^2}\right)$ and $c_k^{+/-}$ are coefficients to be determined (the band-width of the matrix M_{lj} is $2n+1$). Our first observation is that the roots come in pairs (a , $1/a$) due to the symmetry $x \leftrightarrow 1/x$. Thus f_{ji} is composed of terms like $c_k^{+/-}(a_k)^{j-i}$ decaying (increasing) exponentially with $|j-i|$ if $a_k < 1$ ($a_k > 1$). In the region $j > i$ ($j < i$) , boundary condition at $|j-i| \to \infty$ requires $c_k = 0$ for $a_k > 1$ ($a_k > 1$). Note that in the large $|j-i|$ limit, the a_k closest to the unity should dominate since other components die out more quickly. Next we prove that $-\gamma$ (and hence $-1/\gamma$) is a root of $P_n(x)$ when n is sufficiently large.

$$\begin{aligned}
\frac{P_n(-\gamma)}{(-\gamma)^n} &= 1 + \sum_{m=1}^{n} (-1)^m \left(\gamma^{m^2+m} + \gamma^{m^2-m}\right) \\
&= 1 + \sum_{m=1}^{n} (-1)^m \gamma^{m^2+m} + \sum_{m=0}^{n-1} (-1)^{m+1} \gamma^{m^2+m} \\
&= (-1)^n \gamma^{n^2+n} + \sum_{m=1}^{n-1} (-1)^m (1-1) \gamma^{m^2+m} \\
&= (-1)^n \gamma^{n^2+n} \to 0, \text{ when } n \text{ is large.}
\end{aligned}$$

The characteristic quantities of $P_n(x)$ are γ, γ^4, γ^9, ..., of which the one closest to the unity is γ.

This leads us to conjecture $(-\gamma)$ is the root of $P_n(x)$ closest to 1 in magnitude. This turns out to be true. Since $\tilde{P}_n(x) = P_n(x)/x^n > 0$ when $x > 0$, there is no positive root. Let us focus on the interval $[-1,0)$. For $n = 1$, $\tilde{P}_1(x) = 1 + \gamma(1/x + x)$ is monotonically decreasing from $\tilde{P}_1(-1) = 1 - 2\gamma$ to $\tilde{P}_1(0^-) \to -\infty$ and there is one root in this interval: $\frac{-1+\sqrt{1-4\gamma^2}}{2\gamma} \approx \frac{-1+1-2\gamma^2}{2\gamma} = -\gamma$. When increasing n by 1, we include one more term $Q_{n+1}(x) = \left(1/x^{n+1} + x^{n+1}\right)\gamma^{(n+1)^2}$. Due to the small factor $\gamma^{(n+1)^2}$, the contribution of Q_{n+1} can be comparable with that of Q_n only when $|x| \lesssim \gamma^{2n+1}$. Since $Q_n(0^-)$ approaches $+\infty$ for even n and $-\infty$ for odd n and Q_n is always monotonic on $[-1,0)$, adding one more term always introduces one more turning point in $\tilde{P}_n(x)$ and thus adds one more root with magnitude much smaller than the previous roots. Therefore $(-\gamma)$ is the root with the largest magnitude by far on $[-1,0)$. We therefore conclude $f_{ji} \propto (-\gamma)^{|j-i|}$ when $|j-i|$ is large.

APPENDIX D
Solving Mathieu Equation with a Constant Drive

In this appendix, we show in detail how to solve the Mathieu equation with a constant drive term.

$$\frac{d^2u}{d\xi^2} + (a - 2q\cos(2\xi))\,u = f_0$$

Let us assume that $u(\xi) = \sum_{n=0}^{\infty} c_{2n}\cos(2n\xi)$ and insert it into the equation. After re-organization we get

$$ac_0 - qc_2 + \sum_{n=1}^{\infty}\left[(a-4n^2)c_{2n} - q(c_{2n-2}+c_{2n+2}) - qc_0\delta_{n,1}\right]\cos(2nt) = f_0.$$

Defining $D_{2n} \equiv (a-4n^2)/q$, we have the following set of linear equations

$$\begin{aligned} ac_0 - qc_2 &= f_0 \\ c_{2n} - \frac{1}{D_{2n}}(c_{2n-2} + c_{2n+2} + c_0\delta_{n,1}) &= 0. \end{aligned}$$

In matrix form,

$$\begin{pmatrix} a & -q & 0 & \cdots & & 0 \\ -\frac{2}{D_2} & 1 & -\frac{1}{D_2} & & & \\ 0 & -\frac{1}{D_4} & 1 & -\frac{1}{D_4} & & \\ \vdots & & -\frac{1}{D_6} & 1 & -\frac{1}{D_6} & \\ & & & \ddots & \ddots & \\ 0 & & & & & \end{pmatrix} \cdot \begin{pmatrix} c_0 \\ c_2 \\ c_4 \\ \vdots \\ \\ \end{pmatrix} = \begin{pmatrix} f_0 \\ 0 \\ 0 \\ \vdots \\ \\ \end{pmatrix}. \tag{7.2.1}$$

The factor $1/D_{2n}$ decreases very fast as n increases and we can truncate the expansion of $u(\xi)$ at a small n. Numerically we observe that typically keeping up toc_4 already gives enough accuracy. We can thus get a very accurate analytical expressions

$$\begin{aligned} c_0 &\approx \frac{64+a(a-20)-q^2}{(32-3a)q^2+a(a-4)(a-16)}, \\ c_2 &\approx \frac{2(a-16)q}{(32-3a)q^2+a(a-4)(a-16)}, \\ c_4 &\approx \frac{2q^2}{(32-3a)q^2+a(a-4)(a-16)}. \end{aligned}$$

For the example in the main text of Chapter IV, $a_r = -0.0388$ and $q_r = 0.283$, we have $c_0 = 1132.8$ and $u_r(\xi) = c_0\,[1 - 0.14\cos(2\xi) + 0.0025\cos(4\xi) + \cdots]$.

The coefficient c_0 is the micromotion corrected equilibrium position and should be consistent with u_0 around which we expand the Coulomb potential in the first place. Thus we should determine u_0/c_0 self-consistently. Taking the relative motion in the main text of Chapter IV as an example, since both $a_{\mathrm{r}} \equiv \frac{-16ZeU_0}{md_0^2\Omega_T^2} + \frac{4Z^2e^2}{\pi\varepsilon_0 m u_o^3 \Omega_T^2}$ and $f_0 \equiv \frac{6e^2}{\pi\varepsilon_0 m u_0^2 \Omega_T^2}$ are functions of u_0, then the self-consistent

equation

$$u_0 = c_0 \quad \approx \quad \frac{64 + a_{\mathrm{r}}(a_{\mathrm{r}} - 20) - q_{\mathrm{r}}^2}{(32 - 3a_{\mathrm{r}})q_{\mathrm{r}}^2 + a_{\mathrm{r}}(a_{\mathrm{r}} - 4)(a_{\mathrm{r}} - 16)}$$

gives the correct u_0. With hje iterative method it typically takes only a few iterations to converge to the correct value when starting from a proper initial value of u_0.

APPENDIX E
Proof of Inverse Matrix Formula

In this appendix, we prove the inverse matrix formula Eq. (6.2.7) in the main text of Chapter VI. We can relate the L matrix to the M matrix defined in Eq. (6.2.3). Denote the space of n-bit binary strings with i bits of 1 as S_i, and S_i has dimension $\binom{n}{i}$. The matrix element $M_{\sigma\rho}$ represents the probability of recording a n-bit binary string ρ as σ, and L_{ij} is the probability of recording a signal $\rho \in S_j$ as any string in the S_i space. As a collective measurement does not distinguish the binary strings in the same space S_i, L_{ij} is related to $M_{\sigma\rho}$ by $L_{ij} = \sum_{\sigma\in S_i} M_{\sigma\rho}$.The probability L_{ij} is apparently independent of the exact form of ρ, as long as ρ belongs to the space S_j, so we can pick up any $\rho \in S_j$ in $L_{ij} = \sum_{\sigma\in S_i} M_{\sigma\rho}$ without alternation to the result of summation. From Eq. (6.2.4) in the main text, we know $M^{-1}_{\mu\nu} = M_{\mu\nu}\left(p'_0, p'_1\right)$. Let us define

$$N_{jk} \equiv \sum_{\mu\in S_j} M^{-1}_{\mu\nu} = \sum_{\mu\in S_j} M_{\mu\nu}\ \left(p'_0, p'_1\right) = L_{jk}\left(p'_0, p'_1\right),$$

where ν is an arbitrary element in S_k. Now we show that N gives inverse of the matrix L:

$$\begin{aligned}\sum_j L_{ij}N_{jk} &= \sum_j \sum_{\sigma\in S_i,\mu\in S_j} M_{\sigma\rho}M^{-1}_{\mu\nu} \\ = \sum_{\sigma\in S_i}\sum_j\sum_{\mu\in S_j} M_{\sigma\mu}M^{-1}_{\mu\nu} &= \sum_{\sigma\in S_i}\delta_{\sigma\nu} = \delta_{ik}\end{aligned}$$

In the second line, we have changed the subscript ρ in $M_{\sigma\rho}$ to μ as both ρ, μ belong to S_j. This proves Eq. (6.2.7) in the main text of Chapter VI.

BIBLIOGRAPHY

BIBLIOGRAPHY

[1] R. P. Feynman. Simulating physics with computers. *International Journal of Theoretical Physics*, 21:467–488, June 1982.

[2] D. Deutsch. Quantum theory, the church-turing principle and the universal quantum computer. In *Proceedings of the Royal Society of London*, volume 400 of *A. Mathematical and Physical Sciences*, pages 97–117, July 1985.

[3] C. H. Bennet and G. Brassard. Quantum cryptography: Public key distribution and coin tossing. In *Proceedings of the IEEE International Conference on Computers, Systems, and Signal Processing*, page 175, 1984.

[4] D. Deutsch and R. Jozsa. Rapid solutions of problems by quantum computation. In *Proceedings of the Royal Society of London*, volume 439, page 553, 1985.

[5] Peter W. Shor. Polynomial-time algorithms for prime factorization and discrete logarithms on a quantum computer. *SIAM Journal on Computing*, 26(5):1484–1509, October 1997.

[6] B. E. King. *Quantum State Engineering and Information Processing with Trapped Ions*. PhD thesis, University of Colorado at Boulder, 1999.

[7] J. I. Cirac and P. Zoller. Quantum computations with cold trapped ions. *Physical Review Letters*, 74(20):4091–4094, May 1995.

[8] Ferdinand Schmidt-Kaler, Hartmut Häffner, Mark Riebe, Stephan Gulde, Gavin P. T. Lancaster, Thomas Deuschle, Christoph Becher, Christian F. Roos, Jürgen Eschner, and Rainer Blatt. Realization of the Cirac-Zoller controlled-NOT quantum gate. *Nature*, 422(6930):408–411, March 2003.

[9] Anders Sørensen and Klaus Mølmer. Quantum computation with ions in thermal motion. *Physical Review Letters*, 82(9):1971–1974, March 1999.

[10] Shi-Liang Zhu, C. Monroe, and L.-M. Duan. Arbitrary-speed quantum gates within large ion crystals through minimum control of laser beams. *Europhysics Letters*, 73(4):485, February 2006.

[11] Shi-Liang Zhu, C. Monroe, and L.-M. Duan. Trapped ion quantum computation with transverse phonon modes. *Physical Review Letters*, 97(5):050505, August 2006.

[12] D. F. V. James. Quantum dynamics of cold trapped ions with application to quantum computation. *Applied Physics B*, 66(2):181–190, February 1998.

[13] Scott Aaronson and Alex Arkhipov. The computational complexity of linear optics. In *Proceedings of the Forty-third Annual ACM Symposium on Theory of Computing*, STOC '11, pages 333–342, New York, NY, USA, 2011. ACM.

[14] L. G. Valiant. The complexity of computing the permanent. *Theoretical Computer Science*, 8(2):189–201, 1979.

[15] Justin B. Spring, Benjamin J. Metcalf, Peter C. Humphreys, W. Steven Kolthammer, Xian-Min Jin, Marco Barbieri, Animesh Datta, Nicholas Thomas-Peter, Nathan K. Langford, Dmytro Kundys, James C. Gates, Brian J. Smith, Peter G. R. Smith, and Ian A. Walmsley. Boson sampling on a photonic chip. *Science*, 339(6121):798–801, February 2013.

[16] Matthew A. Broome, Alessandro Fedrizzi, Saleh Rahimi-Keshari, Justin Dove, Scott Aaronson, Timothy C. Ralph, and Andrew G. White. Photonic boson sampling in a tunable circuit. *Science*, 339(6121):794–798, February 2013.

[17] Max Tillmann, Borivoje Dakic, Rene Heilmann, Stefan Nolte, Alexander Szameit, and Philip Walther. Experimental boson sampling. *Nature Photonics*, 7(7):540–544, July 2013.

[18] Andrea Crespi, Roberto Osellame, Roberta Ramponi, Daniel J. Brod, Ernesto F. Galvao, Nicolo Spagnolo, Chiara Vitelli, Enrico Maiorino, Paolo Mataloni, and Fabio Sciarrino. Integrated multimode interferometers with arbitrary designs for photonic boson sampling. *Nature Photonics*, 7(7):545–549, July 2013.

[19] C. Gogolin, M. Kliesch, L. Aolita, and J. Eisert. Boson-sampling in the light of sample complexity. *arXiv:1306.3995 [quant-ph]*, June 2013.

[20] Scott Aaronson and Alex Arkhipov. BosonSampling is far from uniform. *arXiv:1309.7460 [quant-ph]*, September 2013.

[21] Stefan Scheel. Permanents in linear optical networks. *arXiv:quant-ph/0406127*, June 2004.

[22] D. Porras and J. I. Cirac. Bose-Einstein condensation and strong-correlation behavior of phonons in ion traps. *Physical Review Letters*, 93(26):263602, December 2004.

[23] X.-L. Deng, D. Porras, and J. I. Cirac. Quantum phases of interacting phonons in ion traps. *Physical Review A*, 77(3):033403, March 2008.

[24] F. Diedrich, J. C. Bergquist, Wayne M. Itano, and D. J. Wineland. Laser cooling to the zero-point energy of motion. *Physical Review Letters*, 62(4):403–406, January 1989.

[25] C. Monroe, D. M. Meekhof, B. E. King, S. R. Jefferts, W. M. Itano, D. J. Wineland, and P. Gould. Resolved-sideband raman cooling of a bound atom to the 3D zero-point energy. *Physical Review Letters*, 75(22):4011–4014, November 1995.

[26] B. E. King, C. S. Wood, C. J. Myatt, Q. A. Turchette, D. Leibfried, W. M. Itano, C. Monroe, and D. J. Wineland. Cooling the collective motion of trapped ions to initialize a quantum register. *Physical Review Letters*, 81(7):1525–1528, August 1998.

[27] G. Poulsen, Y. Miroshnychenko, and M. Drewsen. Efficient ground-state cooling of an ion in a large room-temperature linear paul trap with a sub-hertz heating rate. *Physical Review A*, 86(5):051402, November 2012.

[28] D. M. Meekhof, C. Monroe, B. E. King, W. M. Itano, and D. J. Wineland. Generation of nonclassical motional states of a trapped atom. *Physical Review Letters*, 76(11):1796–1799, March 1996.

[29] Michael Reck, Anton Zeilinger, Herbert J. Bernstein, and Philip Bertani. Experimental realization of any discrete unitary operator. *Physical Review Letters*, 73(1):58–61, July 1994.

[30] Hui Khoon Ng, Daniel A. Lidar, and John Preskill. Combining dynamical decoupling with fault-tolerant quantum computation. *Physical Review A*, 84(1):012305, July 2011.

[31] T. Watanabe, S. Nomura, K. Toyoda, and S. Urabe. Sideband excitation of trapped ions by rapid adiabatic passage for manipulation of motional states. *Physical Review A*, 84(3):033412, September 2011.

[32] Rachel Noek, Geert Vrijsen, Daniel Gaultney, Emily Mount, Taehyun Kim, Peter Maunz, and Jungsang Kim. High speed, high fidelity detection of an atomic hyperfine qubit. *arXiv:1304.3511 [quant-ph]*, April 2013.

[33] G.-D. Lin, S.-L. Zhu, R. Islam, K. Kim, M.-S. Chang, S. Korenblit, C. Monroe, and L.-M. Duan. Large-scale quantum computation in an anharmonic linear ion trap. *EPL (Europhysics Letters)*, 86(6):60004, June 2009.

[34] Jonathan P. Home, David Hanneke, John D. Jost, Jason M. Amini, Dietrich Leibfried, and David J. Wineland. Complete methods set for scalable ion trap quantum information processing. *Science*, 325(5945):1227–1230, September 2009.

[35] Marco Anderlini, Patricia J. Lee, Benjamin L. Brown, Jennifer Sebby-Strabley, William D. Phillips, and J. V. Porto. Controlled exchange interaction between pairs of neutral atoms in an optical lattice. *Nature*, 448(7152):452–456, July 2007.

[36] J. R. Petta, A. C. Johnson, J. M. Taylor, E. A. Laird, A. Yacoby, M. D. Lukin, C. M. Marcus, M. P. Hanson, and A. C. Gossard. Coherent manipulation of coupled electron spins in semiconductor quantum dots. *Science*, 309(5744):2180–2184, September 2005.

[37] Matthias Steffen, M. Ansmann, Radoslaw C. Bialczak, N. Katz, Erik Lucero, R. McDermott, Matthew Neeley, E. M. Weig, A. N. Cleland, and John M. Martinis. Measurement of the entanglement of two superconducting qubits via state tomography. *Science*, 313(5792):1423–1425, September 2006.

[38] L. Isenhower, E. Urban, X. L. Zhang, A. T. Gill, T. Henage, T. A. Johnson, T. G. Walker, and M. Saffman. Demonstration of a neutral atom controlled-NOT quantum gate. *Physical Review Letters*, 104(1):010503, January 2010.

[39] T. Wilk, A. Gaëtan, C. Evellin, J. Wolters, Y. Miroshnychenko, P. Grangier, and A. Browaeys. Entanglement of two individual neutral atoms using rydberg blockade. *Physical Review Letters*, 104(1):010502, January 2010.

[40] L. DiCarlo, J. M. Chow, J. M. Gambetta, Lev S. Bishop, B. R. Johnson, D. I. Schuster, J. Majer, A. Blais, L. Frunzio, S. M. Girvin, and R. J. Schoelkopf. Demonstration of two-qubit algorithms with a superconducting quantum processor. *Nature*, 460(7252):240–244, July 2009.

[41] Alberto Politi, Jonathan C. F. Matthews, and Jeremy L. O'Brien. Shor's quantum factoring algorithm on a photonic chip. *Science*, 325(5945):1221–1221, September 2009.

[42] Erik Lucero, R. Barends, Y. Chen, J. Kelly, M. Mariantoni, A. Megrant, P. O'Malley, D. Sank, A. Vainsencher, J. Wenner, T. White, Y. Yin, A. N. Cleland, and John M. Martinis. Computing prime factors with a josephson phase qubit quantum processor. *Nature Physics*, 8(10):719–723, October 2012.

[43] M. D. Reed, L. DiCarlo, S. E. Nigg, L. Sun, L. Frunzio, S. M. Girvin, and R. J. Schoelkopf. Realization of three-qubit quantum error correction with superconducting circuits. *Nature*, 482(7385):382–385, February 2012.

[44] Philipp Schindler, Julio T. Barreiro, Thomas Monz, Volckmar Nebendahl, Daniel Nigg, Michael Chwalla, Markus Hennrich, and Rainer Blatt. Experimental repetitive quantum error correction. *Science*, 332(6033):1059–1061, May 2011.

[45] K. Kim, M.-S. Chang, S. Korenblit, R. Islam, E. E. Edwards, J. K. Freericks, G.-D. Lin, L.-M. Duan, and C. Monroe. Quantum simulation of frustrated ising spins with trapped ions. *Nature*, 465(7298):590–593, June 2010.

[46] R. Islam, E. E. Edwards, K. Kim, S. Korenblit, C. Noh, H. Carmichael, G.-D. Lin, L.-M. Duan, C.-C. Joseph Wang, J. K. Freericks, and C. Monroe. Onset of a quantum phase transition with a trapped ion quantum simulator. *Nature Communications*, 2:377, July 2011.

[47] Julio T. Barreiro, Markus Müller, Philipp Schindler, Daniel Nigg, Thomas Monz, Michael Chwalla, Markus Hennrich, Christian F. Roos, Peter Zoller, and Rainer Blatt. An open-system quantum simulator with trapped ions. *Nature*, 470(7335):486–491, February 2011.

[48] B. P. Lanyon, C. Hempel, D. Nigg, M. Müller, R. Gerritsma, F. Zähringer, P. Schindler, J. T. Barreiro, M. Rambach, G. Kirchmair, M. Hennrich, P. Zoller, R. Blatt, and C. F. Roos. Universal digital quantum simulation with trapped ions. *Science*, 334(6052):57–61, October 2011. PMID: 21885735.

[49] Michael A. Nielsen and Isaac L. Chuang. *Quantum Computation and Quantum Information*. Cambridge Series on Information and the Natural Sciences. Cambridge University Press, Cambridge, UK, 2000.

[50] Changsoon Kim, C. Knoernschild, Bin Liu, and Jungsang Kim. Design and characterization of MEMS micromirrors for ion-trap quantum computation. *IEEE Journal of Selected Topics in Quantum Electronics*, 13(2):322–329, March 2007.

[51] C. Knoernschild, X. L. Zhang, L. Isenhower, A. T. Gill, F. P. Lu, M. Saffman, and J. Kim. Independent individual addressing of multiple neutral atom qubits with a micromirror-based beam steering system. *Applied Physics Letters*, 97(13):134101, September 2010.

[52] Waseem S. Bakr, Jonathon I. Gillen, Amy Peng, Simon Fölling, and Markus Greiner. A quantum gas microscope for detecting single atoms in a hubbard-regime optical lattice. *Nature*, 462(7269):74–77, November 2009.

[53] Jacob F. Sherson, Christof Weitenberg, Manuel Endres, Marc Cheneau, Immanuel Bloch, and Stefan Kuhr. Single-atom-resolved fluorescence imaging of an atomic mott insulator. *Nature*, 467(7311):68–72, September 2010.

[54] Mark Saffman. Addressing atoms in optical lattices with bessel beams. *Optics Letters*, 29(9):1016–1018, 2004.

[55] G. S. Agarwal and K. T. Kapale. Subwavelength atom localization via coherent population trapping. *Journal of Physics B: Atomic, Molecular and Optical Physics*, 39(17):3437, September 2006.

[56] Jaeyoon Cho. Addressing individual atoms in optical lattices with standing-wave driving fields. *Physical Review Letters*, 99(2):020502, July 2007.

[57] D. D. Yavuz and N. A. Proite. Nanoscale resolution fluorescence microscopy using electromagnetically induced transparency. *Physical Review A*, 76(4):041802, October 2007.

[58] Alexey V. Gorshkov, Liang Jiang, Markus Greiner, Peter Zoller, and Mikhail D. Lukin. Coherent quantum optical control with subwavelength resolution. *Physical Review Letters*, 100(9):093005, March 2008.

[59] D. Viscor, J. L. Rubio, G. Birkl, J. Mompart, and V. Ahufinger. Single-site addressing of ultracold atoms beyond the diffraction limit via position-dependent adiabatic passage. *Physical Review A*, 86(6):063409, December 2012.

[60] J. A. Miles, Z. J. Simmons, and D. D. Yavuz. Subwavelength localization of atomic excitation using electromagnetically induced transparency. *Physical Review X*, 3(3):031014, September 2013.

[61] Christof Weitenberg, Manuel Endres, Jacob F. Sherson, Marc Cheneau, Peter Schauß, Takeshi Fukuhara, Immanuel Bloch, and Stefan Kuhr. Single-spin addressing in an atomic mott insulator. *Nature*, 471(7338):319–324, March 2011.

[62] Kenneth R. Brown, Aram W. Harrow, and Isaac L. Chuang. Arbitrarily accurate composite pulse sequences. *Physical Review A*, 70(5):052318, November 2004.

[63] Y. Tomita, J. T. Merrill, and K. R. Brown. Multi-qubit compensation sequences. *New Journal of Physics*, 12(1):015002, January 2010.

[64] Ulrich Haeberlen. *High Resolution NMR in Solids Selective Averaging*. Advances in Magnetic Resonance Series, Supplement 1. Academic Press, New York, 1976.

[65] William F. Trench. An algorithm for the inversion of finite toeplitz matrices. *Journal of the Society for Industrial and Applied Mathematics*, 12(3):515–522, September 1964.

[66] S. Korenblit, D. Kafri, W. C. Campbell, R. Islam, E. E. Edwards, Z.-X. Gong, G.-D. Lin, L.-M. Duan, J. Kim, K. Kim, and C. Monroe. Quantum simulation of spin models on an arbitrary lattice with trapped ions. *New Journal of Physics*, 14(9):095024, September 2012.

[67] James D. Siverns, Seb Weidt, Kim Lake, Bjoern Lekitsch, Marcus D. Hughes, and Winfried K. Hensinger. Optimization of two-dimensional ion trap arrays for quantum simulation. *New Journal of Physics*, 14(8):085009, August 2012.

[68] J. M. Amini, H. Uys, J. H. Wesenberg, S. Seidelin, J. Britton, J. J. Bollinger, D. Leibfried, C. Ospelkaus, A. P. VanDevender, and D. J. Wineland. Toward scalable ion traps for quantum information processing. *New Journal of Physics*, 12(3):033031, March 2010.

[69] M. Saffman, T. G. Walker, and K. Mølmer. Quantum information with rydberg atoms. *Reviews of Modern Physics*, 82(3):2313–2363, August 2010.

[70] R. Dumke, M. Volk, T. Müther, F. B. J. Buchkremer, G. Birkl, and W. Ertmer. Micro-optical realization of arrays of selectively addressable dipole traps: A scalable configuration for quantum computation with atomic qubits. *Physical Review Letters*, 89(9):097903, August 2002.

[71] Silvia Bergamini, Benoît Darquié, Matthew Jones, Lionel Jacubowiez, Antoine Browaeys, and Philippe Grangier. Holographic generation of microtrap arrays for single atoms by use of a programmable phase modulator. *Journal of the Optical Society of America B*, 21(11):1889–1894, November 2004.

[72] R. Islam, C. Senko, W. C. Campbell, S. Korenblit, J. Smith, A. Lee, E. E. Edwards, C.-C. J. Wang, J. K. Freericks, and C. Monroe. Emergence and frustration of magnetism with variable-range interactions in a quantum simulator. *Science*, 340(6132):583–587, May 2013. PMID: 23641112.

[73] H. Häffner, W. Hänsel, C. F. Roos, J. Benhelm, D. Chek-al kar, M. Chwalla, T. Körber, U. D. Rapol, M. Riebe, P. O. Schmidt, C. Becher, O. Gühne, W. Dür, and R. Blatt. Scalable multiparticle entanglement of trapped ions. *Nature*, 438(7068):643–646, December 2005.

[74] Q. A. Turchette, C. S. Wood, B. E. King, C. J. Myatt, D. Leibfried, W. M. Itano, C. Monroe, and D. J. Wineland. Deterministic entanglement of two trapped ions. *Physical Review Letters*, 81(17):3631–3634, October 1998.

[75] C. A. Sackett, D. Kielpinski, B. E. King, C. Langer, V. Meyer, C. J. Myatt, M. Rowe, Q. A. Turchette, W. M. Itano, D. J. Wineland, and C. Monroe. Experimental entanglement of four particles. *Nature*, 404(6775):256–259, March 2000.

[76] Jan Benhelm, Gerhard Kirchmair, Christian F. Roos, and Rainer Blatt. Towards fault-tolerant quantum computing with trapped ions. *Nature Physics*, 4(6):463–466, June 2008.

[77] B. P. Lanyon, P. Jurcevic, M. Zwerger, C. Hempel, E. A. Martinez, W. Dür, H. J. Briegel, R. Blatt, and C. F. Roos. Measurement-based quantum computation with trapped ions. *Physical Review Letters*, 111(21):210501, November 2013.

[78] M. G. Raizen, J. M. Gilligan, J. C. Bergquist, W. M. Itano, and D. J. Wineland. Ionic crystals in a linear paul trap. *Physical Review A*, 45(9):6493–6501, May 1992.

[79] J. P. Schiffer. Phase transitions in anisotropically confined ionic crystals. *Physical Review Letters*, 70(6):818–821, February 1993.

[80] E. Knill. Quantum computing with realistically noisy devices. *Nature*, 434(7029):39–44, March 2005.

[81] Robert Raussendorf and Jim Harrington. Fault-tolerant quantum computation with high threshold in two dimensions. *Physical Review Letters*, 98(19):190504, May 2007.

[82] A. Mortensen, E. Nielsen, T. Matthey, and M. Drewsen. Observation of three-dimensional long-range order in small ion coulomb crystals in an rf trap. *Physical Review Letters*, 96(10):103001, March 2006.

[83] K. Okada, T. Takayanagi, M. Wada, S. Ohtani, and H. A. Schuessler. Observation of ion coulomb crystals in a cryogenic linear octupole rf ion trap. *Physical Review A*, 80(4):043405, October 2009.

[84] B. Szymanski, R. Dubessy, B. Dubost, S. Guibal, J.-P. Likforman, and L. Guidoni. Large two dimensional coulomb crystals in a radio frequency surface ion trap. *Applied Physics Letters*, 100(17):171110, April 2012.

[85] Michael Drewsen, Thierry Matthey, Anders Mortensen, and Jan Petter Hansen. Direct imaging of thermally excited metastable structures of ion coulomb clusters. *arXiv:1202.2544 [physics]*, February 2012.

[86] N. W. McLachlan. *Theory and Application of Mathieu Functions*. Clarendon Press, Oxford, 1947.

[87] M. Combescure. A quantum particle in a quadrupole radio frequency trap. *Annales de l'institut Henri Poincare (A) Physique theorique*, 44:293–314, 1986.

[88] Lowell S. Brown. Quantum motion in a paul trap. *Physical Review Letters*, 66(5):527–529, February 1991.

[89] R. J. Glauber. The quantum mechanics of trapped wave packets. In *Laser Manipulation of Atoms and Ions*, volume 118 of *Proceedings of the International School of Physics "Enrico Fermi" Course*, 1922.

[90] T. Choi, S. Debnath, T. A. Manning, C. Figgatt, Z.-X. Gong, L.-M. Duan, and C. Monroe. Optimal quantum control of multi-mode couplings between trapped ion qubits for scalable entanglement. *arXiv:1401.1575 [quant-ph]*, January 2014.

[91] Masahiro Kitagawa and Masahito Ueda. Squeezed spin states. *Physical Review A*, 47(6):5138–5143, June 1993.

[92] D. J. Wineland, J. J. Bollinger, W. M. Itano, F. L. Moore, and D. J. Heinzen. Spin squeezing and reduced quantum noise in spectroscopy. *Physical Review A*, 46(11):R6797–R6800, December 1992.

[93] D. J. Wineland, J. J. Bollinger, W. M. Itano, and D. J. Heinzen. Squeezed atomic states and projection noise in spectroscopy. *Physical Review A*, 50(1):67–88, July 1994.

[94] Anders S. Sørensen and Klaus Mølmer. Entanglement and extreme spin squeezing. *Physical Review Letters*, 86(20):4431–4434, May 2001.

[95] A. Sørensen, L.-M. Duan, J. I. Cirac, and P. Zoller. Many-particle entanglement with Bose-Einstein condensates. *Nature*, 409(6816):63–66, January 2001.

[96] L.-M. Duan, J. I. Cirac, and P. Zoller. Quantum entanglement in spinor Bose-Einstein condensates. *Physical Review A*, 65(3):033619, February 2002.

[97] Géza Tóth, Christian Knapp, Otfried Gühne, and Hans J. Briegel. Spin squeezing and entanglement. *Physical Review A*, 79(4):042334, April 2009.

[98] T. Takano, M. Fuyama, R. Namiki, and Y. Takahashi. Spin squeezing of a cold atomic ensemble with the nuclear spin of one-half. *Physical Review Letters*, 102(3):033601, January 2009.

[99] C. Gross, T. Zibold, E. Nicklas, J. Estève, and M. K. Oberthaler. Nonlinear atom interferometer surpasses classical precision limit. *Nature*, 464(7292):1165–1169, April 2010.

[100] Max F. Riedel, Pascal Böhi, Yun Li, Theodor W. Hänsch, Alice Sinatra, and Philipp Treutlein. Atom-chip-based generation of entanglement for quantum metrology. *Nature*, 464(7292):1170–1173, April 2010.

[101] Ian D. Leroux, Monika H. Schleier-Smith, and Vladan Vuletic. Implementation of cavity squeezing of a collective atomic spin. *Physical Review Letters*, 104(7):073602, February 2010.

[102] Zilong Chen, Justin G. Bohnet, Shannon R. Sankar, Jiayan Dai, and James K. Thompson. Conditional spin squeezing of a large ensemble via the vacuum rabi splitting. *Physical Review Letters*, 106(13):133601, March 2011.

[103] Kristian Helmerson and Li You. Creating massive entanglement of Bose-Einstein condensed atoms. *Physical Review Letters*, 87(17):170402, October 2001.

[104] Y. C. Liu, Z. F. Xu, G. R. Jin, and L. You. Spin squeezing: Transforming one-axis twisting into two-axis twisting. *Physical Review Letters*, 107(1):013601, June 2011.

[105] D. Jaksch, J. I. Cirac, and P. Zoller. Dynamically turning off interactions in a two-component condensate. *Physical Review A*, 65(3):033625, March 2002.

[106] Joseph W. Britton, Brian C. Sawyer, Adam C. Keith, C.-C. Joseph Wang, James K. Freericks, Hermann Uys, Michael J. Biercuk, and John J. Bollinger. Engineered two-dimensional ising interactions in a trapped-ion quantum simulator with hundreds of spins. *Nature*, 484(7395):489–492, April 2012.

[107] Souma Chaudhury, Seth Merkel, Tobias Herr, Andrew Silberfarb, Ivan H. Deutsch, and Poul S. Jessen. Quantum control of the hyperfine spin of a Cs atom ensemble. *Physical Review Letters*, 99(16):163002, October 2007.

[108] Otfried Gühne and Géza Tóth. Entanglement detection. *Physics Reports*, 474(1-6):1–75, April 2009.

[109] D. Leibfried, E. Knill, S. Seidelin, J. Britton, R. B. Blakestad, J. Chiaverini, D. B. Hume, W. M. Itano, J. D. Jost, C. Langer, R. Ozeri, R. Reichle, and D. J. Wineland. Creation of a six-atom "Schrödinger cat" state. *Nature*, 438(7068):639–642, December 2005.

[110] Thomas Monz, Philipp Schindler, Julio T. Barreiro, Michael Chwalla, Daniel Nigg, William A. Coish, Maximilian Harlander, Wolfgang Hänsel, Markus Hennrich, and Rainer Blatt. 14-qubit entanglement: Creation and coherence. *Physical Review Letters*, 106(13):130506, March 2011.

[111] W. Dür and H.-J. Briegel. Stability of macroscopic entanglement under decoherence. *Physical Review Letters*, 92(18):180403, May 2004.

[112] Hoi-Kwan Lau and Daniel F. V. James. Proposal for a scalable universal bosonic simulator using individually trapped ions. *Physical Review A*, 85(6):062329, June 2012.

[113] David Gross, Yi-Kai Liu, Steven T. Flammia, Stephen Becker, and Jens Eisert. Quantum state tomography via compressed sensing. *Physical Review Letters*, 105(15):150401, October 2010.

[114] Steven T. Flammia and Yi-Kai Liu. Direct fidelity estimation from few pauli measurements. *Physical Review Letters*, 106(23):230501, June 2011.

[115] Wei-Tao Liu, Ting Zhang, Ji-Ying Liu, Ping-Xing Chen, and Jian-Min Yuan. Experimental quantum state tomography via compressed sampling. *Physical Review Letters*, 108(17):170403, April 2012.

[116] A. Shabani, R. L. Kosut, M. Mohseni, H. Rabitz, M. A. Broome, M. P. Almeida, A. Fedrizzi, and A. G. White. Efficient measurement of quantum dynamics via compressive sensing. *Physical Review Letters*, 106(10):100401, March 2011.

[117] Shihao Ji, Ya Xue, and L. Carin. Bayesian compressive sensing. *IEEE Transactions on Signal Processing*, 56(6):2346–2356, 2008.

[118] D. S. Gonçalves, C. Lavor, M. A. Gomes-Ruggiero, A. T. Cesário, R. O. Vianna, and T. O. Maciel. Quantum state tomography with incomplete data: Maximum entropy and variational quantum tomography. *arXiv:1306.0467*, June 2013. Phys. Rev. A 87, 052140 (2013).

[119] T. Baumgratz, D. Gross, M. Cramer, and M. B. Plenio. Scalable reconstruction of density matrices. *Physical Review Letters*, 111(2):020401, July 2013.

[120] Robin Blume-Kohout. Hedged maximum likelihood quantum state estimation. *Physical Review Letters*, 105(20):200504, November 2010.

[121] Robin Blume-Kohout. Optimal, reliable estimation of quantum states. *New Journal of Physics*, 12(4):043034, April 2010.

[122] S. J. van Enk and Robin Blume-Kohout. When quantum tomography goes wrong: drift of quantum sources and other errors. *New Journal of Physics*, 15(2):025024, February 2013.

[123] R. Blatt and C. F. Roos. Quantum simulations with trapped ions. *Nature Physics*, 8(4):277–284, April 2012.

[124] D. Leibfried, R. Blatt, C. Monroe, and D. Wineland. Quantum dynamics of single trapped ions. *Reviews of Modern Physics*, 75(1):281–324, March 2003.

[125] Milton Abramowitz and Irene A. Stegun. *Handbook of Mathematical Functions*. Dover Books on Mathematics. Dover Publications, 1965.

[126] Stephan Gulde, Mark Riebe, Gavin P. T. Lancaster, Christoph Becher, Jürgen Eschner, Hartmut Häffner, Ferdinand Schmidt-Kaler, Isaac L. Chuang, and Rainer Blatt. Implementation of the Deutsch-Jozsa algorithm on an ion-trap quantum computer. *Nature*, 421(6918):48–50, January 2003.